Lawrence Berkeley National Laboratory

Title
Research advances towards large-scale solar hydrogen production from water

Authors
Liu, Guanyu
Sheng, Yuan
Ager, Joel W
et al.

Research Advances towards Large-Scale Solar Hydrogen Production from Water

*Guanyu Liu,[†ab] Yuan Sheng,[†ab] Joel W. Ager,[cd] Markus Kraft,[abe] Rong Xu[*ab]*

[a]School of Chemical & Biomedical Engineering, Nanyang Technological University, 62 Nanyang Drive, Singapore

[b]Cambridge Centre for Advanced Research and Education in Singapore (CARES), CREATE Tower, 1 Create Way, Singapore

[c]Department of Materials Science and Engineering, University of California, Berkeley, California 94720, United States

[d]Berkeley Educational Alliance for Research in Singapore (BEARS), CREATE Tower, 1 Create Way, Singapore

[e]Department of Chemical Engineering and Biotechnology, University of Cambridge, West Cambridge Site, Philippa Fawcett Drive, Cambridge CB3 0AS, United Kingdom

†These authors contributed equally

*To whom correspondence should be addressed: RX (email: RXu@ntu.edu.sg)

Abstract

Solar hydrogen production from water is a sustainable alternative to traditional hydrogen production route using fossil fuels. However, there is still no existing large-scale solar hydrogen production system to compete with its counterpart. In this Review, recent developments of four potentially cost-effective pathways towards large-scale solar hydrogen production, *viz.* photocatalytic, photobiological, solar thermal and photoelectrochemical routes, are discussed, respectively. The limiting factors including efficiency, scalability and durability for scale-up are assessed along with the field performance of the selected systems. Some benchmark studies are highlighted, mostly addressing one or two of the limiting factors, as well as a few recent examples demonstrating upscaled solar hydrogen production systems and emerging trends towards large-scale hydrogen production. A techno-economic analysis provides a critical comparison of the levelized cost of hydrogen output via each of the four solar-to-hydrogen conversion pathways.

Table of Contents
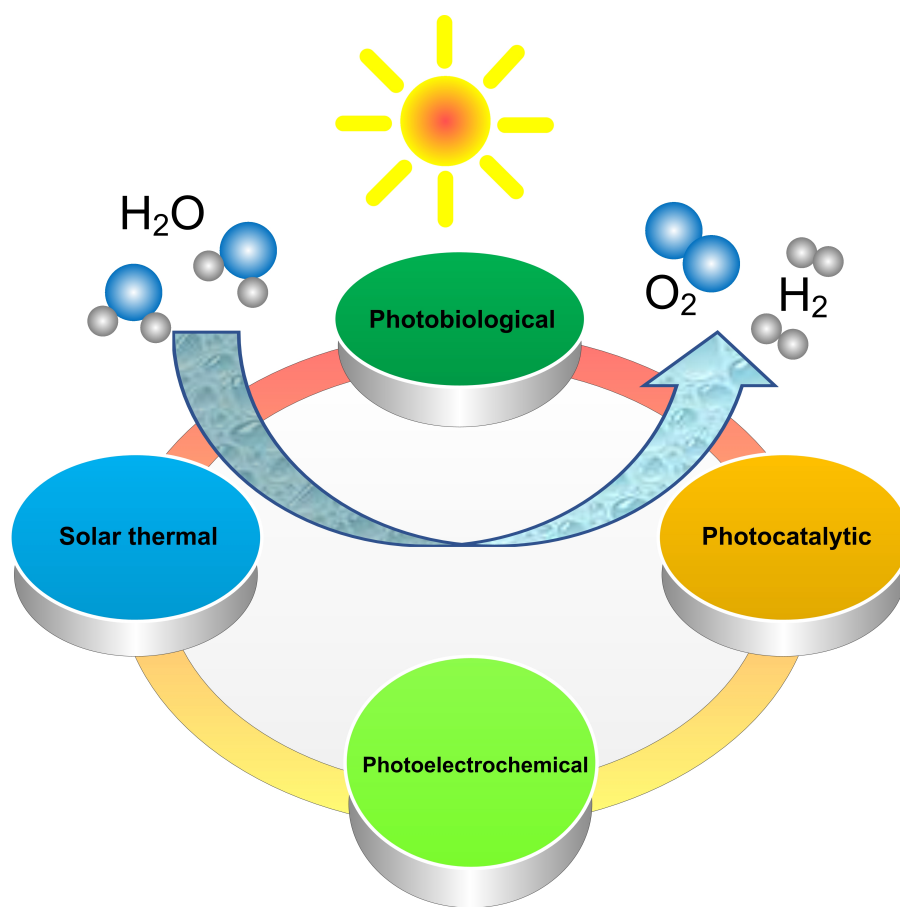
1. Introduction

Hydrogen is industrially utilized for methanol production, hydrocracking in petroleum refinery and ammonia synthesis for fertilizer production.[1] New markets are also emerging for vehicles powered by hydrogen fuel cells that combine hydrogen and oxygen from the air in an electrochemical reaction to generate electricity, as well as fuel cell home heating systems.[2-3] Furthermore, to alleviate environmental problems caused by fossil fuels during traditional hydrogen production routes such as methane reforming and coal gasification, solar hydrogen production from water has attracted intensive research interest as a promising pathway to a sustainable energy future of the planet.[4] Through this process, solar energy and earth-abundant water are converted into a storable fuel that is suitable for seasonal storage.[5] Over the last few decades significant progress has been made to improve the solar-to-fuel efficiency and stability of the solar-driven water splitting systems. However, this method still cannot compete with its counterparts that have been employed for large-scale hydrogen production of 50 million tonnes per year worldwide from fossil fuels.[6]

Water splitting into hydrogen and oxygen is a thermodynamically uphill reaction with free energy change ΔG^o of +237 kJ per mol of H_2 under standard conditions (25 ^{o}C, 1 atm pressure). This must be supplied, in this case, by the energy from sunlight to drive the water splitting reaction. Based on the forms of intermediate energy, the solar hydrogen production can be categorized into different production routes. Notably, a solar hydrogen production plant will be energy-positive only if the hydrogen-generating facilities meet certain efficiency and durability criteria.[7-8] Ongoing research is focusing on improving performance, increasing lifetime and reducing cost towards eventual large-scale implementation.[9-12]

In this review, we examine four approaches to achieve solar-driven hydrogen production, *viz.* photocatalytic, photobiological, solar thermal and photoelectrochemical hydrogen production, emphasizing upscaled systems and emerging trends towards large-scale hydrogen

production. Regarding each of the four solar hydrogen production routes, we discuss its reaction mechanism, materials development, system configuration, benchmark laboratory demonstration and field performance. In the last section, recent techno-economic studies are summarized to evaluate the levelized cost of hydrogen output via each production route, which can guide research investments to achieve commercially viable solutions.

2. Photocatalytic water splitting

First reported in 1977 with TiO_2 powders,[13] the simplest configuration of photocatalytic water splitting consists of a single type of semiconductor particles in contact with water (Figure 1a). Upon excitation by an incident photon with a higher energy than the bandgap of the semiconductor (E_g), an electron in the valence band (VB) can be promoted to the conduction band (CB) and leave behind a hole. The electron and hole have to separate spatially and diffuse to the surface of the semiconductor to participate in the hydrogen evolution reaction (HER) and oxygen evolution reaction (OER), respectively. For the simultaneous hydrogen and oxygen evolution, known as overall water splitting (OWS), to occur in this single semiconductor configuration, stringent requirements on the electronic structure of the semiconductor has to be met. At the thermodynamic limit, the OWS is reversible, the conduction band minimum (CBM) should match the redox potential of the H^+/H_2 pair and the valence band maximum (VBM) should match that of the O_2/H_2O pair, setting the theoretical minimum of E_g for OWS in the single semiconductor configuration at 1.23 eV. The theoretical limit for STH in the single semiconductor configuration has been calculated to be 31%,[14] and considering inevitable losses associated with state-of-the-art materials, a practical limit for such system has been estimated to be 11%.[15]
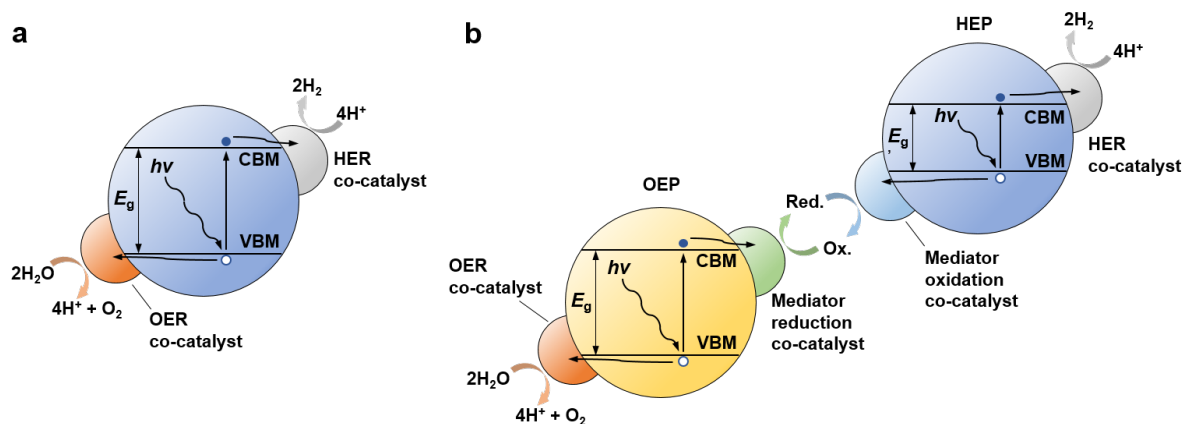
Figure 1. Simplified mechanism of photocatalytic water splitting in (a) the single-semiconductor and (b) the Z-scheme configurations. "Red." and "Ox." denote the reduced and oxidized forms of the redox mediator, respectively.

In practice, however, STH rarely exceeds 1% in photocatalytic OWS especially in the absence of UV radiation. One of the most important reasons is that only semiconductors with significantly larger E_g than 1.23 eV have exhibited OWS activity, some of the well-known examples being TiO_2, $SrTiO_3$, $NaTaO_3$, $Ga_{1-x}Zn_xN_{1-x}O_x$, and $g-C_3N_4$.[16-20] The large E_g of these materials prevents the utilization of all near-infrared and most visible light in solar radiation. Difficulties in exploiting narrow-bandgap semiconductors arise in three main aspects. First, extra energy in the photo-generated electrons/holes is required to overcome the activation barrier of OER/HER before water splitting occurs experimentally. The magnitude of the extra energy is determined by surface chemistry of the photocatalyst.[21] It adds to the required VBM/CBM and hence minimum E_g. Second, it is difficult to predict, measure, and tune the VBM and CBM separately. Often the VBM of a semiconductor is positive enough to drive the OER but the CBM is not negative enough to drive the HER, vice versa. As a result, most photocatalysts can only produce H_2 or O_2 at the expense of sacrificial electron donating or accepting chemicals, respectively. Third, many narrow-bandgap semiconductors are unstable in photocatalytic OWS conditions due to photochemical corrosion. The issue is typically more significant in materials consisting of anions other than O^{2-}, e.g. S^{2-}, Se^{2-}, and

N^{3-}.[22-24] These anions are oxidized at potentials more negative than that of the OER, making it thermodynamically more favorable for the photo-generated holes to oxidize the photocatalyst than to oxidize water.

Another prominent factor in the low STH is recombination of photo-generated electrons and holes. Instead of reacting with water, the electrons and holes can recombine to emit light (by radiative recombination) or heat (by non-radiative recombination), dissipating the energy they carry. The carrier diffusion length, which measures the average length a charge carrier travels in a semiconductor before recombination, offers an intuitive comparison of the extent of recombination. It ranges from over one millimeter for lightly doped silicon wafers[25] to just a few nanometers for TiO_2, the common photocatalyst.[26] The short carrier diffusion length limits the photocatalytic efficiency, as electrons/holes generated deeper in the photocatalyst particle do not contribute to the surface reactions. An indication of the effect of charge carrier recombination is internal quantum efficiency (IQE), defined as:

$$IQE = \frac{\text{number of electrons or holes reacted with water}}{\text{number of photons absorbed}} \times 100\% \qquad (1)$$

Larger deviation of IQE from 100% signifies heavier impact of recombination.

Before the hydrogen and oxygen produced on the photocatalyst can be recovered, a final obstacle has to be overcome, which is the reverse reaction of OWS. Just as water can accept and donate electrons in HER/OER, the produced hydrogen can react with photo-generated holes (in the hydrogen oxidation reaction, HOR) and the oxygen with photo-generated electrons (in the oxygen reduction reaction, ORR). These reverse reactions are exothermic and occur at room temperature, dissipating the chemical energy stored by OWS as heat and lowering the STH. While the impact of reverse reactions is difficult to quantify, it is encompassed, together with the effect of incomplete light absorption, by the commonly reported apparent quantum efficiency (AQE) which is more easily measured than IQE. AQE is defined as:

$$\text{AQE} = \frac{nr}{I} \times 100\% \tag{2}$$

where n is the number of electrons transferred for the evolution of unit amount of product, r is the rate of hydrogen/oxygen evolution, I is the rate of incident photons. In single semiconductor OWS, $n = 2$ for HER and $n = 4$ for OER. A detailed review on the theoretical aspect of the various physical processes affecting AQE is found elsewhere.[27]

Since the discovery of photocatalytic water splitting activity, enormous efforts have been made to improve the solar-to-hydrogen (STH) efficiency. The majority of the work has been focused on the design of the photocatalyst. To circumvent the strict requirement on the alignment between VBM/CBM and OER/HER potentials and hence allow for a wider choice of semiconductor materials, a double semiconductor water splitting system was proposed which was inspired by biological photosynthesis also known as the Z scheme.[28] Its first demonstration was reported much later in 2001 and today STH exceeding 1% has been achived.[29-30] In Z-scheme OWS as illustrated in Figure 1b, the photo-generated holes in the oxygen evolution photocatalyst (OEP) drive the OER while the electrons generated in the hydrogen evolution photocatalyst (HEP) drive the HER. Charge transfer between the two photocatalysts is achieved by either direct contact, a metallic mediator, or a redox couple in the electrolyte. This only requires the VBM of OEP to be more positive than the OER potential, CBM of HEP more negative than the HER potential, and CBM of OEP more negative than VBM of HEP. Therefore in theory, IR radiation less energetic than 1.23 eV can be utilized. However, it should be noted that in Z-scheme OWS the number of required photoexcitation and charge transfer events is double that of the single semiconductor OWS for the evolution of the same amount of hydrogen/oxygen. It follows that for the calculation of AQE (Equation 2), $n = 4$ for HER and $n = 8$ for OER. In addition, the kinetic barriers and reverse reactions associated with the charge transfer processes between the OEP and HEP

complicate the OWS system. As a result, Z-scheme OWS has not shown significant advantages over single semiconductor systems in terms of STH.[31]

Due to low capital and operating costs, photocatalytic water splitting has been frequently suggested as a promising method of solar hydrogen production.[32] The viability of photocatalytic OWS as a commercial technology, however, faces several great challenges at the current stage. The most important issues are its low STH, fire hazards of oxyhydrogen mixture, and limited/unknown stability of catalysts which still pose significantly higher cost compared with that of methane steam reforming catalysts.[33] In the following subsections, we discuss the research progress in improving the practicality of photocatalytic hydrogen production by dividing the literature in two broad categories focused on the catalyst and reactor/system design, respectively. The last subsection will present notable demonstrations of the technology beyond the laboratory scale.

2.1. Photocatalysts

So far the dominant focus of studies on water splitting photocatalysts has been their activity. The strategies for optimization of photocatalytic activity are briefly summarized herein, as up-to-date reviews under this topic can be readily found.[34-39] Potential methods for large-scale production of photocatalysts which form the focus of this section are discussed afterward in detail.

2.1.1. Strategies for photocatalyst design

First of all, bandgap engineering has been frequently involved to maximize the utilization of visible radiation. The two most successful strategies to achieve such bandgap tuning are probably doping wide-bandgap semiconductors with heteroatoms and preparing solid solutions of different semiconductors.[40] They have led to some OWS photocatalysts responsive to visible light with the longest wavelengths.[41-42] The first demonstration of visible light-driven OWS also employed the GaN-ZnO solid solution.[43] In doping

photocatalysts, donor states are introduced near the VBM and acceptor states near the CBM while in the electronics industry the opposite is usually true. This is because the main purpose of doping photocatalysts is narrowing the bandgap instead of generating thermally excited charge carriers which would greatly promote recombination. Nevertheless, the introduction of heteroatoms does promote recombination by disrupting the regularity of the host lattice. The degree of doping has to be carefully controlled such that the benefit of increased visible light absorption is not overwhelmed by the enhanced recombination.

After photons have been captured to generate electron-hole pairs, the competition between charge carrier separation and recombination becomes important, which has received considerable attention. Charge carrier separation is improved by an electric field. In photocatalytic systems where no external circuit is connected, the electric field can be generated by anisotropy of the photocatalyst's crystal structure or formation of semiconductor-semiconductor junctions.[44] Positive effects of junctions both between semiconductors of different chemical compositions and between different crystallographic phases with the same chemical composition have been demonstrated.[45-46] On the other hand, recombination caused by presence of defects including lattice dislocation, interstitial filling, vacancies, and surface states can be suppressed by increasing the crystallinity of the photocatalyst and excluding contaminants.[47] Appropriate annealing, for example, is desirable in this regard.[48] Alternatively, the photocatalyst can be prepared in the form of nanoparticles to shorten the diffusion pathways of the charge carriers and hence their probability of recombination, as has been commonly carried out.[36] However, excessively small particles have poor optical absorption and are rich in surface defects that promote recombination.

Another main body of work on water splitting photocatalysts has been focused on the surface chemistry. Compared with the generation and diffusion of charge carriers, the surface reactions (HER/OER) occur over a longer timescale and are the rate determining steps in

most water splitting systems.[44, 49] The surface of semiconductors optimized for light absorption usually has high HER/OER overpotential. To facilitate the surface reactions, co-catalysts with lower overpotentials have been used since the earliest studies on photocatalytic OWS.[50] Anchored to the surface of the light-harvesting semiconductor, they are the actual reaction centers for HER/OER. For many photocatalysts including the most studied TiO_2, co-catalysts are in fact necessary for any measurable OWS activity.

As water electrolysis closely parallels photocatalytic OWS, electrocatalysts for the former can serve as co-catalysts for the latter. In practice, a single co-catalyst for HER/OER or two co-catalysts for both half reactions can be introduced to a photocatalyst as illustrated in Figure 1. For example, Pt and other platinum-group metals are well known for their low HER overpotential and most frequently adopted as the HER co-catalyst.[47] In recent years novel materials based on earth-abundant elements including first-row transition metal phosphides[51], chalcogenides[52], and biomimetic molecular catalysts[53] for this purpose have gained increasing attention. For OER, oxides of Mn, Co, Ni, Ru, and Ir are commonly used as the co-catalyst.[47] The synergistic effect of applying both HER and OER co-catalysts to the same photocatalytic system has been demonstrated, affording up to twofold increase in AQE compared with using one co-catalyst.[54-55] With appropriate alignment between the band energy of the light absorber and the co-catalyst, the latter acts as an electron trap to suppress recombination and increase quantum efficiency.[56] Furthermore, co-catalysts exhibiting surface plasmonic resonance (SPR) can facilitate the generation of electron/hole pairs regardless of E_g of the photocatalyst.[57] If the SPR occurs at a lower energy than E_g, then the range of operable wavelength for the photocatalyst can be extended by incorporating the co-catalyst. Visible light-responsive Au- and Ag-based systems are notable examples.[58]

On the other hand, most noble metal co-catalysts e.g. Pt also catalyze the reverse reactions of water splitting and reduce the amount of recoverable hydrogen/oxygen. To inhibit the

reverse reactions, deposition of an amorphous metal oxyhydroxide nanolayer on the co-catalyst has been found effective.[59-60] It was proposed that the nanolayer impedes ORR by selectively blocking diffusion of oxygen towards the co-catalyst surface. Finally, excessive loading of co-catalysts can prevent effective absorption of incident light by the photocatalyst. For a balance between the positive and negative effects as well as economic considerations, the typical loading of co-catalysts is below a few percent by weight.

Since the 2000s energy crisis which stimulated interest in the commercial potential of solar water splitting, there has been increasing research on replacing the noble metal components of photocatalysts with less expensive materials. Figure 2 shows that many elements commonly used in photocatalysts/co-catalysts such as Cd, Se, Pt, Bi, Ru and Ir are not only costly but also scarce in nature. Extensive consumption of these elements in a future energy industry built on solar H_2 production would be unsustainable if not impossible. In this context many earth-abundant metals/metal oxides have been found to be efficient co-catalysts with activity comparable to noble metals,[61-62] and completely metal-free photocatalysts have emerged as another promising system.[63] Notably, a C_3N_4 catalyst loaded with carbon nanodots has shown a STH of 2% and stable performance over 200 days in OWS.[64] Despite these successes, relatively little attention has been paid to scaled-up photocatalyst synthesis. It is well recognized that the preparation of nanomaterials, which accounts for the majority of studies on photocatalytic water splitting, is a kinetically controlled process and highly sensitive to the history of the physicochemical environment.[65] Accurate size and morphological control over the product in large scales is challenging due to temperature and concentration inhomogeneity. As production of catalysts with reliable quality in industrially relevant throughputs is essential to the viability of the technology, research efforts to this end are discussed herein.
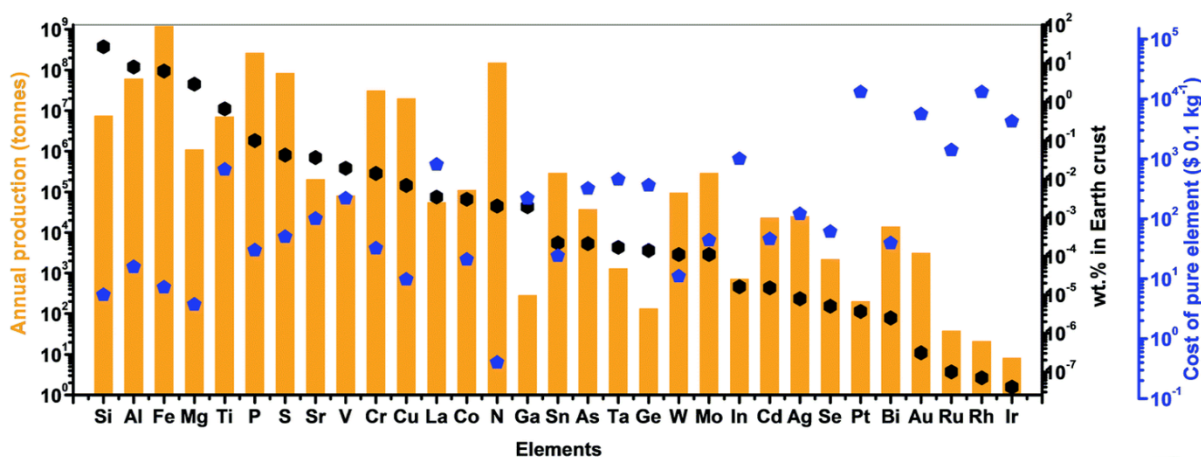
Figure 2. Annual production, abundance, and cost of common elements. Adopted with permission from Ref. [9], copyright (2019) the Royal Society of Chemistry.

2.1.2. Large-scale batch synthesis of photocatalysts

To date batch-wise wet chemical processing has remained the dominant method of laboratory catalyst synthesis. It requires minimal investment in equipment and is supported by extensive knowledge in open literature. However, to achieve accurate control over size and morphology of nanocatalysts which is crucial to their catalytic performance, highly diluted reaction mixtures are most frequently involved. As separation of the nanocatalysts usually requires energy-intensive centrifugation instead of filtration methods, such processes have significantly higher operating cost than those for conventional particulate products, and the energy penalty is further aggravated by the large volume of reaction mixtures. Given the low productivity of the diluted reaction system and narrow margin of profit in water splitting, the same strategy for size/morphology control in laboratory is likely to be prohibitive in an industrial setting. In one example, hydrothermal synthesis of $Cd_{0.5}Zn_{0.5}S$ nanocrystals with a production rate of ~0.8 kg per batch has been performed in a 13 L stirred tank reactor.[66] The self-contained apparatus also consisted of reagent storage, product separation, and waste gas treatment units as shown in Figure 3. Remarkably, the nanocrystals were separated by ultrafiltration which demands less energy input than centrifugation at the expense of automation. The catalyst exhibited an energy conversion efficiency of up to 4.3% and an

13

AQE of 40.5% at 425 nm, which almost equals the activity of a similar catalyst synthesized in a 130-fold smaller batch. However, the particle size distribution and catalytic activity are noticeably worse than in a 2-fold diluted, laboratory-scale synthesis requiring no stirring[67], highlighting the difficulty in process intensification of nanomaterials synthesis in batch-wise wet chemical systems.
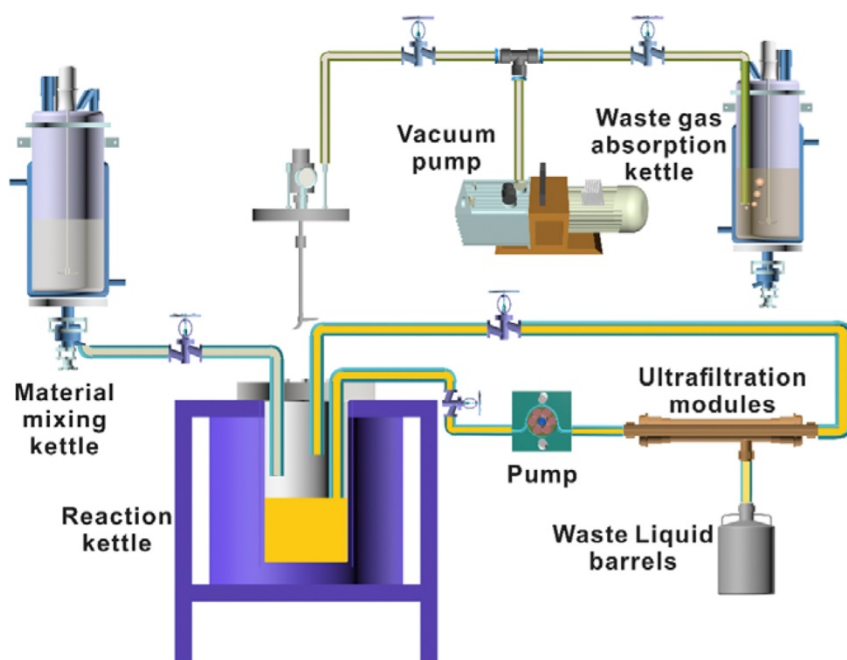

Figure 3. Schematic diagram of a pilot plant for hydrothermal synthesis of $Cd_{0.5}Zn_{0.5}S$ nanoparticles in batch mode. Reproduced with permission from Ref. [66], copyright (2018) Elsevier Ltd.

Besides increasing batch size, it is also possible to improve the throughput of batch-wise synthesis by shortening the processing time. Completion of reactions has to be still ensured for reasonable yield, which can be achieved by more efficient heating methods such as microwave heating. A type of dielectric heating in nature, it does not depend on any thermally conductive medium, and heat is generated evenly in the reaction mixture as long as it is homogeneous within the reach of the radiation, reducing the effects of convection. So far microwave heating has primarily been used to accelerate wet chemical synthesis.[68] For example, 200 nm α-Fe_2O_3 particles have been prepared in a 5 L microwave-heated

14

hydrothermal reactor with a production rate claimed to be comparable to 2.1 m^3 conventional reactors.[69] Many nanomaterials with photocatalytic water splitting activity have been prepared by similar methods where the required reaction time, typically a few to a few tens of minutes, was an order of magnitude lower than in conventional hydrothermal methods.[70] However microwave-assisted synthesis of photocatalysts has not exceeded the gram scale in laboratory research. The main reason is probably the limited penetration of 2.45 GHz microwave generated by most commercial equipment.[71] To heat the internal volume of large reactors, heat transfer from the outer layer accessible to microwave is the only channel, which offsets the benefits of microwave heating to some degree. Deeper penetration of microwave energy can be achieved by nonstandard lower frequency equipment, but the cost is much higher.

Laser and direct current have also been used to deliver heat efficiently to reactants. In the former case, the optical energy is converted to localized heat at the point of contact, melting/vaporizing the starting material which is then cooled by and react with the reaction medium.[72] Considering that examples of laser-assisted synthesis of water splitting photocatalysts are rare, it is remarkable that CoO nanoparticles synthesized by femtosecond pulsed laser ablation of CoO microparticles in water have exhibited the highest recorded unassisted photocatalytic OWS activity at a STH of 5%.[73] Similar to laser, a high voltage applied to the solid-liquid interface can also generate localized heat through plasma discharge, which has been exploited for one-step synthesis of TiO_{2-x} with visible light sensitivity.[74-75] Briefly, high voltage pulses were applied to Ti electrodes immersed in an NH_4NO_3 or HNO_3 electrolyte. It was proposed that metallic Ti melted/vaporized by the plasma at the cathode was quickly quenched by the relatively cold electrolyte while being oxidized, resulting in the partially oxidized product. In the two aforementioned synthesis methods, the amount of materials converted by each laser/electrical pulse is microscopic, but the reaction is usually

completed within the millisecond scale due to extreme temperatures. As most of the input energy is delivered to the solid-liquid interface instead of the bulk of the mixture, they are also energy-efficient and hence have potential for scale-up, provided that economic processes for product recovery are developed.

Compared to wet chemistry, solid-state synthesis allows for much higher precursor concentrations and hence more efficient use of reactor volume. Pyrolytic synthesis of g-C$_3$N$_4$, for instance, has been scaled up from 5 g to 500 g of urea as precursor, producing up to ~28 g of g-C$_3$N$_4$ per batch.[76] Constant yield was obtained and 90% of H$_2$ evolution activity was maintained after the scale-up. While strictly speaking the pyrolysis of urea occurs in the liquid (molten) phase, some of the most efficient photocatalysts such as doped SrTiO$_3$, NaTaO$_3$, and GaN-ZnO solid solutions have indeed been produced by conventional solid-state reactions.[17-18, 48] Due to sluggish diffusion and interaction of solid precursors which necessitate high temperature for acceptable reaction rates, such syntheses are slow, energy-intensive, and accompanied by severe sintering. The as-synthesized products are typically micrometer-sized particles with low specific surface area limiting the amount of available catalytic sites. But on the other hand, the high temperature facilitates the removal of structural defects from the semiconductor crystals and improves the carrier diffusion length. The negative effects of small surface area may be compensated for by increased number of charge carriers reaching the catalytic sites, resulting in enhanced activity with particle size. Furthermore, the method is well-established in industrial production and the yield is close to 100% on a metal basis. Despite the fact that the throughput in research works has been limited to several grams, we believe that solid-state synthesis has great potential for production of photocatalysts in larger scales.

Similar to wet chemical methods, solid-state synthesis of photocatalysts has adopted microwave heating. However, the efficiency of heating is sensitive to electrical properties of

the material being processed, which is greatly buffered by the copious amount of solvent present in wet chemical systems but not in solid-state synthesis. Microwave heating is therefore non-uniform in solid-state mixtures due to their inhomogeneity. Nevertheless, microwave-assisted synthesis of g-C_3N_4 from urea, melamine, cyanamide, or thiourea has been reported with a maximum of 2 g of product produced per batch.[77] CuO was used as the heating medium to deliver heat to the reaction mixture as it strongly absorbs microwave radiation. Although this affects the uniformity of heating, the reaction time was reduced to 18 min from the 3-4 h required by conventional heating. The product even exhibited 50% improvement in photocatalytic hydrogen evolution compared with g-C_3N_4 synthesized in a furnace, with a higher crystallinity cited as the main factor.

In solid-state synthesis, the reaction can be accelerated by not only efficient heating but also addition of flux which melts during the synthesis, e.g., molten salt, and acts as a solvent to promote local diffusion of reactants. It is well-established industrial practice to add flux up to a few percent of the total feed. Recently, the method has been developed further by increasing the amount of flux so that a significant fraction if not all of the precursors are dissolved during synthesis.[78] The resulting process, namely molten salt synthesis, allows for controllable formation of nanocrystals as nucleation and growth of crystals are more uniform than in conventional solid-state synthesis. In this sense, it parallels wet chemical processing albeit with significantly higher reactant concentrations. Sr-doped $NaTaO_3$ nanocubes with sizes of 20-60 nm, for example, have been synthesized from Na_2CO_3, $SrCO_3$, and Ta_2O_5 in molten NaCl-KCl and exhibited remarkable OWS activity under UV radiation.[79]

2.1.3. Large-scale continuous synthesis of photocatalysts

Batch-wise synthesis requires evacuating and recharging of reactors which inevitably leads to long downtime and batch-to-batch variations due to highly non-linear heat/mass transport involved, particularly in wet chemical processes. As a result, continuous processes are

17

preferred in industrial production. There has been considerable research on continuous hydrothermal flow synthesis (CHFS) of inorganic nanomaterials since the 1990s, a comprehensive review of which has been published recently.[80] In contrast to laboratory-scale batch synthesis where the reaction mixture is usually heated for several hours at up to 200 °C, the studies aimed at industrial production adopt reaction temperatures of 200-400 °C to reduce the required residence time to a few seconds or minutes. In order to achieve the high temperature in an even smaller timescale before the product starts to form, the precursor solution is often heated by directly mixing it with supercritical water. Using this method, production of <100 nm metal oxide, hydroxide, sulfide, and phosphate nanoparticles in the kg/h scale has been readily realized. Figure 4 shows a representative schematic diagram of a CHFS system.
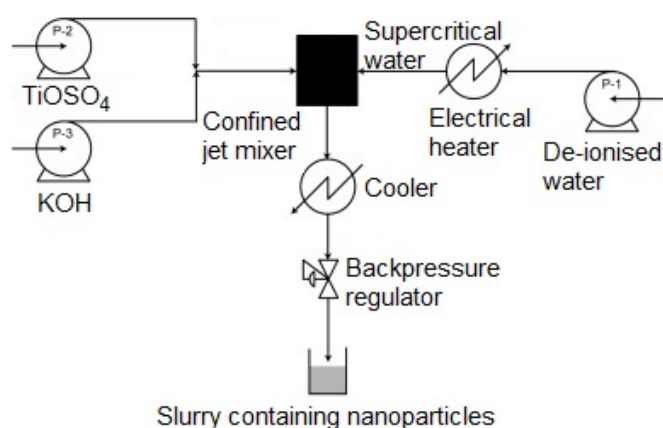

Figure 4. Schematic diagram of a typical continuous hydrothermal flow synthesis (CHFS) set-up. Adopted and modified with permission from Ref. [81], copyright (2015) Elsevier Ltd.

While many photocatalytically active materials including TiO_2, ZnO, CdS, α-Fe_2O_3, WO_3, *etc*. have been synthesized using this method, reports on their photocatalytic water splitting activity are scarce. Starting from $TiOSO_4$ and KOH, Makwana *et al.*[81] synthesized anatase TiO_2 nanoparticles with tunable sizes of 5-18 nm and tested their water splitting activity after sputter coating pelletized TiO_2 particles with Pt. The Ti precursor were processed at 6 mol/h with a residence time of ~5.5 s in the hot section of the reactor.[82] More recently, 5 nm Ti^{3+}-

doped TiO_2/C composite was synthesized in a smaller scale where the throughput of Ti precursor was 45 mmol/h.[83] It showed a hydrogen evolution activity 49 fold higher than that of commercial P25 TiO_2 evaluated in the same conditions. Similar activity was achieved with $K_2Ti_6O_{13}$ nanofibers in an earlier work.[84] The material was synthesized with a residence time of ~2 s and a production rate of 0.3 g/h. Admittedly the throughput of CHFS still faces the bottleneck of the dependence on time-consuming centrifugation processes for product separation, as is the case in most laboratory studies on nanomaterials.

Although not well known in the field of chemistry, gas-phase synthesis is by far the most established method for commercial production of nanomaterials. Today the majority of nanoparticle commodities including carbon black, fumed silica, and the benchmark photocatalyst P25 TiO_2 are produced by a type of gas-phase process, namely flame aerosol synthesis (FAS), first commercialized in the 1940s.[85] In FAS, the precursors and supporting fuel in the form of either vapors or atomized liquid are introduced continuously into a flame. The precursors are pyrolyzed in the flame to form nanoparticles entrained by the exhaust which can be recovered by cyclone separators or filters.

Due to the few unit operations and energy-efficient separation techniques involved, FAS is suitable for large scale production. The number of nanomaterials successfully synthesized by FAS is enormous, covering the oxides of almost all the metal elements in the periodic table up to the 6th period and all the noble metal particles.[86] However, while common metal oxide photocatalysts have mostly been prepared by FAS, their activity in water splitting has been seldom reported.[87] To the best of our knowledge, TiO_2 has remained the only FAS-derived material tested for water splitting activity. A majority of such works have been reviewed.[88]

As an example, a series of F-doped 1% Pt/TiO_2 was synthesized in one step by liquid-fed FAS, and exhibited high hydrogen evolution activity from mixed methanol and water vapors.[89] The schematic diagram of typical liquid-fed FAS equipment is shown in Figure 5a,

where a solution of metal precursors in flammable solvent is atomized by and burnt in oxygen. Due to the heat released by combustion of the fuel, the temperature of the precursor droplets quickly rises to >1000 °C, enabling its complete vaporization before pyrolysis products reach super-saturation. As a result, particle formation can mainly proceed by homogeneous nucleation and lead to nanometer sizes. In this case, XRD analysis showed that the TiO_2 consisted of ~90% anatase and ~10% rutile with average crystallite sizes of 15-20 nm.
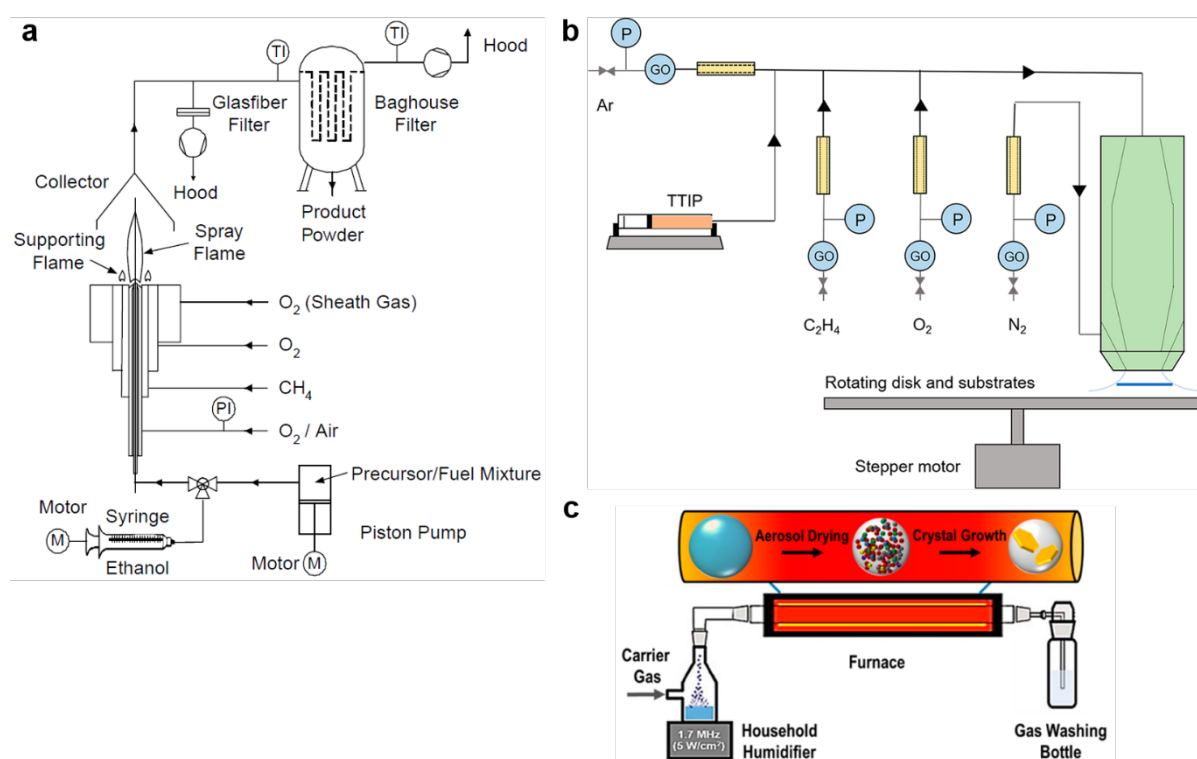

Figure 5. Schematic diagrams of (a) liquid-fed flame aerosol synthesis, reproduced with permission from Ref. [90], copyright (2003) Elsevier Science Ltd. (b) vapor-fed flame aerosol synthesis, reproduced with permission from Ref. [91], copyright (2018) American Chemical Society, and (c) ultrasonic spray pyrolysis, reproduced with permission from Ref. [92], copyright (2016) American Chemical Society.

Recently, our group demonstrated a photocatalytic H_2 evolution AQE of 39.4% at 360 nm in methanol solution using a FAS-derived 10-20 nm TiO_2 photocatalyst with 0.1% of Pt co-catalyst.[91] Different from the study mentioned earlier, the TiO_2 was synthesized by feeding

vaporized titanium(IV) tetraisopropoxide together with ethylene, oxygen and argon to a flat flame stabilized on the surface of a rotating collection disk as shown in Figure 5b. Interestingly, the TiO_2 II phase that had only been synthesized at extreme pressures was obtained in open atmosphere in this work, possibly due to fast quenching of metastable intermediates before rutile crystallized.[93] The presence of TiO_2 II/anatase/rutile junctions may be beneficial to charge carrier separation and hence the photocatalytic activity.

Apparently, a flame is not the only possible heat source for gas-phase synthesis of nanomaterials. As depicted by Figure 5c, in the so-called ultrasonic spray pyrolysis process, conventional tube furnace is used to continuously dry and pyrolyze fine droplets of precursor solution without involving combustion. A number of titanates and tantalates active in photocatalytic water splitting have been synthesized using this method, the performance of which is summarized in Table 1. Compared with FAS, the ultrasonic spray pyrolysis does not afford heating of the precursors as fast. The vaporization of droplets is therefore incomplete before significant amount of product forms, and the resulting particles retain the shape of the precursor droplets in the form of polycrystalline aggregates. It has been noted, however, that despite the large potential of gas-phase nanomaterials synthesis for commercialization, the short residence time of particles prevents healing of their structural defects which compromises the photocatalytic activity.[94] Combination with a following annealing step or wet chemical treatment[95] may be necessary to achieve desirable results. In addition, adsorbed species on nanoparticles and their effect on morphological control during FAS have been poorly understood. Unlike in wet chemical synthesis where a large variety of surface capping agents can be applied to control particle growth on specific crystal facets, in FAS the harsh environment limits such control. As a result, FAS-derived nanocatalysts with sophisticated structural features, for example crystal facets of high Miller indices, have not been reported.

Table 1. Photocatalytic water splitting performance of catalysts synthesized by ultrasonic spray pyrolysis

Photocatalyst	Co-catalyst	AQE*	Ref.
$NaTaO_3$	NiO	50.9% @ 254 nm	[96]
$C/NaTaO_3$	-	~30% @ 254 nm	[97]
$g-C_3N_4 / SrTiO_3:Rh$	Pt	5.5% @ 410 nm	[98]
$SrTiO_3:Ni,Ta,La$	Pt	3.6% @ 420 nm	[99]
$SrTiO_3:Rh,Ta$	Pt	8.4% †	[100]
$Sr_{1-2x}Na_{2x}Ti_{1-x}Mo_xO_3$	Pt	1.8% †	[101]
$SrTiO_3:F$	Pt	0.74% †	[102]
$SrTiO_3:Mo$	Pt	2.3% †	[103]

*The activity was measured in aqueous methanol.

†The apparent quantum efficiency (AQE) was measured at an unstated wavelength.

2.2. Reactor/system Design

In the majority of studies on photocatalytic water splitting, the measurement of activity is carried out in a magnetically stirred tank reactor where the catalyst slurry receives irradiation through a quartz/glass window and the gaseous product is sampled by a manifold connected to the reactor. Typically the volume of slurry is below 1 L with less than 1 g of the photocatalyst, producing no more than several millimoles of hydrogen per hour. For industrial applications that require production on a large scale (cubic meters per hour), at least 1000-fold scale-up is necessary. As the low activity of photocatalysts has been generally considered the main obstacle to practical use of the technology, little attention has been paid to the engineering aspect of the problem which in our view, however, is as important and complex. Research on the design of photocatalytic water splitting reactors has been partially reviewed,[104-106] and the following discussion aims to complement these reviews while providing necessary background information.

2.2.1. Safety

For OWS reactors, one of the critical issues of scale-up is the fire/explosion hazard of oxyhydrogen mixtures because hydrogen and oxygen are generated simultaneously. It has been suggested that the hydrogen be diluted with an inert gas, for example nitrogen or carbon dioxide, until its concentration is below the lower flammability limit, and be separated by

selectively permeable membranes from the hydrogen-oxygen-inert gas mixture.[107-108] However, considering hydrogen's lower flammability limit of only 4% (in air/oxygen, normal temperature and pressure), the large amount of required diluent poses heavy burden to the process. Even though the flammability range of hydrogen is significantly narrowed by the suppressing effects of carbon dioxide, the optimal specific cost of 99% hydrogen has been estimated at 6.40 $/kg compared with 2 $/kg for the established methane steam reforming process.[108] In addition, no experimental demonstration of such systems has been reported.

On the other hand, selective membranes can render Z-scheme OWS intrinsically safe by separating the HEP and OEP in two compartments, so that hydrogen and oxygen are not mixed at any point.[109-110] Figure 6 illustrates that in such a system, an ion exchange membrane allows aqueous redox mediators (in this case Fe^{2+}/Fe^{3+}) to cross and complete the HEP-OEP charge transfer while blocking the diffusion of hydrogen/oxygen to a large extent. Although it was claimed that the reactions were not limited by mass transfer resistance across the membrane, the rate of gas evolution (0.48 μmol/h for H_2 and 0.25 μmol/h for O_2, with 0.3 g of HEP and OEP each, 500 W halogen lamp) is low.[110]
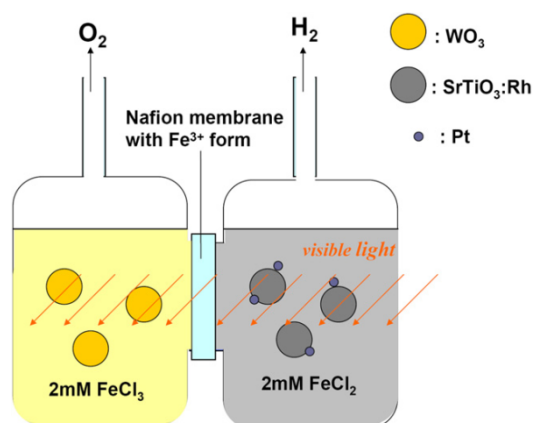

Figure 6. A twin reactor for Z-scheme water splitting with the HER and OER chambers separated by cation exchange membrane. Reproduced with permission from Ref. [110], copyright (2009) Elsevier Ltd.

In fact, similar function can also be realized by non-selective membranes. Using a membrane filter with 10 μm pore size as the separator, Sasaki *et al.* obtained hydrogen at 4.9 μmol/h from 0.1 g of Ru/SrTiO$_3$:Rh and oxygen at 1.9 μmol/h from 0.3 g of BiVO$_4$ simultaneously.[111] About 4% of the hydrogen inevitably crossed the membrane and contaminated the oxygen, but as a side product the hydrogen-contaminated oxygen could be diluted and purged by air to eliminate the hazard. Importantly, upscaling of the porous medium-separated Z-scheme OWS to full-size plants has been examined with the outlook of achieving practical success.[112-113] The proposed reactor is composed of low-cost polymer film "baggies" containing photocatalyst slurries as illustrated in Figure 7. The flexibility of the polymer film allows for expansion of the baggies as a temporary storage method for H$_2$ and O$_2$, thus simplifying the pneumatic system. Safety advantages of separate production of H$_2$ and O$_2$ (Figure 7b) over generation of H$_2$/O$_2$ mixture (Figure 7a) are apparent, given the volume of gases to be dealt with in such scales.
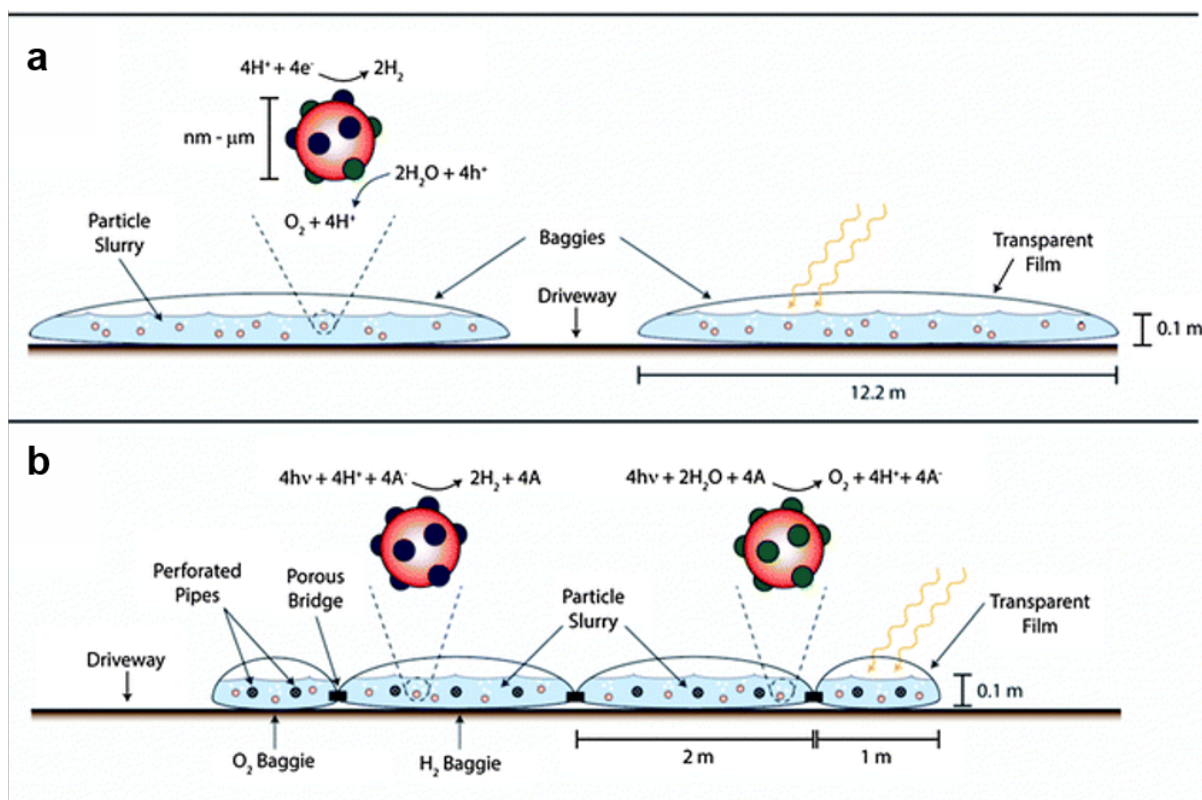
2.2.2. Hydrodynamic design and suppression of reverse reactions

During laboratory evaluation of photocatalyst powders, care is always taken to ensure even distribution of the catalyst in the slurry through vigorous magnetic stirring. The role of stirring in maximizing hydrogen production rate has been recognized and attributed to enhancement of light absorption and mass transfer.[114-115] In large-scale operation, however, mechanical stirring is uneconomical in photoreactors due to the large energy penalty associated. Although the amount of studies on water splitting photoreactors has been too small to provide an empirical guideline for the hydrodynamic design, major reactor designs in the closely related and more developed field of photocatalytic waste water treatment have exclusively been of the continuous flow type, among which tubular reactors coupled to solar concentrators have seen the most success in pilot- or larger scale applications.[116] This is largely a result of knowhow accumulated through extensive research on solar thermal engineering. Similar designs can in principle be applied to water splitting but it should be taken into consideration that water splitting requires more gas-tightness for hydrogen recovery and no routine separation of photocatalyst. Indeed, tubular reactors form the heart of most pilot-scale works on photocatalytic water splitting. Homogeneous distribution of catalyst particles in such reactors is achieved by recirculating the slurry in the tubes under fully turbulent conditions.

In the laboratory scale, flow regimes other than that of the tubular reactors have also been investigated for water splitting. For example, a shallow funnel-shaped photoreactor without active stirring was demonstrated to achieve similar STH as was an ordinary stirred tank photoreactor.[117] Figure 8a,b show the structure of the reactor where the slurry was introduced

tangentially to induce turbulence and hence mixing. Notably, in a more recent study 44%

improvement in AQE was demonstrated using Pt/TiO$_2$ catalyst beads in a fluidized bed

reactor compared with using recirculating suspension of Pt/TiO$_2$ nanoparticles.[118] The system

also included a sparger in the downstream of the reactor to extract the hydrogen and oxygen

with a N$_2$ carrier gas, as illustrated by Figure 8c. Through computational modelling, it was

proposed that efficient mass transfer and fast removal of the product gases were key factors

in the high AQE because they suppressed the reverse reactions.[119] However, fluidized bed

reactors require photocatalysts in the form of millimetre-sized beads which significantly

increases the mass of solids to be handled. The upright positioning of the reactor also poses
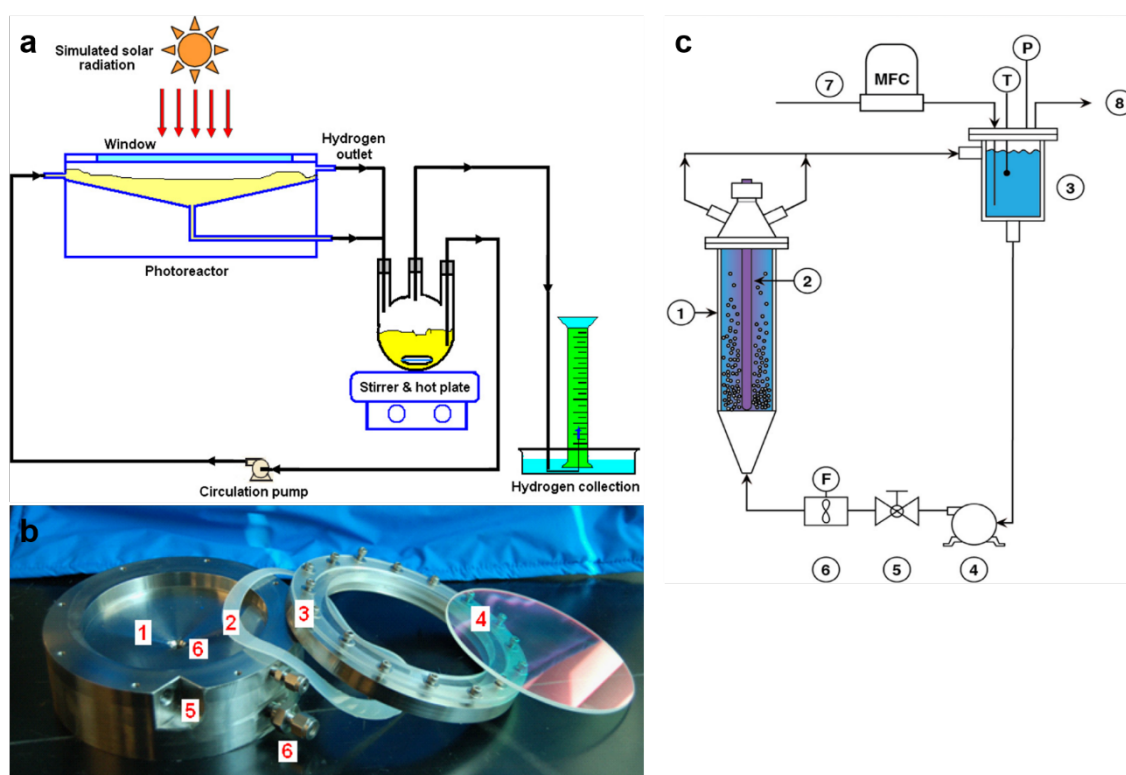
difficulty in sunlight collection.

Figure 8. (a) Schematic diagram and (b) photo of a laboratory-scale flow reactor system: 1, photoreactor; 2, gasket; 3, flange; 4, window; 5, inlet port; 6, outlet port. Reproduced with permission from Ref. [117], copyright (2010) Elsevier Ltd. (c) Schematic diagram of a fluidized bed reactor system for photocatalytic water splitting: 1, fluidized bed reactor; 2, UV lamp; 3, gas-liquid separator; 4, pump; 5, flow control valve; 6, flow meter; 7, mass flow controller

for N$_2$ sparging; 8, outlet to GC. Reproduced with permission from Ref. [118], copyright (2017) Elsevier Inc.

Also to control reverse reactions, an interesting method was reported where dissolved oxygen in a photocatalyst slurry was removed through an immersed oxygen-selective membrane by flowing argon as purge gas on the dry side of the membrane.[120] More than 100% improvement in hydrogen evolution rate was achieved thereby. In fact, measures to prevent reverse reactions have been routinely taken in laboratory studies, albeit without being realized and/or properly acknowledged sometimes. For example, most commercially available apparatus for photocatalytic water splitting experiments allow the system to be evacuated and operated under subatmospheric pressure. The low pressure leads to decreased solubility of hydrogen/oxygen which not only suppresses the reverse reactions but also enhances desorption of the products from the catalyst surface. Moreover, sacrificial electron/hole scavengers such as Ag^+, $S_2O_8^{2-}$, S^{2-}, methanol and triethanolamine have been frequently used to render the water splitting reaction irreversible.

From an engineering point of view, low pressure operation in large scales causes heavy energy penalty to the process, and unless the sacrificial reagent is a waste or regenerated using renewable energy, production of hydrogen as a basic feedstock at the expense of the downstream chemicals cannot be justified. In this connection, a hybrid photocatalytic-solar thermal cycle has been proposed.[121] In the model, photocatalytic hydrogen evolution occurs together with oxidation of aqueous $(NH_4)_2SO_3$ to $(NH_4)_2SO_4$ by photo-generated holes. The $(NH_4)_2SO_4$ then goes through a metal oxide-assisted multistep solar thermal process to regenerate $(NH_4)_2SO_3$ and produce oxygen. However, the energy required to vaporize all the remaining water after the photocatalytic step presents an issue for the overall efficiency of the hybrid cycle.

2.2.3. Optical design

Compared with ordinary reactors, the design of photoreactors is complicated by the need to maximize exposure of catalyst particles to incident solar radiation. In the simplest form, a photoreactor can be a flat panel-type container as shown in Figure 9a, which has been proven a cost-effective solution to water treatment.[116] The entire surface of the reactor can receive both direct and diffuse light, so the incident angle of sunlight does not affect photocatalytic performance as strongly as it does to tubular reactors with solar concentrators which will be discussed in more details. For water splitting, however, the reactor has to be sealed with a transparent cover and the capital cost increases. The issue is aggravated by the fact that few structural materials exhibit good transmission of UV radiation which is most efficiently utilized and for many wide-bandgap photocatalysts, the only usable part of solar radiation. Laboratory works usually adopt quartz glass as the cover which is too costly for large reactors. While thin borosilicate and soda lime glass can have satisfactory transparency to terrestrial UV, in large areas their thickness has to be increased to support their own weight and the UV transmission decreases. Some engineering polymers have been suggested as alternatives,[117] but their reliability under constant exposure to direct sunlight is questionable. For these reasons, tubular glass reactors have become the midway solution as a compromise between transparency and mechanical strength. Nevertheless, flat panel reactors were adopted by recent pilot-scale trials of photocatalytic water splitting as elaborated further in Section 2.3, which is most possibly due to the low cost and ease of reactor construction in such scales.[122-123]
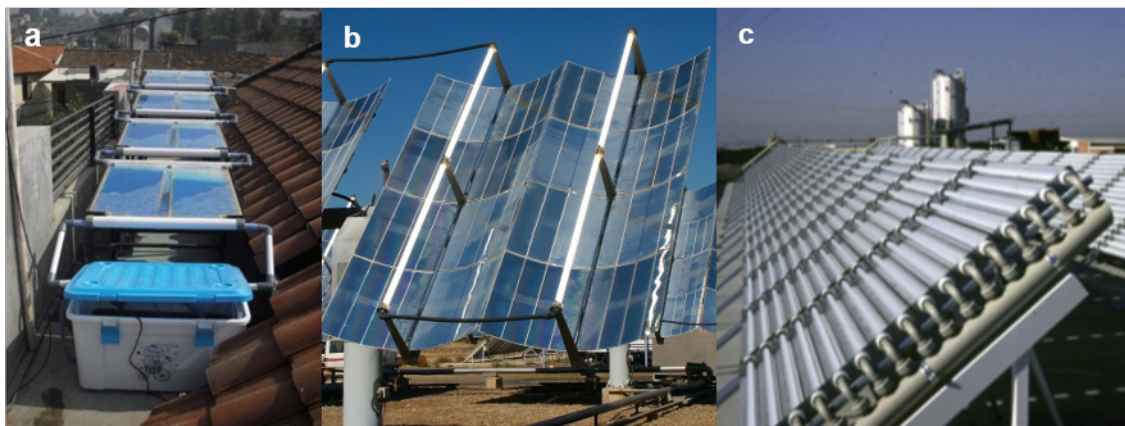
Figure 9. Photos of typical (a) flat panel photoreactor, adopted with permission from Ref. [124], copyright (2017) Elsevier Ltd. (b) tubular photoreactor with parabolic trough collector and (c) tubular photoreactor with compound parabolic collector, adopted with permission from Ref. [125], copyright (2015) Elsevier Ltd.

To fully utilize the surface area of the tubular reactors, light reflectors of various geometries have been designed to illuminate the underside of the reactors. Originated from solar thermal engineering, the oldest type of reflectors had a single parabolic profile. This configuration known as a parabolic trough collector (Figure 9b) can only reflect incident light that is perpendicular to its aperture to the reactor tube at the focus and wastes all the diffuse light.[126] Despite having some success in waste water treatment, its use for water splitting has not been reported. Most of the reflectors used for water splitting experiments are compound parabolic collectors (CPCs) that allow some diffuse light to reach the reactor tube (Figure 9c). As shown in Figure 10a, its profile consists of two joint parabolas. Apparently, the ray traces show highly concentrated irradiation on the two sides of the reactor tube. To improve the uniformity of illumination on the tube surface, a new type of reflector geometry has been developed recently, named the surface uniform collector (Figure 10b).[127]
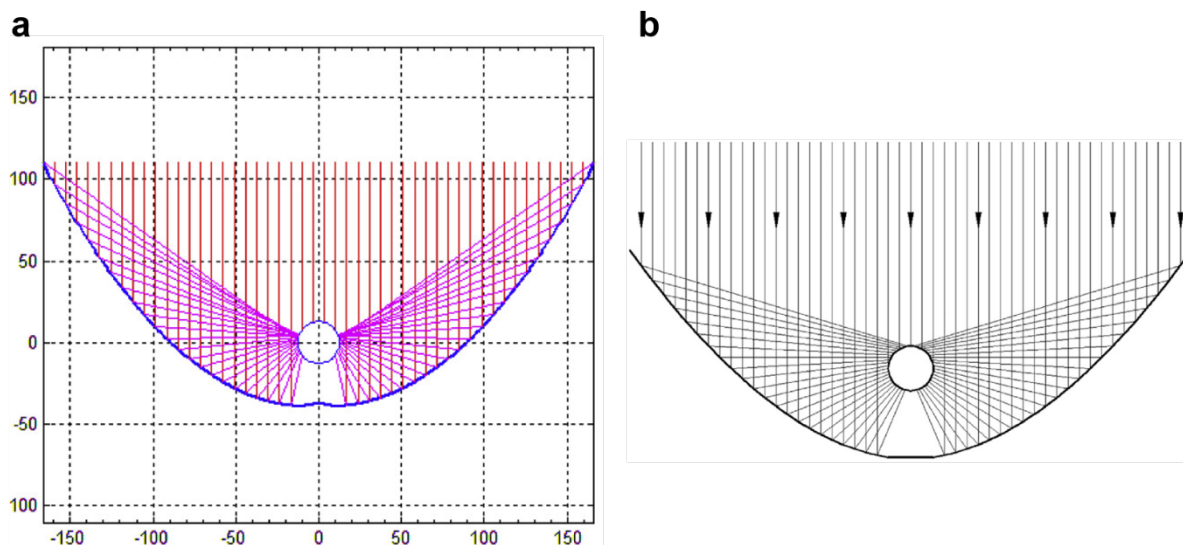
Figure 10. Cross-sectional views of (a) compound parabolic collector, reproduced with permission from Ref. [128], copyright (2018) Elsevier Ltd. and (b) surface uniform collector, reproduced with permission from Ref. [127], copyright (2016) Elsevier Ltd.

Optimization of the different reflector geometries has been performed, the theory of which is described in detail elsewhere and beyond the scope of this review.[129-130] The reflectors facilitate concentration of solar radiation, *i.e.* higher irradiance on the surface of the reactor than that of natural sunlight, which allows for the use of less photocatalyst and smaller reactor sizes compared with flat panel designs for unconcentrated sunlight. However, the quantum efficiency of the photocatalyst can decrease with irradiance because the increased charge carrier density also promotes recombination. In addition, in CPCs the amount of usable diffuse light decreases as the concentration factor increases. It is in principle possible to optimize the concentration factor of the reflector with respect to a certain catalyst, but research in this direction is scarce and difficult due to the complex kinetics of photocatalytic water splitting.[131]

2.3. Progress in pilot tests

Pilot-scale demonstration of photocatalytic water splitting has been limited due to low efficiency of catalysts, difficulties in engineering large reactors in a laboratory setting, and

economic considerations among other factors. As no commercial projects have been reported so far, we define the pilot-scale demonstration as any experiment that involves an illuminated geometric area exceeding 100 cm^2 or a total volume of slurry exceeding 1 L with natural sunlight only. The criteria were chosen as such because studies in smaller scales are readily performed using commercially available apparatus without particular engineering concerns. Table 2 summarizes the basic features and performance of the pilot plants.

The first pilot plant for photocatalytic water splitting was demonstrated in 2009.[132] It consisted of four tubular glass reactors connected in series, each coupled to a CPC with an illuminated area of 0.6 m^2. Optimized hydrogen production of 1.88 L/h corresponding to a STH of 0.47% was achieved. A unique feature of this pilot plant was its large solar concentration factor of ~4 in contrast to the typical value of ~1 in water treatment plants, which also characterized subsequent works from the same group.[127, 133-135] The difference between the design criteria of water splitting and water treatment plants, *i.e.* high rate of hydrogen production per unit reactor volume for the former and large throughput of waste water per unit plant area for the latter, was highlighted and contributed significantly to the decision of using the large light concentration factor. The water splitting process could therefore be intensified with less catalyst required. However, fast consumption of the sacrificial agents was found a problem that affected hydrogen production in extended experiments.

For further process intensification in a larger scale (32.4 m^2 of illuminated area in total), the CPC was redesigned to reduce its space requirements and stirring was facilitated by periodically bubbling compressed gas through the reactors instead of continuously recirculating the slurry by a pump.[133] Despite a high catalyst loading, the STH was remarkably lower than in the first example (Table 2). A similar design was adopted in the largest-scale study so far, involving a total illuminated area of 103.7 m^2 and 720 L of

photocatalyst slurry.[134] Figure 11 shows the structure of the plant. While the purpose of the design was to take maximal advantage of natural convection for the stirring of the photocatalyst slurry, forced recirculation had to be performed in the middle of the experiment due to severe sedimentation which was cited as the main reason for the low STH of 0.087%. Nevertheless, this attempt remains closest to a practical solar water splitting plant in terms of its scale and duration of test (6 h). The amount of hydrogen produced, 26.7 L/h, is remarkable. The same group also achieved a STH of 0.48%, the highest among pilot-scale experiments so far, with the surface uniform collector.[135]

Interestingly, in the abovementioned series of experiments better performance was obtained with forced recirculation. As reverse reactions were made insignificant by the use of sacrificial hole scavengers, the main mechanism of this performance enhancement seems to be more related to the efficiency of light absorption and/or transport of hole scavenger species near the catalyst surface.
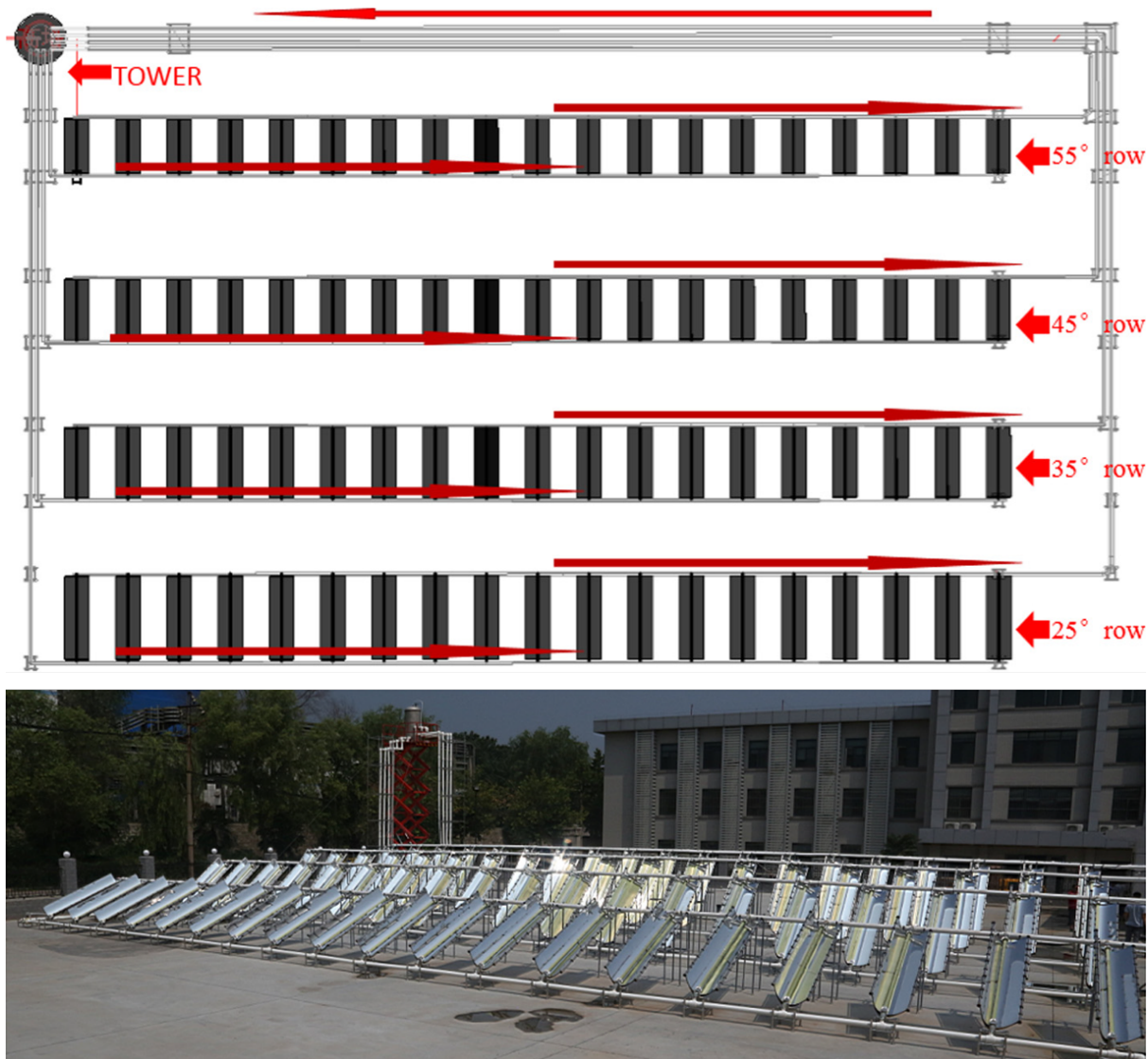
Figure 11. Schematic diagram and photo of a pilot plant for photocatalytic water splitting. Reproduced with permission from Ref. [134], copyright (2017) Elsevier Ltd.

Pilot tubular reactors with solar concentrators have also been used with organic hole scavengers. A few studies carried out in Plataforma Solar de Almería, Spain since 2013 demonstrated photocatalytic hydrogen evolution from aqueous formic acid, methanol, glycerol and organic wastewater.[136-138] The pilot plants had been designed for water treatment and thus, as discussed earlier, had solar concentration factors of ~1 to maximize the utilization of diffuse sunlight. The relative effectiveness of the hole scavengers were found to depend on the type of the catalyst, but in all cases the hydrogen evolution from wastewater was at least an order of magnitude slower than in the presence of other hole scavengers. Note

that in these works solar power was measured by radiometers only responsive to part of the solar spectrum, *i.e.* λ < 400 nm or λ < 550 nm, making it difficult to directly compare the performance with most literature data. Considering the contribution of the measured part to the total irradiance in a standard AM1.5G spectrum, the STH based on total solar irradiance is 3.8 and 22 times lower than the value reported based on λ < 550 nm and λ < 400 nm irradiance, respectively. While solar hydrogen evolution with concurrent wastewater treatment was proven possible, the low reaction rate along with peculiar consumption of already formed hydrogen and catalyst deactivation[138] renders the potential of the technology unclear for commercial hydrogen production.

As an alternative to the sophisticated solar concentration reactors, flat panel photoreactors have received efforts for scale-up due to their simplicity. The first pilot scale demonstration of this type was reported in 2014 using a Pt/g-C$_3$N$_4$ catalyst.[139] The photocatalyst slurry containing triethanolamine as sacrificial hole scavenger was recirculated by a pump between a reservoir and the reactor which had an illuminated area of 1 m^2 and a cavity thickness of 8 mm. Despite the continuous pumping, aggregation of the catalyst particles which could not be re-dispersed was observed during the experiment. This as well as the low UV transmittance of the reactor cover made of polycarbonate was believed to negatively affect the performance, resulting in only up to 0.08 L/h of hydrogen produced. To counter the problems, the reactor cover material was changed to poly(methyl methacrylate) for its better UV transparency and the catalyst immobilized on stainless steel supporting plates.[140] The pilot plant which was otherwise the same as that used in the previous work is shown in Figure 12. The rate of hydrogen production was improved by a factor of 2 even though the illuminated area was reduced. Regardless of the low average STH of 0.06%, it has been the longest running pilot-scale experiment (28 days) without replacement of catalyst in between.
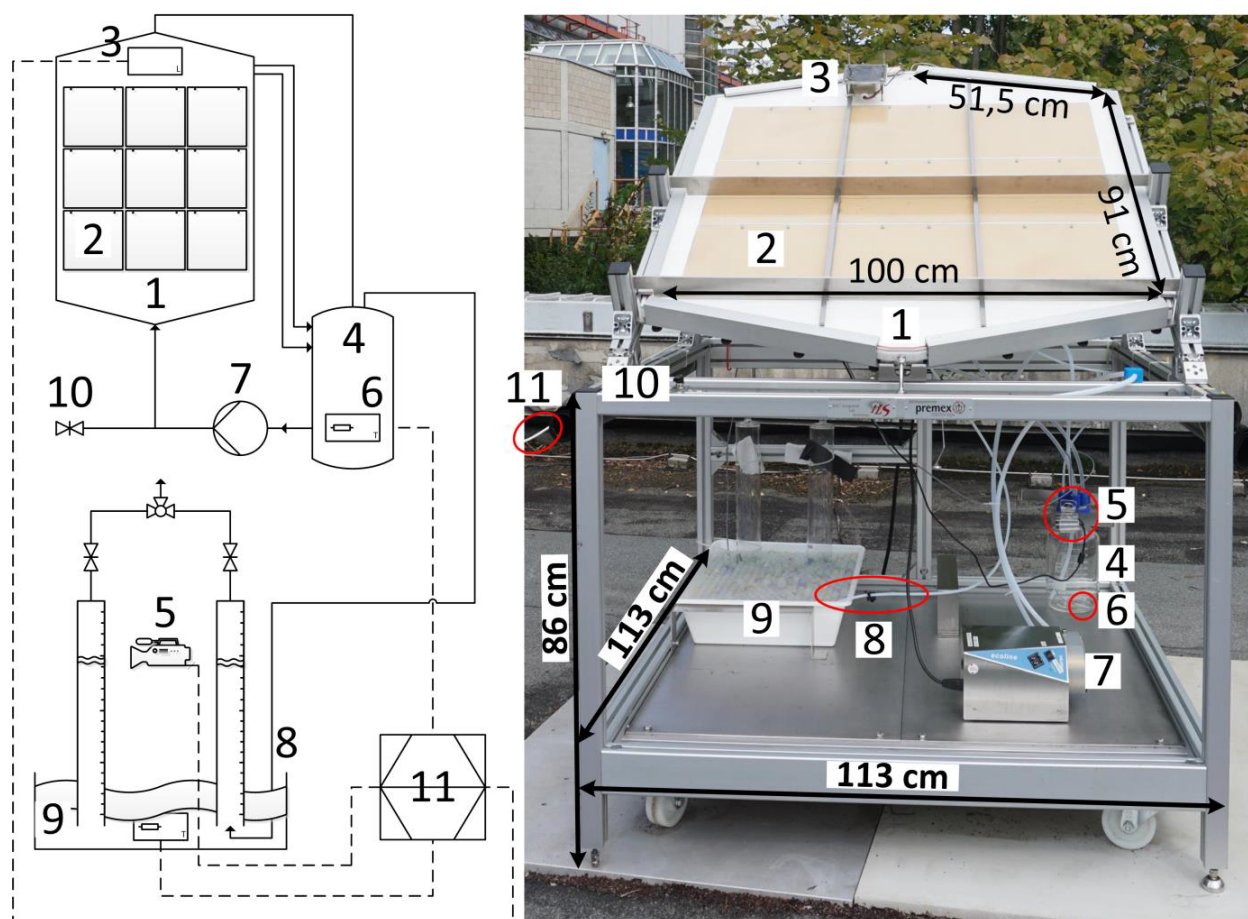
Figure 12. Schematic diagram and photo of a panel recirculation reactor system for photocatalytic hydrogen production with an immobilized Pt/g-C$_3$N$_4$ catalyst: 1, inlet of reactor; 2, reaction chamber; 3, light sensor; 4, storage tank for reaction medium; 5, camera for monitoring of hydrogen volume; 6, thermocouple; 7, pump; 8, gas line; 9, gas collection apparatus; 10, purge valve; 11, computer. Reproduced with permission from Ref. [140], copyright (2015) Wiley-VCH.

In all the examples introduced so far, sacrificial electron donors were consumed to facilitate hydrogen evolution, which significantly reduced the gain of chemically stored energy in the overall reaction compared with OWS. The only pilot-scale realization of pure water splitting was reported recently at the scale of 1 m^2 and reached a STH of 0.4%, which is remarkable considering that the photocatalyst (RhCrO$_x$/SrTiO$_3$:Al) was only sensitive to UV.[141] The reactor module is rather simple in design and is in theory readily scalable, as shown by Figure 13. Unfortunately, the test only lasted for 30 min and improvement of long-term stability, although achieved with laboratory-scale (25 cm^2) devices, was not demonstrated. It

is worth mentioning that the same group has developed equally or more efficient Z-scheme OWS devices by screen printing, an industrially established manufacturing process, but the performance was only measured with 25 cm² samples despite 100 cm² and 900 cm² examples being shown.[142-143] Apparently, the scale-up of unassisted photocatalytic OWS is much less studied than the already underdeveloped pilot-scale sacrificial photocatalytic hydrogen evolution.
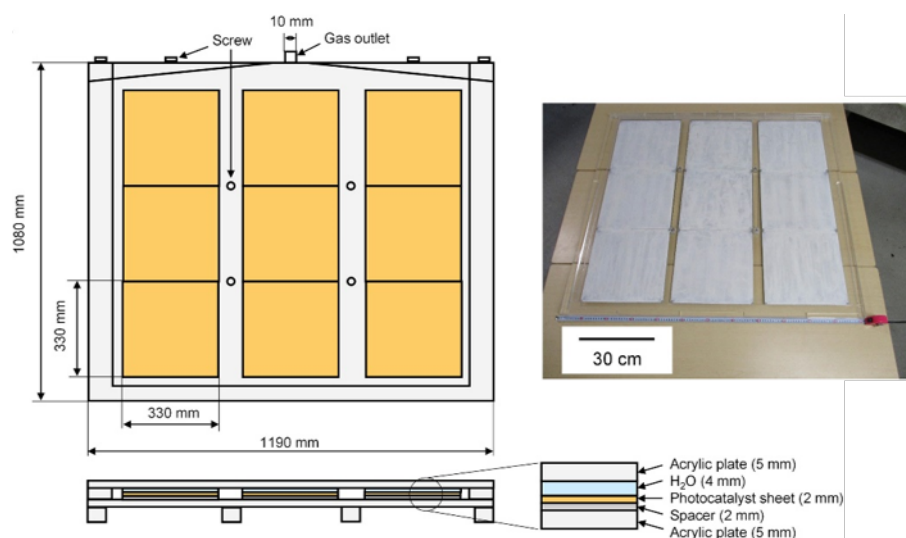

Figure 13. Schematic diagram and photo of a photocatalytic overall water splitting panel with an immobilized $RhCrO_x/SrTiO_3$:Al catalyst. Adopted and modified with permission from Ref. [141], copyright (2017) Elsevier Inc.

Table 2. Pilot-scale demonstrations of photocatalytic water splitting.

Reactor	Catalyst	Catalyst loading	Illuminated area (m²)	Total volume (L)	Sacrificial agent	Test duration	Average H₂ rate (L/h)	Max STH	Average STH	Ref.
Flat panel	Pt/g-C$_3$N$_4$	13 g/m²	0.756	-	TEOA	28 d	0.17	0.12%	0.06%	[140]
Flat panel	Pt/g-C$_3$N$_4$	0.62 g/L	1	11 L	TEOA	1 d	0.08	-	-	[139]
Flat panel	Pt/g-C$_3$N$_4$	0.62 g/L	1	11 L	TEOA	3 d	0.04	-	-	
Flat panel	RhCrO$_x$/SrTiO$_3$:Al	8 g/m²	1	-	None	30 min	1.02	-	0.4%	[141]
Tubular CPC	Pt/CdS	0.56 g/L	2.4	11.4 L	Na$_2$SO$_3$, Na$_2$S	6.5 h	~0.3	-	0.07%	[132]
Tubular CPC	Pt/CdS	1 g/L	2.4	11.4 L	Na$_2$SO$_3$, Na$_2$S	-	1.88	-	0.47%	[132]
Tubular CPC	Cd$_x$Zn$_{1-x}$S	0.5 g/L	1.53	75 L	Na$_2$SO$_3$, Na$_2$S	5 h	~1.3	~0.4%	0.35%	[127]
Tubular SUC†	Cd$_x$Zn$_{1-x}$S	0.5 g/L	1.53	75 L	Na$_2$SO$_3$, Na$_2$S	5 h	~1.8	~0.48%	0.38%	[127]
Tubular CPC	NiS/Cd$_x$Zn$_{1-x}$S	0.25 g/L	103.7	720 L	Na$_2$SO$_3$, Na$_2$S	6 h	26.7	~0.13%	0.087%	[134]
Tubular CPC	Cd$_x$Zn$_{1-x}$S	2.77 g/L	32.4	207 L	Na$_2$SO$_3$, Na$_2$S	3.5 h	10.3	-	0.12%	[133]
Tubular SUC	NiS/Cd$_x$Zn$_{1-x}$S	0.5 g/L	1.53	70 L	Na$_2$SO$_3$, Na$_2$S	3 h	2.15	~0.5%	0.48%	[135]
Tubular	Cd$_x$Zn$_{1-x}$S/TiO$_2$	0.5 g/L	-	1 L	S^{2-} waste water, Na$_2$SO$_3$	1.5 h	0.12	-		[144]
Tubular CPC	Pt/TiO$_2$:N	0.2 g/L	1.375	25 L	HCOOH	5 h	~0.34	2.5% <400 nm	-	[136]
Tubular CPC	Pt/Cd$_x$Zn$_{1-x}$S	0.2 g/L	1.375	25 L	HCOOH	5 h	~0.16	1.6% <400 nm	-	[136]
Tubular CPC	Pt/Cd$_x$Zn$_{1-x}$S	0.2 g/L	1.375	25 L	Municiple waste water	5 h	~0.02	-	-	[136]
Tubular CPC	Au/TiO$_2$	0.2 g/L	2.1	25 L	HCOOH	5 h	0.73	1.8% <550 nm	-	[137]
Tubular CPC	Au/TiO$_2$	0.2 g/L	2.1	25 L	Municiple waste water	5 h	~0.002	-	-	[137]
Tubular CPC	Cu/TiO$_2$	0.2 g/L	2.1	25 L	CH$_3$OH	5 h	0.04	-	-	[138]
Tubular CPC	Cu/TiO$_2$	0.2 g/L	2.1	25 L	Glycerol	5 h	0.14	2.6% <400 nm	-	[138]
Tubular	Pt/TiO$_2$	1 g/L	0.036	1.2 L	Pure CH$_3$OH	4 h	-	-	-	[145]

†SUC: surface uniform collector

3. Photobiological hydrogen production

Photobiological generation of molecular hydrogen was first reported in 1942.[146] Due to benign biochemical reaction conditions and theoretically negative carbon footprint, it has received increasing attention as a potential technology for commercial hydrogen production particularly in the past two decades. Photobiological hydrogen evolution activity has been mainly observed with microalgae, cyanobacteria, and purple non-sulfur bacteria (PNSB), following different mechanisms.[147] Microalgae and cyanobacteria exhibit direct biophotolysis of water through a process that overlaps with the light-dependent stages of photosynthesis.[148] As illustrated by Figure 14, electrons are extracted from water and transferred to the redox mediator ferredoxin, driven by photocatalytic reactions on photosystem 2 and 1 (PS2 & PS1), respectively. Instead of fixing CO_2 through the light-independent reactions of photosynthesis, the reduced ferredoxin donates electrons to hydrogenases which catalyze reversible HER using the protons derived from water.

In microalgae the enzyme responsible for HER, [FeFe] hydrogenase, is the most active type with turnover rates of up to 1000 s^{-1} and near zero overpotential.[149] However, due to extreme oxygen sensitivity of [FeFe] hydrogenase, the HER is quenched within minutes by the oxygen produced on PS2.[150-151] As the deactivation is irreversible and regeneration of [FeFe] hydrogenase requires strict anaerobic induction,[152] the process has limited practicality. A different enzyme, [NiFe] hydrogenase, catalyzes HER in cyanobacteria. It is constitutively expressed and reversibly deactivated by oxygen,[152] but less active than [FeFe] hydrogenase by a factor of ~100.[153] In some cases light-driven HER occurs with electrons and protons supplied by catabolism of stored organics that are photosynthesized by the same organism previously (Figure 14). This process of hydrogen production is named indirect biophotolysis. Although the theoretical maximum of STH can reach 14% for biophotolysis,[154] experimentally measured efficiency has usually been below 3%.[155] In light-limiting

conditions and purged with inert gas, continuous biophotolysis has been reported at energy efficiencies up to 24% based on photosynthetically active radiation, which is equivalent to approximately 10% STH.[153, 156] However, the practicality of hydrogen production in such conditions is remote at the best.
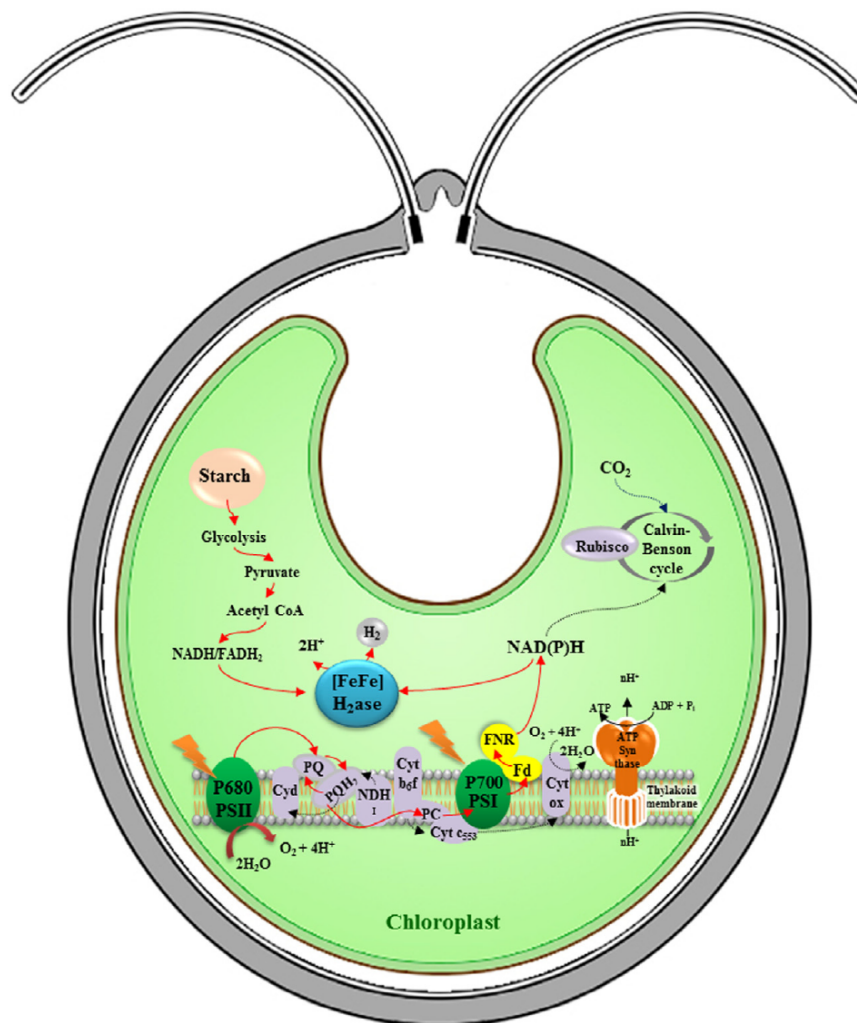

Figure 14. Simplified illustration of hydrogen-related metabolic pathways in green algae. Abbreviations; [FeFe] H2ase: [FeFe] hydrogenase, PSII: photosystem II, PSI: photosystem I; PQ/PQH2: plastoquinone pool, Cyt b6f: cytochrome b6f, PC: plastocyanin, Cyt c553: cytochrome c553, Cyd: quinol oxidase, Fd: ferredoxin, FNR: ferredoxin-NADP reductase, SDH: succinate dehydrogenase, NDH-I: NADPH dehydrogenase (complex I), Cyt ox: cytochrome c oxidase, OPP: oxidative pentose phosphate pathway, Rubisco: Ribulose-1,5-bisphosphate carboxylase oxygenase. Reproduced with permission from Ref. [148], copyright (2017) Elsevier Ltd.

Besides hydrogenases, nitrogenases also produce hydrogen as a by-product of nitrogen fixation. Catalyzed by the most commonly occurring Mo nitrogenase, one hydrogen molecule is produced with fixation of each nitrogen molecule (Equation 3). In the absence of nitrogen, only hydrogen is formed (Equation 4). Nitrogenases are responsible for hydrogen generation by nitrogen-fixing cyanobacteria and PNSB.

$$N_2 + 8H^+ + 8e^- + 16ATP \rightarrow 2NH_3 + H_2 + 16(ADP + Pi) \tag{3}$$

$$2H^+ + 2e^- + 4ATP \rightarrow H_2 + 4(ADP + Pi) \tag{4}$$
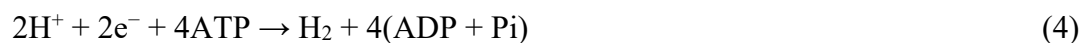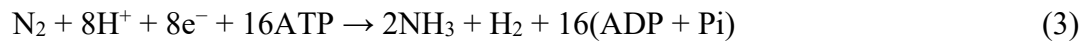
Due to the large amount of required energy input from ATP, the process is irreversible but on the other hand less efficient than hydrogenase-based biophotolysis.[157] Similar to hydrogenases, nitrogenases are inhibited by oxygen and in addition by fixed nitrogen sources particularly in the form of ammonia/ammonium, thus demanding careful supply of nutrition for optimal hydrogen production.[158] Moreover, to recycle the energy stored in hydrogen, hydrogenases that only catalyze HOR (known as uptake hydrogenases) are co-expressed with nitrogenases and reduce the efficiency of hydrogen production further.[157]

3.1 Photobiological strategies

Various genetic, metabolic, and reaction engineering strategies have been studied to improve the efficiency of photobiological hydrogen production, which include but are not limited to 1) selecting mutant species with deficiency in uptake hydrogenase or CO_2 fixing enzymes, 2) modifying the hydrogenase structure for enhanced oxygen tolerance, 3) starving the microorganism of sulfur to impede its PS2 function, 4) choosing appropriate carbon/nitrogen sources, 5) continuous culturing, and 6) cell immobilization.[159-164] The detailed approaches and mechanisms which have been extensively reviewed are drastically different from those of physicochemical processes, and thus beyond the scope of this article. In general, PNSB have led to the most practical success because of their flexible nutritional requirement and anoxygenic metabolism that avoids inhibition of nitrogenase by autogenous

oxygen, although they cannot oxidize water and depend on electron donors such as alcohols, carboxylic acids, and sugars for hydrogen production.[165-166] Taking acetic acid and glucose as model substrates, the process known as photofermentation can theoretically yield 4 and 12 moles of hydrogen per mole of substrate, respectively:

$$CH_3COOH + 2H_2O \rightarrow 4H_2 + 2CO_2 \qquad \Delta H^0 = +129 \text{ kJ/mol} \qquad (5)$$

$$C_6H_{12}O_6 + 6H_2O \rightarrow 12H_2 + 6CO_2 \qquad \Delta H^0 = +361 \text{ kJ/mol} \qquad (6)$$

3.2 Photobiological demonstrations

It should be noted that although the photofermentation reactions have large energy gain nominally, the actual hydrogen yield is much lower due to competitive metabolic pathways. Therefore for the technology to be economically viable, increasing efforts have been made to utilize low cost substrates such as food processing wastes and crop residues instead of pure chemicals.[167-169] Benefitting from development of photobioreactors for algal biorefinery, pilot studies on photofermentative hydrogen production have been more common and in larger scales than those on other methods of hydrogen production. Herein we highlight a few recent and notable pilot-scale examples, the operating conditions and performance of which are summarized in Table 3.

Table 3. Selected pilot-scale examples of photobiological hydrogen production.

Reactor	Microorganism	Substrate	Max. H$_2$ production rate (mmol/L·h)	Average H$_2$ production rate (mmol/L·h)	H$_2$ purity	Substrate conversion	Duration (days)	Ref.
Panel 1.4 L recirculation	Immobilized *R. capsulatus YO3*	Sugar beet molasses	0.79	0.6	-	50%	40 (recharged every 4 days)	[170]
Tubular 20 L recirculation	*R. capsulatus YO3*	Molasses	0.47	0.07	82.8%	-	17 (fed 3 times)	[171]
Baffled 4 m^3 continuous flow	Mixed PNSB	Hydrolyzed corn stalk pith	6.17	-	42-50%	81%	-	[172]
Tubular 9 L recirculation	*R. capsulatus YO3*	Molasses	0.31	0.11	32.6%	~100%	8 (fed every day)	[173]
Panel 1.4 L recirculation	Immobilized *R. capsulatus YO3*	Sucrose, glutamate	0.87	0.62	-	45%	20 (replaced every 4 days)	[174]
Baffled 4 m^3 continuous flow	Mixed PNSB	Glucose	3.96	-	43-47%	~95%	-	[175]
Baffled 8 m^3 continuous flow	Mixed PNSB	Hydrolyzed corn stover, CH$_3$COONa	-	8.0	68%	-	30	[176]

Similar with the case of photocatalytic water splitting, tubular flow reactors are often adopted in photobiological hydrogen production. In the example shown in Figure 15a, the bacteria were cultured in a recirculating hydrogen production medium which was regularly and partially replaced with fresh medium for feeding.[173] Solar concentration was not used, as photosynthesis microorganisms exhibit low tolerance towards heat and high irradiance. While the operation of such systems is simple, they suffer from unstable hydrogen production. Typically hydrogen production is most efficient in the exponential growth phase of the bacteria. It is difficult to maintain the growth phase at fluctuating temperature and irradiance in outdoor environments, and hydrogen production diminishes after the growth stops. In addition, the increasing biomass concentration reduces light penetration, also affecting hydrogen production. Flow reactors with constant feed/effluent to maintain the spatial distribution of culture density are thus preferred.

Recently, sustained photobiological hydrogen production in m^3-scale reactors has been reported. As illustrated in Figure 15b, bacterial inoculum and hydrogen production medium were constantly fed to the reactor. Stable hydrogen production of up to 1.5 kmol/day for 30 days has been demonstrated with an 8 m^3 photoreactor.[176] In this case, a dark fermentative hydrogen production stage preceded the photoreactor to convert carbohydrates to fatty acids, the preferred carbon source of photosynthesis bacteria, which has been proven to enhance the efficiency of hydrogen production. However, meticulous control of reaction conditions in such reactors is critical to the prevention of washout and the stable hydrogen generation. In the present example the operating temperature was maintained by a solar thermal water heater. A sophisticated illumination system consisting of fiber optics coupled to a solar concentrator and photovoltaic battery-powered light-emitting diodes was adopted to keep the illumination constant throughout the day. In contrast to photocatalytic water splitting, the solar radiation was diluted to 3000 lux to suite the need of bacterial growth (direct sunlight

43

has ~100000 lux). The accessory equipment significantly increases the capital cost of the system. To enhance the stability of the reactor and thus circumvent the complexity of control system, immobilization of the bacterial culture has been suggested as a solution. Figure 15c,d shows that the photosynthesis bacteria, fixed by agar, were anchored to a fabric support for use in a panel-type photoreactor.[174] Under direct sunlight without irradiance control, sustained hydrogen production for 40 days has been demonstrated. The substrate conversion efficiency was also significantly improved over tubular flow reactors involving suspended bacterial culture.
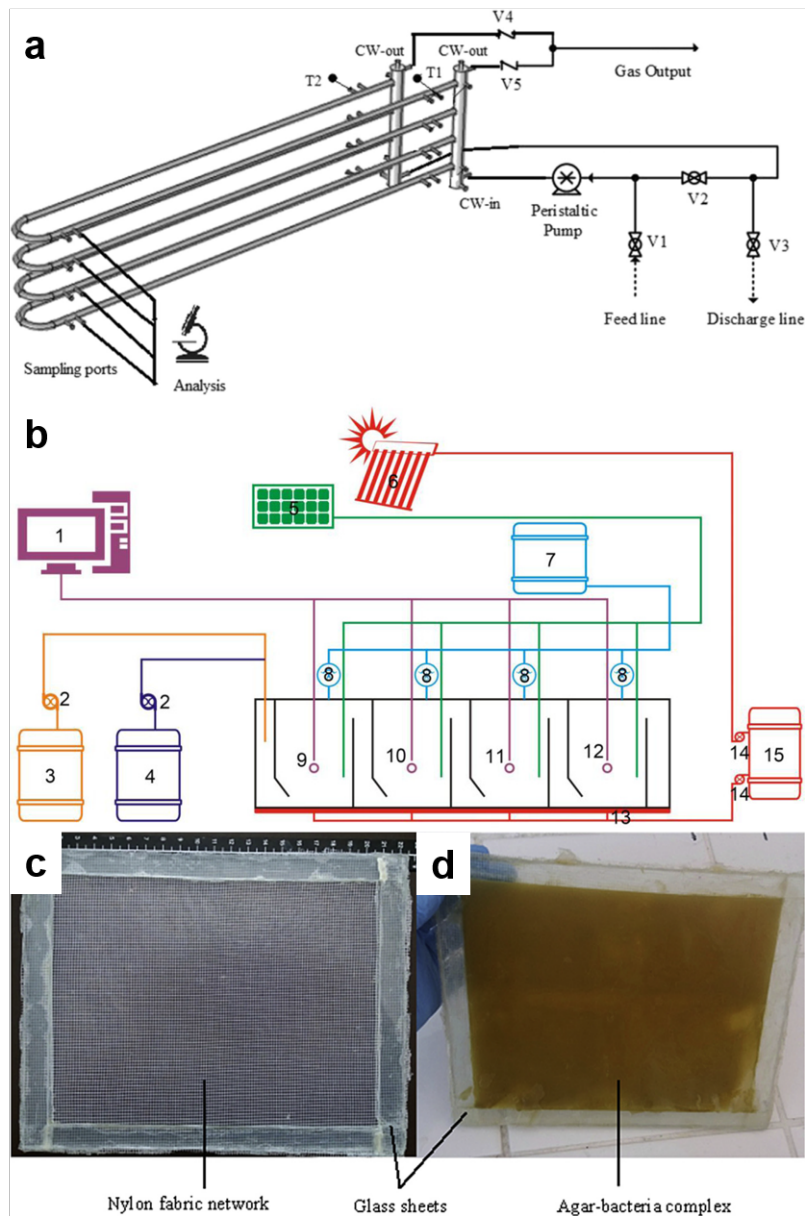
Figure 15. (a) Schematic diagram of a tubular recirculation photobiological hydrogen production set-up. Reproduced with permission from Ref. [173], copyright (2016) Elsevier Ltd. (b) Schematic diagram of a pilot plant for continuous flow photobiological hydrogen production: 1, control center; 2, peristaltic pump; 3, hydrogen producing medium tank; 4, photosynthesis bacteria tank; 5, fiber-optical solar import plant; 6, solar water heater; 7, gas tank; 8, gas flowmeter; 9-12, reaction chambers; 13, thermal insulation; 14, circulation pump; 15, hot water storage tank. Reproduced with permission from Ref. [175], copyright (2017) Elsevier Ltd. c,d) Photos of (c) fabric support for bacteria immobilization and (d) immobilized bacteria culture. Reproduced with permission from Ref. [174], copyright (2017) Elsevier Ltd.

4. Solar thermal water splitting

Solar thermal water splitting (STWS) involves concentrated solar radiation, which is used to maintain high temperature in a chemical reactor to drive chemical reaction, *viz.* water splitting, towards the production of storable and transportable hydrogen fuels (Figure 16). Various types of solar collectors and receivers have been developed and commercialized during the last few decades to serve for the solar thermal plants worldwide.[177-182] Therefore, it would be viable to simply integrate a thermochemical water splitting system into the existing solar collectors and receivers for large-scale hydrogen production.
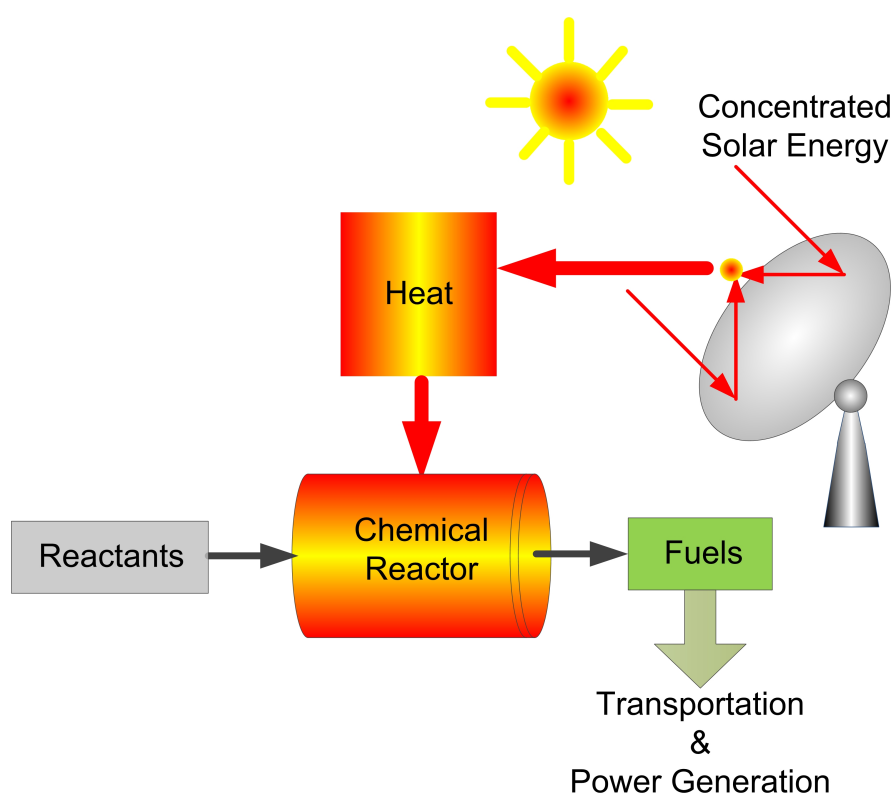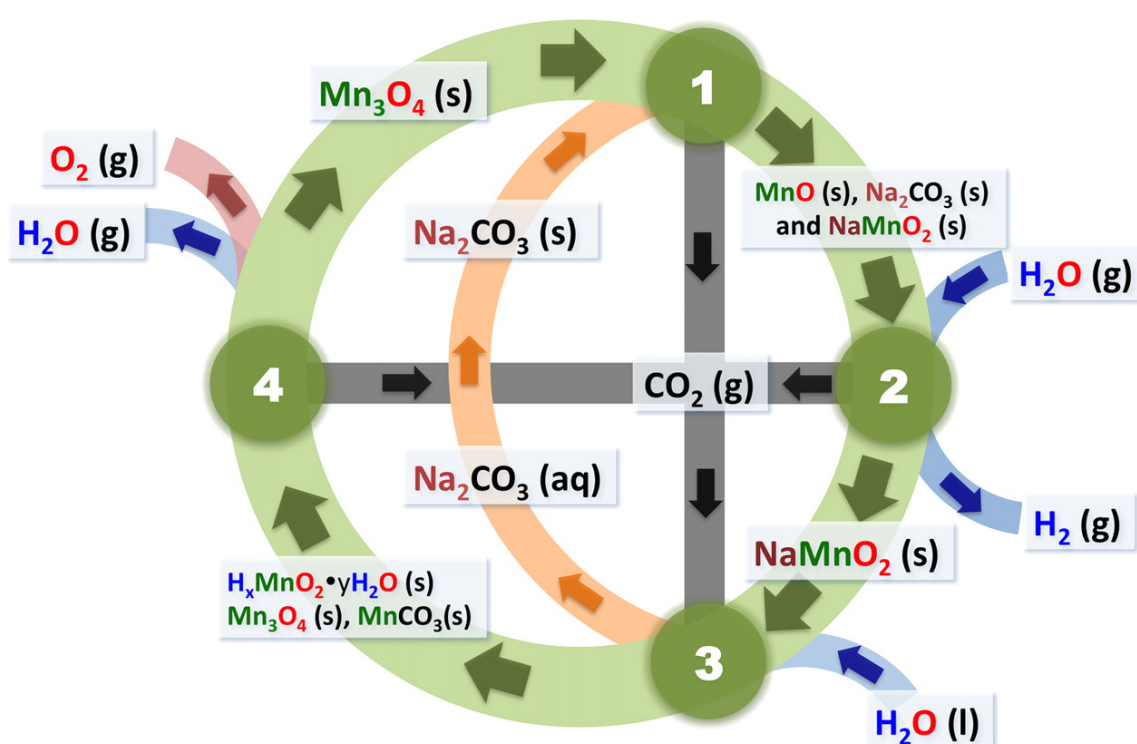

Figure 16. Schematic of solar thermal energy conversion into fuels.

4.1 Multistep cycles

Compared to direct thermolysis of water at above 2700 °C with low fraction of H_2 in the mixed products,[183] hydrogen and oxygen gases can be produced separately during a two-step or multistep water splitting process at lower temperatures with faster reaction kinetics.[184] Multistep cycles, *e.g.* sulphur-iodine process and hybrid copper chloride cycle, operate at

temperatures below 850 °C and commonly suffer from environmental issues, such as usage of harsh acids/bases and heavy metals.[185-186] However, a completely recyclable manganese-based thermochemical cycle has been reported without involving any toxic or corrosive components (Figure 17).[187] This system demonstrated good recyclability of at least 5 cycles and >90% yield for both hydrogen and oxygen evolution. By using manganese oxide nanoparticles instead of bulk material, lower operation temperature and faster hydrogen production rate were achieved.[188]

Step	Reaction	Temp (°C)
1	$3Na_2CO_3(s) + 2Mn_3O_4(s) \rightarrow 4NaMnO_2(s) + 2CO_2(g) + 2MnO(s) + Na_2CO_3$	850
2	$2MnO(s) + Na_2CO_3(s) + H_2O(g) \rightarrow H_2(g) + CO_2(g) + 2NaMnO_2(s)$	850
3	$6NaMnO_2(s) + ayH_2O(l) + (3 + b)CO_2(g) \rightarrow$ $3Na_2CO_3(aq) + aH_xMnO_2 \bullet yH_2O(s) + bMnCO_3(s) + cMn_3O_4(s)$	80
4	$aH_xMnO_2 \bullet yH_2O(s) + bMnCO_3 + \rightarrow$ $(2-c)Mn_3O_4(s) + ayH_2O(g) + bCO_2(g) + 0.5O_2(g)$	850
Net	$H_2O(g) \rightarrow H_2(g) + 0.5O_2(g)$	

a, b and c satisfy following relations: $a + b + 3c = 6$ and $(4-x)a + 2b + 8c = 18$

Figure 17. Schematic of the Mn-based multi-step thermochemical cycle for water splitting. Reproduced with permission from Ref. [187], copyright (2012) National Academy of Sciences.

In a typical two-step STWS, the first step (temperature T_{red}) is a reduction step, in which a metal oxide is reduced to the lower oxidation state under low oxygen partial pressure. Oxygen is generated at the same time during this endothermic step, as shown in the Equation (7). This reaction happens at a high temperature achieved by heating with concentrated sunlight. In the second step (temperature T_{oxd}), the reduced metal oxide reacts with water vapor that re-oxidizes the material and releases a stoichiometric amount of hydrogen, as shown in the Equation (8). This oxidation step normally requires a lower temperature than that for reduction step,[189-190] as $T_{red} > T_{oxd}$ is the thermodynamic driving force of the two-step process to make it thermodynamically favourable Equation (9). $\Delta G_{f,T_{oxd}}^{H_2O}$ is the Gibbs free energy change of H_2O formation. The entropy of O_2 is referred to as $S_{T_{red}}^{O_2}$. As $S_{T_{red}}^{O_2}$ increases with increasing T_{red}, small values of ΔT are thermodynamically achievable at high T_{red}.[191]

$$MO_x \rightarrow MO_{x-\delta} + \frac{\delta}{2}O_2 \tag{7}$$

$$MO_{x-\delta} + \delta H_2O \rightarrow MO_x + \delta H_2 \tag{8}$$

$$\Delta T = T_{red} - T_{oxd} = -2\Delta G_{f,T_{oxd}}^{H_2O} \Big/ \left(S_{T_{red}}^{O_2} \right) \tag{9}$$

It is worth noting that CO_2 can also be reduced to CO during the second step, which is the well know water-gas shift reaction. Ideally, a mixture of water vapor and gaseous carbon dioxide with optimized ratio will be utilized as reactants. The generated synthesis gas mixture can be catalytically converted to liquid hydrocarbon fuels such as gasoline, diesel and kerosene, through industrially available technologies (*e.g.* Fischer-Tropsch synthesis).[192-193]

Two-step redox cycles can be generally divided into two categories – volatile and non-volatile. With respect to volatile redox cycles, the metal oxides undergo gas-solid phase transitions. In contrast, metal oxides during non-volatile cycles maintain in the solid state. Non-volatile metal oxide redox cycles consist of two subcategories – stoichiometric and non-

stoichiometric cycles.[194] Several commonly investigated materials for two-step redox cycles are shown in Table 4.

Table 4. Common two-step metal oxide redox pairs.

Category	Cycle material	Reduction reaction	Ref.
Volatile	Zinc oxide	$ZnO(s) \rightarrow Zn(g)$	[195-197]
	Tin oxide	$SnO_2(s) \rightarrow SnO(g)$	[198]
Non-volatile (stoichiometric)	Iron oxide	$Fe_3O_4 \rightarrow FeO$	[199-204]
	Ferrite	$M_xFe_{3-x}O_4 \rightarrow xMO + (3-x)FeO$	[205-207]
	Hercynite	$Fe_3O_4 + 3Al_2O_3 \rightarrow 3FeAl_2O_4$ $M_xFe_{3-x}O_4 + 3Al_2O_3 \rightarrow (3-x) FeAl_2O_{4-x} + xMAl_2O_4$	[208-210]
Non-volatile (non-stoichiometric)	Ceria	$CeO_2 \rightarrow CeO_{2-\delta}$	[211-215]
	Doped ceria	$M_xCe_{1-x}O_2 \rightarrow M_xCe_{1-x}O_{2-\delta}$	[216-218]
	Perovskite	$ABO_3 \rightarrow ABO_{3-\delta}$	[219-220]

Volatile reactions generally demonstrate a better oxygen exchange capability than non-volatile reactions and the reduction process is thermodynamically more favourable. However, a highly demanding quenching step is necessary to avoid recombination and material loss is inevitable due to gas-phase deposition on the walls of the reactor, volatile cycles are therefore not viable for large-scale and long-term solar thermal hydrogen production. Amongst the proposed cycles in Table 4, ceria, doped hercynite and perovskite materials are the most promising candidates due to their lower reduction temperatures and fast reaction rates. Chueh *et al.* demonstrated high rate production of both H_2 and CO using porous cerium oxide (325 g in mass, 80% in porosity) in a solar cavity-receiver reactor (Figure 18).[211] The system maintained fairly stable and rapid fuel generation for over 500 cycles with solar-to-fuel efficiencies of 0.7 to 0.8%. The authors anticipated that both the efficiency and production rate can be substantially increased by reactor optimization and system integration. Thermodynamic analysis indicated that efficiency values of 16-19% are achievable based solely on the material properties of CeO_2, even in the absence of sensible heat recovery.[212]

Compared to the state-of-the-art material ceria, Sr- and Mn-doped perovskite $LaAlO_3$ showed 9 times greater H_2 yields when reduced at 1350 °C and re-oxidized at 1000 °C.[220] Moreover, during the reduction process, its onset temperature for O_2 evolution was 300 °C

lower than that of CeO_2. This perovskite oxide also had excellent durability without any noticeable degradation in fuel production rate during 80 redox cycles. Later, Weimer and co-workers reported isothermal water splitting at 1350 °C using hercynite cycle, which exhibited over 12 times larger H_2 production capability than that of ceria, per mass of active material when reduced at 1350 °C and reoxidized at 1000 °C.[210] Compared to previous redox cycles with temperature swings between reduction and oxidation steps, this isothermal process demonstrated more favourable kinetics and thermodynamics towards hydrogen production. Its thermodynamic driving force came from the large pressure swing in the gas composition between reduction and oxidation processes. In addition, it reduced both irreversible heat losses and thermal shock concerns that limit the efficiency and operations of traditional temperature-swing water splitting.
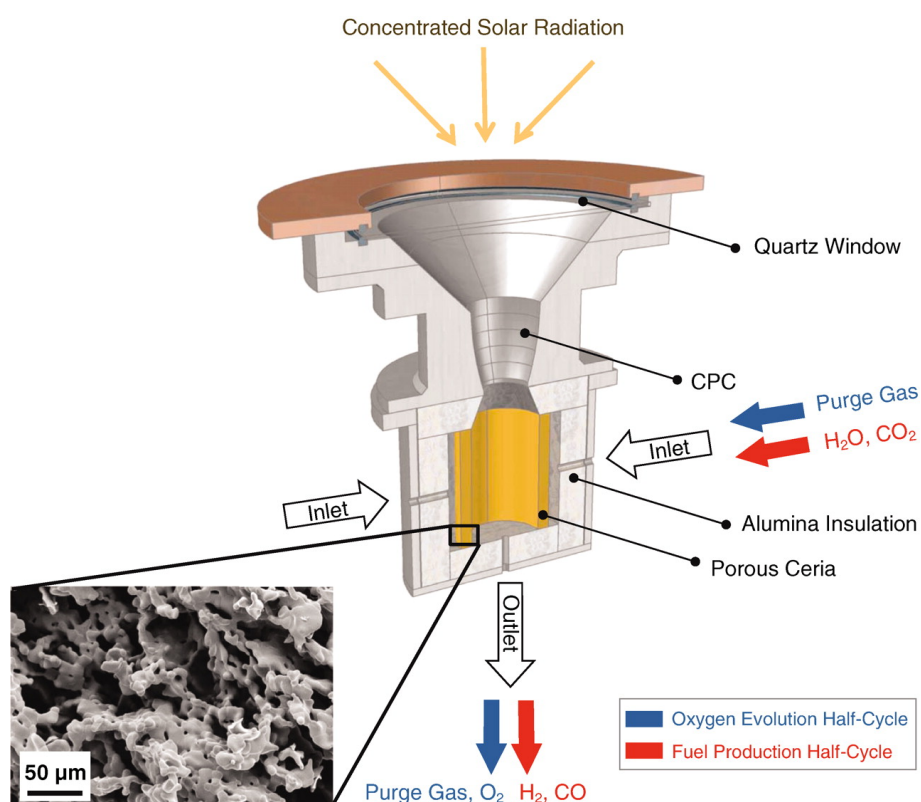

Figure 18. Schematic of the solar reactor for the two-step, solar-driven thermochemical production of fuels. It comprises a thermally insulated cavity receiver with a porous monolithic ceria cylinder. Concentrated solar radiation enters through a windowed aperture and impinges on the ceria inner walls. Reacting gases flow radially across the porous ceria

toward the cavity inside, whereas product gases exit the cavity through an axial outlet port at the bottom. Inset is the scanning electron micrograph of the porous ceria tube after 23 cycles. Reproduced with permission from Ref. [211], copyright (2010) American Association for the Advancement of Science.

4.2 Solar thermal scaleup

In 2015, Steinfeld and co-workers experimentally demonstrated the first ever production of jet fuel via a thermochemical H_2O/CO_2-splitting cycle using reticulated porous CeO_2 foam under simulated concentrated solar radiation of up to 3000 suns (Figure 19).[221] Solar-to-fuel energy conversion efficiency of 1.72% was achieved with good stability of 291 consecutive redox cycles, yielding a volume of 700 standard liters of syngas with the composition of 33.7% H_2, 19.2% CO, 30.5% CO_2, 0.06% O_2, 0.09% CH_4, and 16.5% Ar. The gaseous products were subsequently compressed and further processed via Fischer-Tropsch synthesis to generate a mixture of liquid hydrocarbons including 17.1 wt % naphtha, 35.6 wt % kerosene, 17.1 wt % gasoil and 30.2 wt % of heavier fractions. This work demonstrated the technical feasibility of the solar thermal redox process at operating conditions, towards industrial scale implementation of solar-to-fuel conversion.
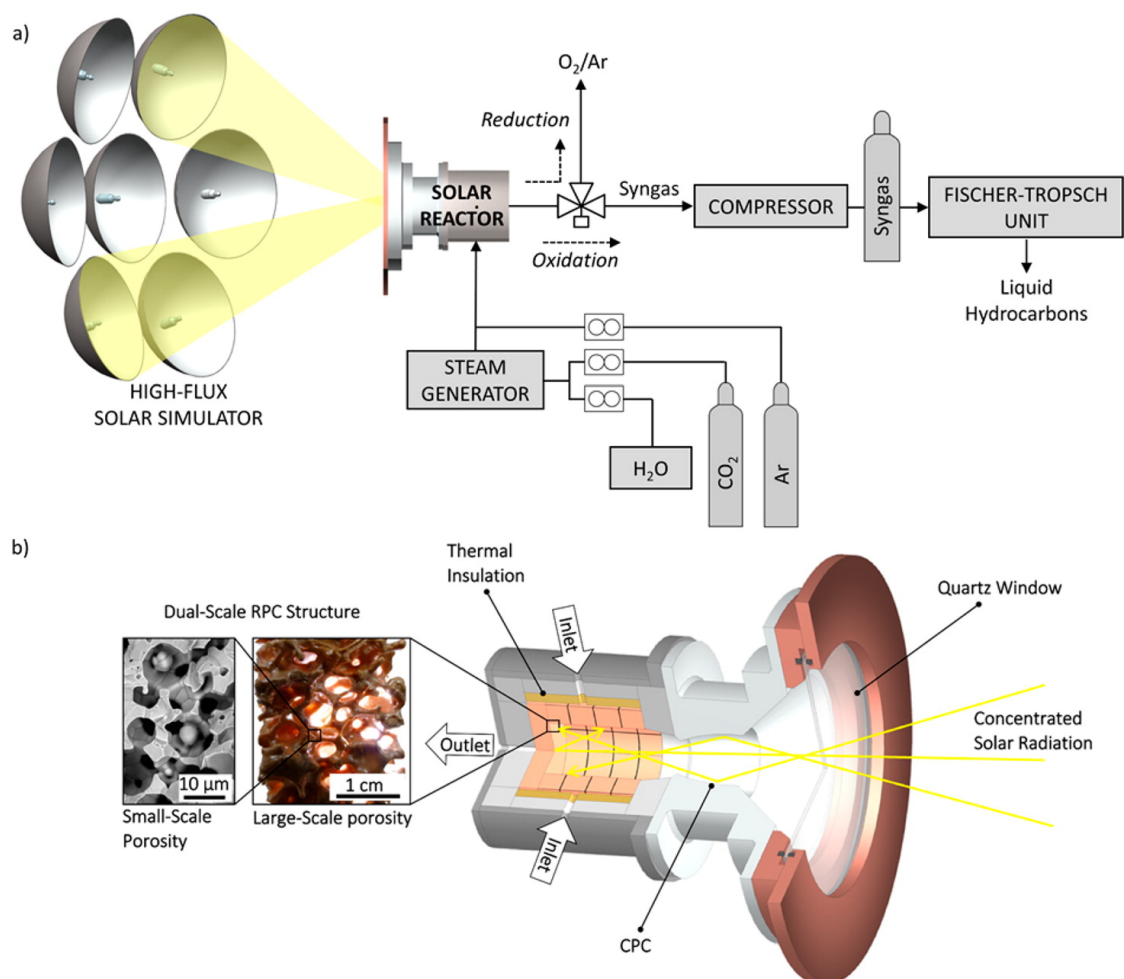
Figure 19. (a) Schematic of the experimental setup with the main system components for production of solar kerosene from H_2O and CO_2 via the ceria-based thermochemical redox cycle. (b) Schematic of the solar reactor configuration. The cavity-receiver includes a reticulated porous ceria structure with both millimetre- and micrometre-scale porosity. Reproduced with permission from Ref. [221], copyright (2015) American Chemical Society.

Although significant efforts have been made to develop new redox active materials and new solar thermal reactor concepts, the reported solar-to-fuel efficiencies are still far below 10%. Amongst various possible STWS cycles, two-step cycles are most promising to achieve economical large-scale hydrogen production with high conversion efficiency.[184] Compared to the current standard STWS material ceria which has been extensively investigated for years,[222] perovskite materials and doped-hercynite show more advantages such as lower reduction temperature, higher fuel production rate and larger fuel production capacity. Future research should concentrate on the development of these materials and solar reactors based

on flowing particles (Figure 20).[184] The solar reactor design could be potentially adapted from the reactor systems proposed for chemical looping hydrogen production, driven by solar heat instead, which have been previously summarised.[223-224]
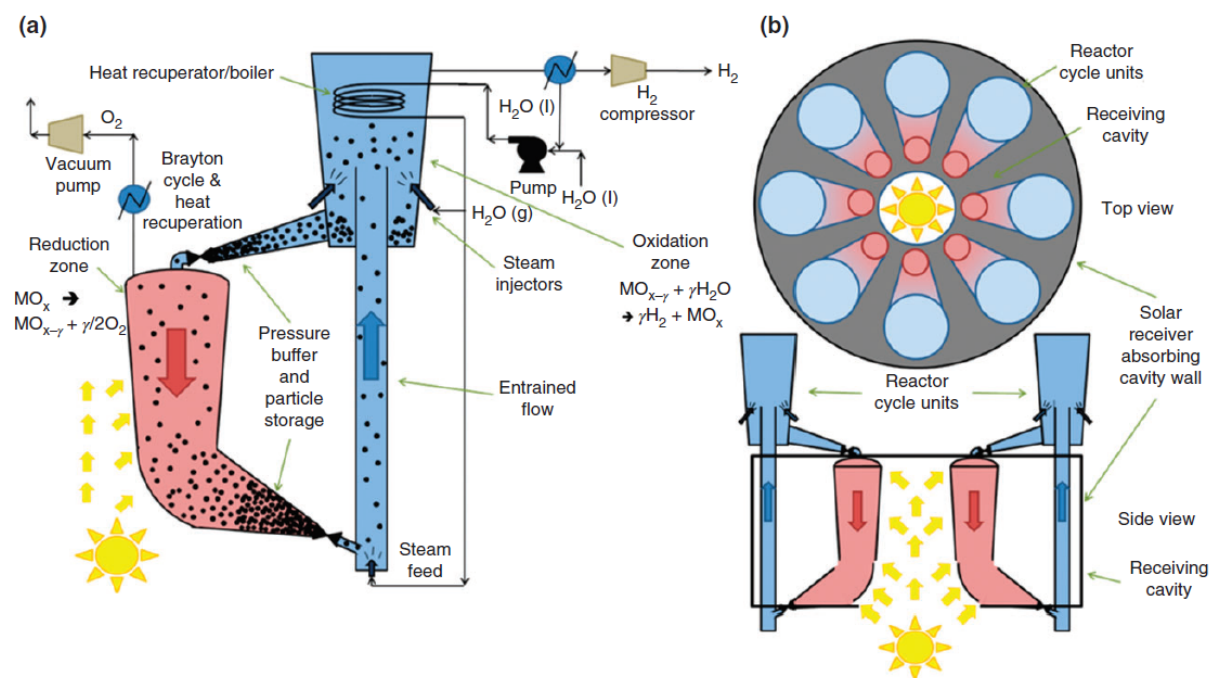

Figure 20. Schematic of the solar thermal particle flow reactor. (a) An individual reduction/oxidation reactor unit and (b) receiver configuration containing multiple reduction/oxidation reactor units. Reproduced with permission from Ref. [184], copyright (2015) John Wiley and Sons.
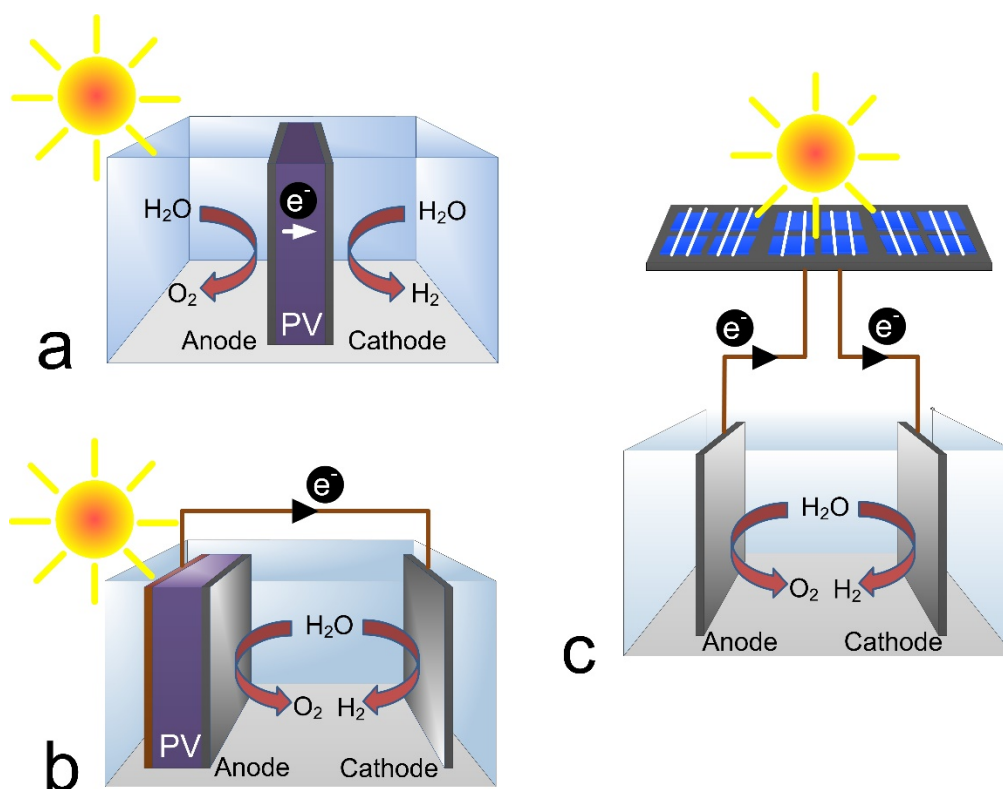
5. Photoelectrochemical water splitting

Figure 21. Schematic of three photoelectrochemical water splitting approaches. (a) Fully integrated/wireless PEC device; (b) partially integrated/wired PEC device; (c) non-integrated/modular PEC device.

Photoelectrochemical (PEC) water splitting devices convert the energy of photons to chemical energy, which consist of three approaches to couple the light harvesting and water splitting components, allowing room temperature operation of a reaction with ΔG^o of +237 kJ per mol of H_2 or 1.23 eV per electron. In fully integrated/wireless PEC devices, the light absorber and water splitting catalysts are in physical contact, as shown in Figure 21a. In partially integrated/wired PEC devices, oxidation reaction or hydrogen evolution catalyst is in physical contact with the light absorber, while the other catalyst on the other electrode is connected through external wiring (Figure 21b). In contrast, non-integrated devices known as modular systems consist of two separate units, *i.e.* photovoltaic (PV) cells and electrolyser that are combined via external wiring (Figure 21c). Regardless of the types of PEC devices,

the key system requirements towards large-scale hydrogen production are efficiency, stability and scalability (Figure 22). Beginning with the discovery of TiO_2 photoelectrodes for water splitting reported in 1972,[225] to date there is no PEC device that satisfies all these key requirements although absorbers, catalysts and membranes exist that are individually efficient, robust and scalable.[226] Therefore, it is critical to fabricate an integrated PEC system with each component operating under mutually compatible conditions.
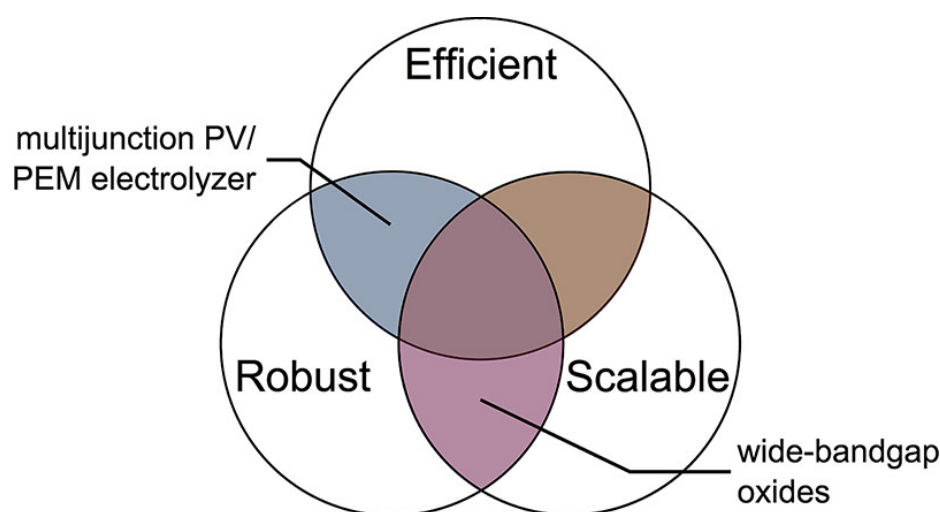

Figure 22. Venn diagram showing the three key requirements for viable solar-driven water-splitting devices. The materials that satisfy two out of the three requirements are highlighted. Reproduced with permission from Ref. [226], copyright (2014) American Chemical Society.

5.1 Fully integrated/wireless devices

5.1.1 Fully integrated PV-electrocatalysts devices

In 1998, Rocheleau *et al.* demonstrated this system by integrating sputtered $NiFe_{0.19}O_{2.2}$ OER catalysts and $Co_{0.73}Mo_{0.27}$ HER catalysts into triple junction amorphous silicon solar cells.[227] The tests were conducted in 1 M KOH with photoactive solar cell area of 0.27 cm^2 and electrode areas of 1 cm^2. A STH efficiency of 7.8% was achieved. The catalysts were separately tested in 1 M KOH and showed no degradation of catalytic activity for over 7200 h. During outdoor testing of the PEC device, the STH conversion efficiency dropped in the late afternoon due to the decreased blue portion of the solar spectrum. Later a similar water

splitting system was reported by Nocera and co-workers.[228] Co-borate OER catalyst and NiMoZn HER catalyst were coupled with a commercially available triple-junction amorphous Si PV. The 1×2 cm^2 wireless device demonstrated a STH efficiency of 2.5% in a mixture of 0.5 M KBi and 1.5 M KNO$_3$ electrolyte under AM 1.5 illumination (1 sun). In comparison, a wired device achieved higher efficiency of 4.7% in 1 M potassium borate (pH 9.2). A larger wireless Pt/TiO$_2$/InGaP/GaAs/Ge/IrO$_x$ water splitting device, with an area of 6.25 cm^2, demonstrated an initial STH efficiency of 11.2% and 10% photocurrent loss after 9 h in 3 M KHCO$_3$ under 1 sun illumination.[229] To achieve intrinsically safe photoelectrolysis without producing a flammable, potentially explosive mixture of H$_2$ and O$_2$ in the reactor, Atwater and co-workers constructed a membrane-based wireless prototype for solar-driven water splitting (Figure 23a).[230] The tandem-junction GaAs/InGaP light absorbers were protected by 150 nm ALD-TiO$_2$ layer and coupled with sputtered Ni OER and Ti/Ni-Mo HER electrocatalysts, respectively. An initial STH conversion efficiency of 8.6% was achieved under 1 sun illumination in 1.0 M KOH electrolyte (Figure 23b). However, the gas production rate decreased by ~10% after 4 h operation of the monolithically integrated device, likely due to the inhomogeneous protection coating on the light absorbers.
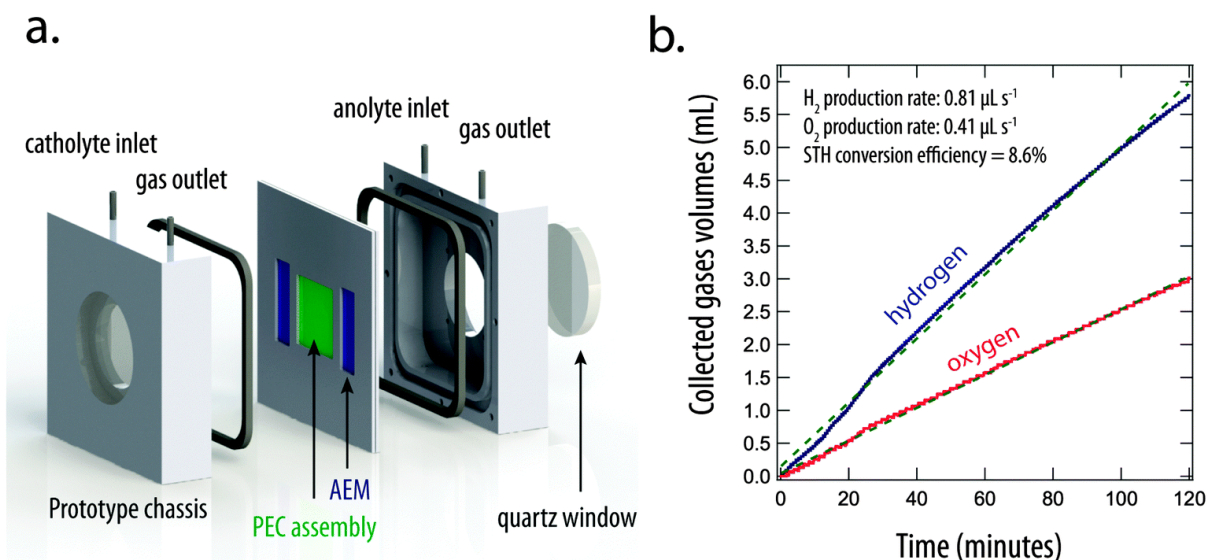
Figure 23. (a) Schematic representation of a fully integrated intrinsically safe, solar-hydrogen system prototype. (b) Collected hydrogen and oxygen as a function of time for the integrated prototype (active area = 1.0 cm^2 for both the photoanode and cathode) under 1 sun illumination in 1.0 M KOH. The estimated production rates (dashed lines) for H$_2$ and O$_2$ are 0.81 μL s^{-1} and 0.41 μL s^{-1}, respectively. Reproduced with permission from Ref. [230], copyright (2015) The Royal Society of Chemistry.

5.1.2 Fully integrated photoelectrode-PV devices

Perovskite solar cells, as the fastest-advancing solar technology to date, have also been utilized to fabricate solar-driven water splitting systems.[231-232] However, due to the intrinsic vulnerability of perovskites to moisture, such systems degraded rapidly under the reported operating conditions. In 2015, Kim *et al.* achieved 12 h continuous water splitting in 0.1 M bicarbonate electrolyte by combining in tandem a CH$_3$NH$_3$PbI$_3$ perovskite single junction solar cell with hydrogen-treated and Mo-doped BiVO$_4$ (Figure 24).[233] The wireless device produced stoichiometric H$_2$ and O$_2$ with an average STH efficiency of 3.0% using cobalt carbonate and platinum as OER and HER catalysts, respectively. In addition, a 1.7 cm^2 triple junction polymer solar cell for light absorption was combined with RuO$_2$ as both OER and HER catalysts for photoelectrochemical water splitting. Its STH efficiency is 3.6%, which is 33% lower than that of a small area solar cell (<0.1 cm^2). This system is not stable with ~5% current loss during 20 min operation in 1 M KOH electrolyte.
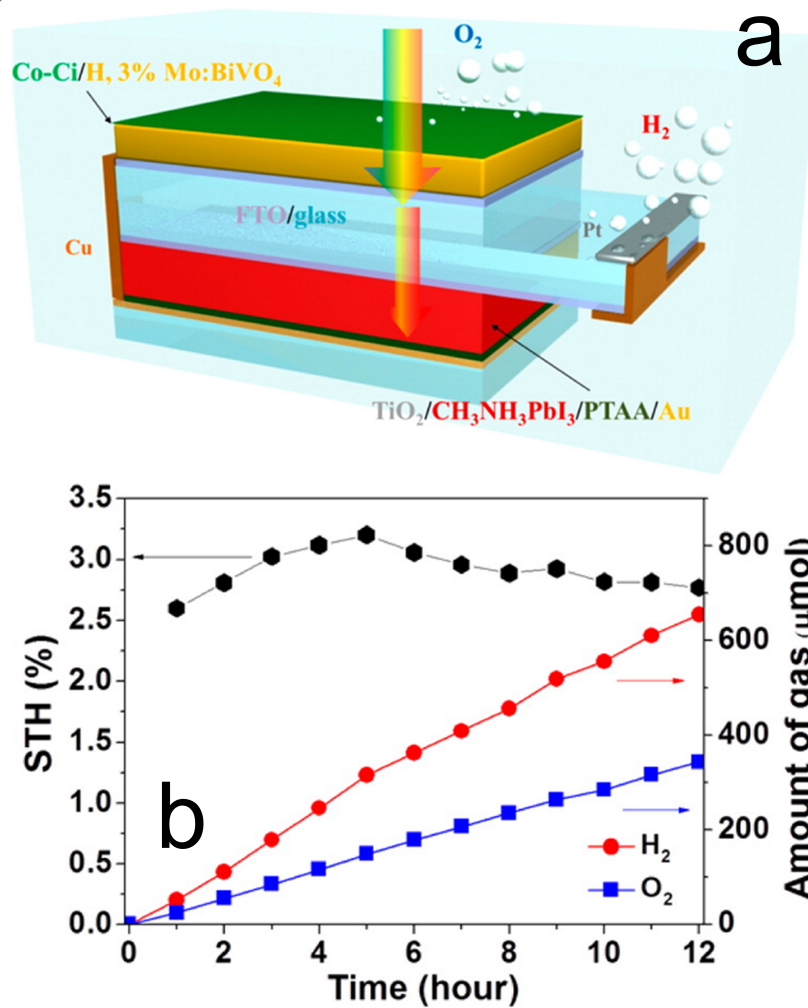
Figure 24. (a) Schematic of the wireless artificial leaf solar hydrogen generator. Configuration composed of first absorber (Co-Ci/H, 3% Mo:BiVO$_4$) and second absorber (TiO$_2$/ CH$_3$NH$_3$PbI$_3$) tandem cells. (b) Gas evolution and calculated STH of the artificial leaf (1.3 cm^2) under AM 1.5G, 100 mW cm^{-2}. Reproduced with permission from Ref. [233], copyright (2015) American Chemical Society.

The fully integrated/wireless devices generally exhibit lower STH efficiency than wired ones,[228, 233] although high efficiencies of up to 16-19% have been reported using very costly semiconductors.[234-235] Encapsulation or protection layer is usually needed to prevent the vulnerable solar cells from touching the electrolytes. Moreover, the generated hydrogen/oxygen bubbles and the integrated OER/HER catalysts could potentially lead to optical losses due to absorption and/or scattering by them, thus decreasing the light absorption of the solar cells and limiting the STH efficiency of the whole system. However,

compared to wired solar-driven water splitting devices, the fabrication costs can be significantly reduced by integrating the PV and electrolysis components into a single, monolithic device.[236-237]

5.2 Partially integrated/wired devices

5.2.1 Partial integrated PV-electrolysis devices

One of the earliest and highly publicized examples of these partially integrated water splitting devices was reported by Khaselev and Turner in 1998.[238] In this device, a p-type GaInP$_2$ photocathode was biased with a single GaAs p-n junction. The GaAs bottom cell provided sufficient voltage to overcome energetic mismatch between the band edges of the GaInP$_2$ and the water redox reactions, as well as additional voltage needed to overcome overvoltage losses from OER and HER. This resulted in an impressive STH efficiency of 12.4%. More recently, Verlage *et al.* utilized a tandem-junction photo-absorber consisting of an InGaP top cell and GaAs bottom cell for unassisted solar-driven water splitting. The 0.031 cm^2 photoanode was wired to a ~1 cm^2 Ni-Mo cathode and separated by an anion-exchange membrane (Figure 25a). The photocurrent of this system decreased by ~15% over 80 h operation under 1 sun illumination in 1.0 M KOH aqueous solution (Figure 25b).
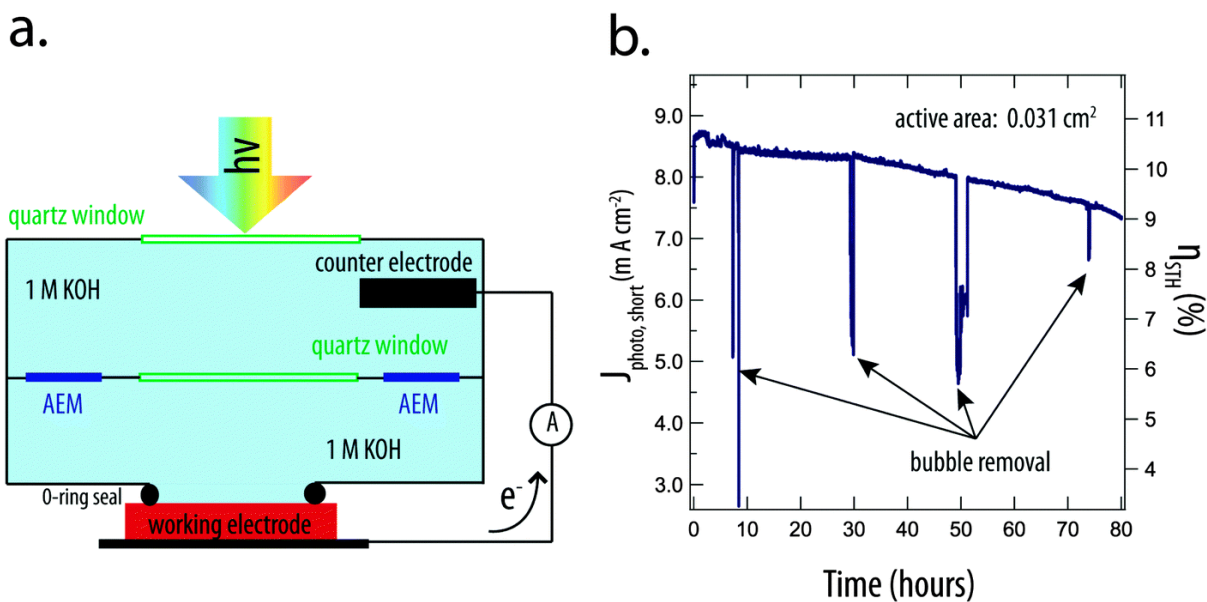
Figure 25. (a) Schematic illustration of the PEC cell configuration. The photoanode and the cathode were separated by an anion-exchange membrane. (b) The short-circuit photocurrent density and the corresponding STH efficiency, as a function of time under 1 sun illumination in 1.0 M KOH aqueous solution. Reproduced with permission from Ref. [230], copyright (2015) The Royal Society of Chemistry.

In 2016, based on laser-patterning technology used for the series connection of thin-film solar cells, Turan *et al*. proposed and realized a concept which is scalable to large area photoelectrochemical water splitting.[239] The scalability was simply achieved by continuous repetition of a base unit, consisting of either a series connection of three a-Si:H single-junction cells or two a-Si:H/μc-Si:H tandem cells connected in series (Figure 26a). Bare nickel foam was used for both anode and cathode in 1 M KOH electrolyte. An upscaled device with an active area of 52.8 cm^2 and 13 base units was demonstrated with a STH efficiency of ~3.9% (Figure 26b). The similar gas production rate per unit area between the upscaled and single base unit device confirmed the good scalability of the concept.
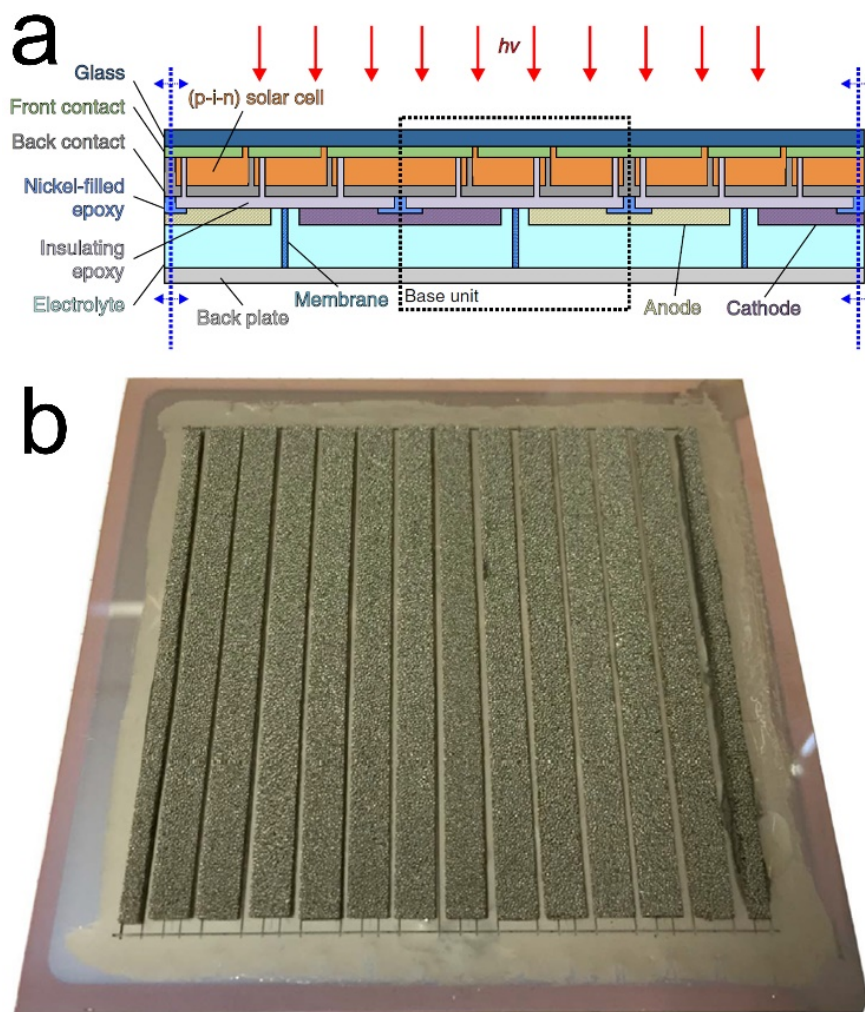
Figure 26. (a) Schematic of the device cross-section, depicting the device structure of a scalable photovoltaic water-splitting device in the superstrate configuration. The number of cell stripes in series can be easily adjusted (three in this case). The configuration is extendable in both directions (hinted by the dashed blue arrows). The base unit that defines the region of periodic repetition is highlighted by the dashed box. (b) Photograph of a large-scale photovoltaic water-splitting device. The total device area was 64 cm^2 with an active area of 52.8 cm^2. Each base unit consists of two series-connected a-Si:H/μc-Si:H tandem solar cells with a cell stripe width and length of 2.5 and 80 mm, respectively. Thirteen base units were mounted on a 10×10 cm^2 substrate. The back end was made of nickel-foam elements for both cathodes and anodes. Reproduced with permission from Ref. [239], copyright (2016) Nature Publishing Group.

5.2.2 Photoanode–photocathode tandem devices

Another possible strategy towards unassisted solar-driven water splitting is to combine a photoanode and a photocathode in tandem to carry out OER and HER, respectively. This system is also known as a multicomponent Z-scheme PEC cell. Its STH efficiency is determined by the crossover of overlaid current-voltage curves of the individual photoanode and photocathode.[240] The efficiency of the integrated PEC systems is limited by a lack of photovoltage from commonly used photocathodes as well as from insufficient photocurrent from typical photoanodes (Figure 27).[241] Various attempts using photoanode-photocathode combination have been made, such as NiOOH/FeOOH/Mo:BiVO$_4$-Pt/CdS/CuGa$_3$Se$_5$/(Ag,Cu)GaSe$_2$,[242] BiVO$_4$-InP,[241] CdS/TiO$_2$-CdSe/NiO,[243] BiVO$_4$-Rh:SrTiO$_3$.[244] However, the STH conversion efficiency of these PEC systems was not high (less than 1%). Additionally, their stability and scalability were other major issues inhibiting large scale fabrication of this system.
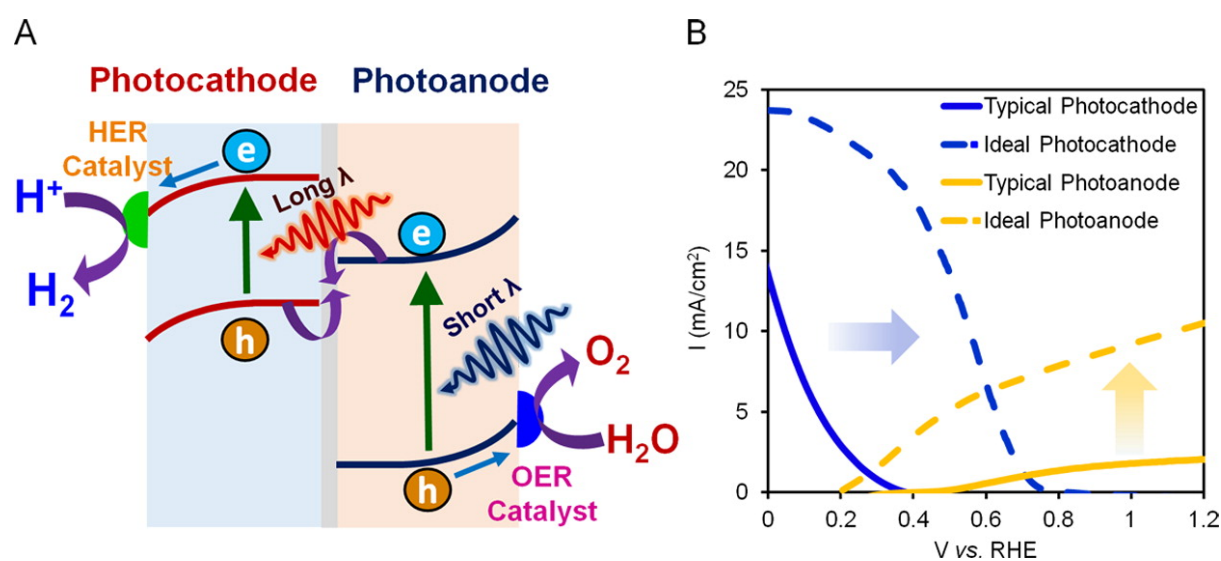
Figure 27. (A) Illustration of a photoanode–photocathode tandem system. (B) Photocurrent-potential curves for typical and ideal photoelectrodes. Reproduced with permission from Ref. [241], copyright (2016) American Chemical Society.

Some other enlightening studies toward large scale fuel production focused on upscaling of the individual photoelectrode, improvement of their long-term stability or development of highly scalable synthesis method of active semiconductor nanostructures. Pareek *et al*.

deposited 9×9 cm^2 nanorod-structured CdS films via spray pyrolysis for hydrogen production in the electrolyte of Na$_2$S and Na$_2$SO$_3$ solution under 80 mW/cm^2 light irradiation.[245] However, this system is not viable for long-term operation as sacrificial agents were utilized. By comparing LaTiO$_2$N photoanodes with the size of 1 cm^2 and 40 cm^2, Dilger *et al*. concluded that scale-up did not affect the faradaic efficiency but significantly decreased photocurrent density, which is due to insufficient charge transport.[246] Although some lab-scale demonstration using photoanodes such as Ta$_3$N$_5$ showed an excellent photoresponse with a high photocurrent approaching its theoretical photocurrent limit, its poor photostability inhibited its usage for practical application.[86]

Earth-abundant and intrinsically stable hematite can theoretically achieve a STH efficiency of 16.8%, which is comparable to that of Ta$_3$N$_5$.[247] Its excellent photostability for water oxidation was confirmed by Dias *et al.* using 19 nm thick hematite films prepared by spray pyrolysis without any dopants and co-catalysts.[248] The photoanodes maintained a constant photocurrent density of ca. 0.95 mA cm^{-2} at 1.45 V vs. RHE over 1000 h simulated solar illumination in 1 M NaOH electrolyte solution, showing no evidence of hematite film degradation or photocurrent density loss. Nevertheless, its low electron mobility, short hole diffusion length and very short excited-state lifetime have resulted in its poor PEC performance. Extensive efforts have been devoted to enhancing its photoactivity, such as adding electronic dopants and surface/interface engineering.[247, 249] One of the most efficient hematite-based photoanodes was reported by Jeon *et al.* in 2017, reaching a stable photocurrent density of ~6 mA cm^{-2} at 1.23 V vs. RHE over 100 h under AM 1.5G irradiation (100 mW cm^{-2}) with Faradaic efficiency of ~95%.[250] Notably, this impressive performance was achieved by optimization of combined modification methods that are all well-known and previously demonstrated. An earlier demonstrated photoanode with CoPi/Ag/α-Fe$_2$O$_3$/Fe foil configuration exhibited a stable photocurrent density of 4.68 mA

cm^{-2} at 1.23 V vs. RHE in 1 M NaOH under AM 1.5G (100 mW cm^{-2}) illumination.[251] Similarly, a CoPi/α-Fe$_2$O$_3$:Pt/FTO photoanode prepared via a solution-based method showed a photocurrent density of 4.32 mA cm^{-2} at 1.23 V vs. RHE in 1 M NaOH under AM 1.5G simulated sunlight.[252] However, their onset potentials were still around 0.7 V vs. RHE, which were very positive.

Despite the low photoactivity, hematite photoanodes have been upscaled to larger areas for investigation. Mendes and co-workers proposed a novel PEC cell design and tested a 10 × 10 cm^2 undoped-hematite photoanode deposited by ultrasonic spray pyrolysis on transparent conductive oxide glass, showing a photocurrent density of 0.40 mA cm^{-2} at 1.45 V vs. RHE in 1 M KOH electrolyte under 1 sun solar irradiation.[253] Hankin *et al.* fabricated 10 × 10 cm^2 Sn-doped hematite photoanodes on Ti foil substrates by spray pyrolysis to carry out both experimental and modelling study about reactor scale-up issues.[254] It was discovered that perforated photoelectrodes decreased ionic current path lengths and thus decreased macroscopic inhomogeneities in current density distributions compared to planar ones. In addition, by comparing a single 50 cm^2 hematite photoanode with eight 3.2 cm^2 photoanodes connected in parallel, Vilanova *et al.* concluded that the multi-photoelectrode configuration produced a slightly higher photocurrent density as well as a higher photovoltage.[255] Encouragingly, through investigation on two different types of hematite photoanodes with different thickness, morphology and dopants, Segev *et al.* found that the water photo-oxidation current density scaled linearly with the solar flux concentration ranging from below 1 to above 25 suns, whereas the photovoltage scaled logarithmically with the flux concentration at a significantly faster rate than that in concentrated photovoltaics (Figure 28).[256] This discovery indicated that commercially viable high solar flux concentration could further increase the efficiency of hematite photoanodes used for water splitting tandem cells.
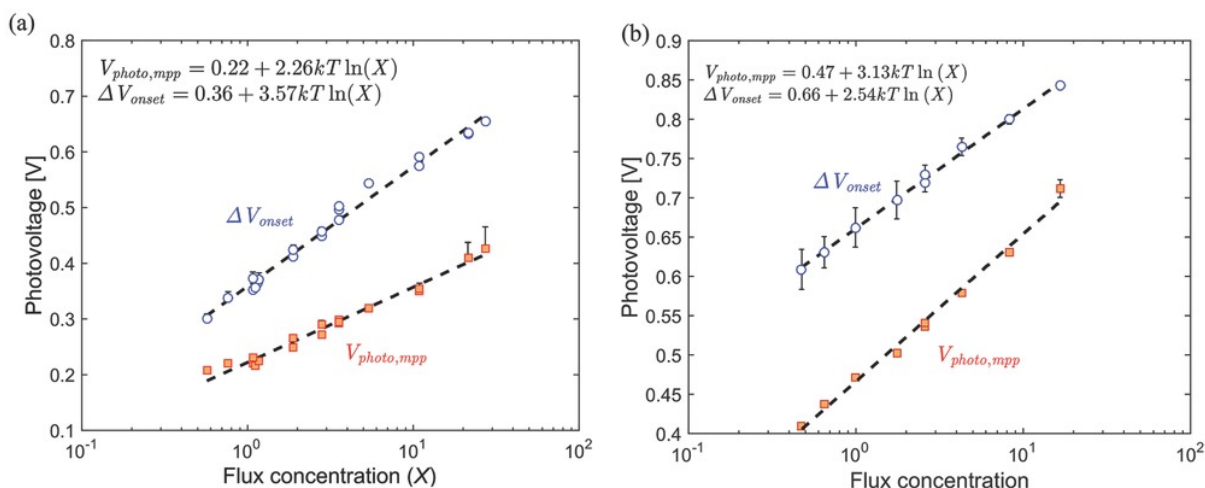
(a)
$V_{photo,mpp} = 0.22 + 2.26kT\ln(X)$
$\Delta V_{onset} = 0.36 + 3.57kT\ln(X)$

(b)
$V_{photo,mpp} = 0.47 + 3.13kT\ln(X)$
$\Delta V_{onset} = 0.66 + 2.54kT\ln(X)$

Figure 28. The photovoltage at the maximum power point (orange squares) and the photo-induced shift in the onset potential (blue circles) as a function of the flux concentration for (a) compact Ti-doped hematite with a film thickness of 50 nm and (b) mesoporous Si-doped hematite with a film thickness of 500 nm. Reproduced with permission from Ref. [256], copyright (2015) John Wiley and Sons.

Amongst various oxide semiconductors used for photoanodes, $BiVO_4$ is one of the most promising candidates that demonstrate both high photocurrent density and low onset potential of 0.1-0.2 V vs. RHE. In 2015, Pihosh *et al.* demonstrated a $WO_3/BiVO_4$+CoPi core-shell nanostructured photoanode fabricated by Glancing Angle Deposition.[257] It achieved water oxidation photocurrent density of 6.72 mA cm^{-2} at 1.23 V vs. RHE under 1 sun illumination, which corresponded to ~90% of the theoretical value for $BiVO_4$. However, the electrode size was only 0.226 cm^2 and the long-term photostability was not reported. A 2.25 cm^2 photoanode of WO_3/(W,Mo):$BiVO_4$+FeOOH/NiOOH achieved a photocurrent density of 5.35 ± 0.15 mA cm^{-2} at 1.23 V vs. RHE in 0.5 M K_2SO_4 in phosphate buffer (pH 7) under 1 sun illumination.[258] This helix nanostructured photoanode was fabricated by e-beam evaporation and oblique angle depiction. Stability test was conducted over 84 h with 8.73% photocurrent decay.

As the water oxidation performance of $BiVO_4$ photoanodes continues to improve, emerging research focuses on the enhancement of their long-term stability. To supress the anodic

photocorrosion with the loss of V^{5+} ions from the $BiVO_4$ lattice by photooxidation-coupled dissolution, V^{5+}-saturated electrolyte was used, maintaining stable water oxidation photocurrent of the $BiVO_4$/FeOOH/NiOOH photoanode for up to 450 h.[259] A more stable Mo-doped $BiVO_4$ photoanodes exhibiting a constant photoactivity over 1100 h was developed by Kuang *et al.* upon high-temperature treatment and in situ catalyst regeneration.[260] As shown in Figure 29, the nickel contact layer between Sn and Mo-doped $BiVO_4$ was dissolved upon electrochemical oxidation. Upon simulated solar irradiation, the dissolved Ni^{2+} ions were photoelectrochemically deposited on the surface of Mo:$BiVO_4$. This Ni oxygen evolution catalyst (OEC) was subsequently converted into a more active NiFe-OEC via the incorporation of Fe species from electrolyte. Thus, the continuous dissolution and in situ regeneration of the NiFe catalyst enable a stable photocurrent at pH 9 during the 1100 h solar-driven water oxidation test.

However, these promising approaches have not been applied to improve the photoactivity or photostability of up-scaled $BiVO_4$ photoanodes. For example, a 5 cm × 5 cm WO_3/Mo:$BiVO_4$/CoPi photoanode prepared via metal-organic decomposition showed 21% photocurrent loss after only 1 h of operation under AM 1.5G illumination in 0.5 M Na_2SO_4 solution (pH 6).[261] A deleterious areal effect was also proposed, which decreased the photocurrent density as the active area of photoanode was enlarged.
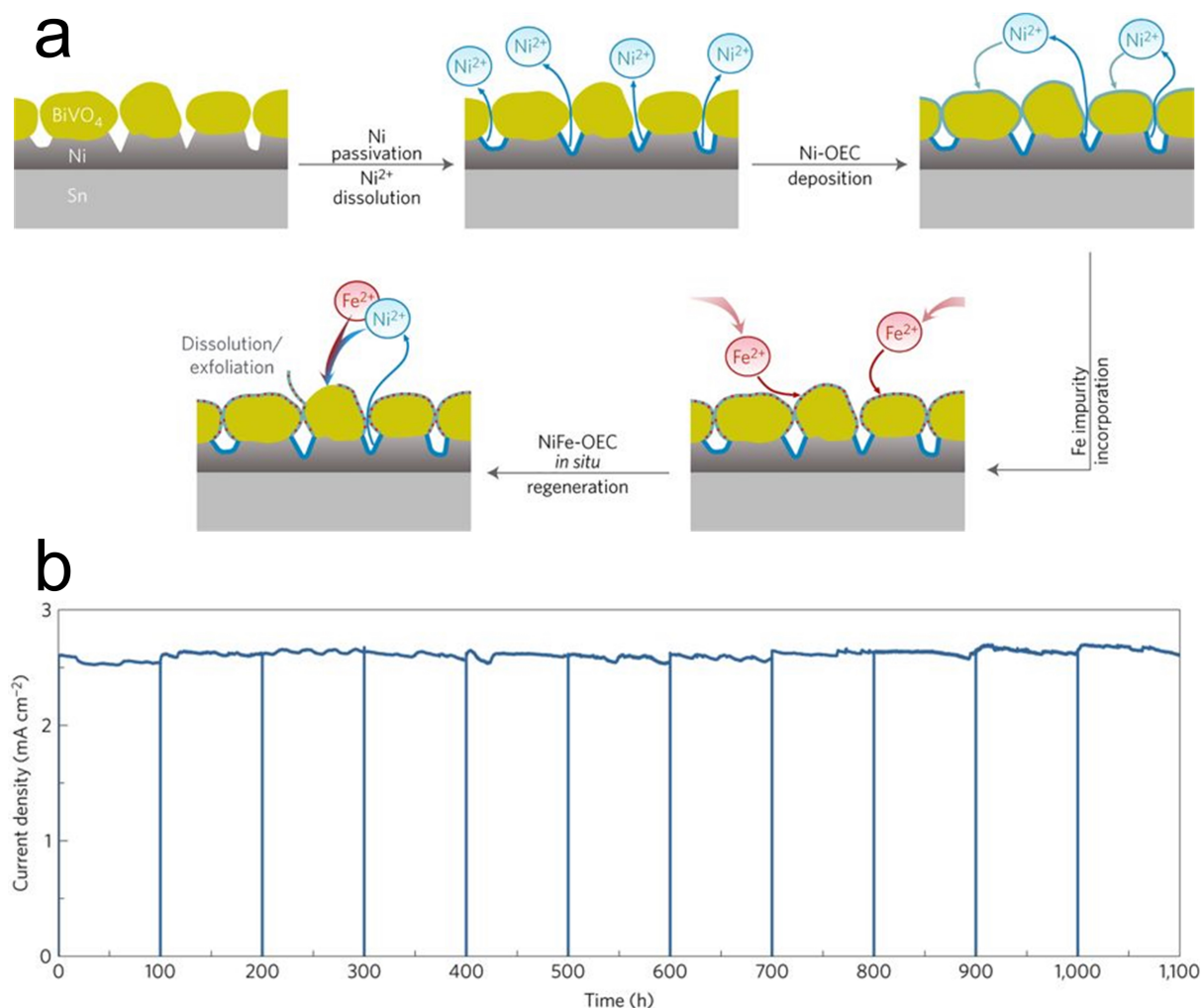
Figure 29. (a) Schematic illustration of the self-generated NiFe OEC and *in situ* regeneration. (b) Long-term water photooxidation stability of the NiFe-OEC /Mo:BiVO$_4$/Ni/Sn photoanode over 1100 h under AM 1.5G irradiation (100 mW cm^{-2}) at 0.6 V vs. RHE in 1 M borate buffer (pH 9). Reproduced with permission from Ref. [260], copyright (2016) Nature Publishing Group.

The choice of suitable p-type semiconductors for photocathodes is more arduous than that for photoanodes as p-type semiconductors are highly unstable during the reduction process in electrolytes. Cu$_2$O is a promising p-type oxide as photocathode for PEC hydrogen evolution with a direct bandgap of 2 eV, which corresponds to a theoretical maximum photocurrent of 14.7 mA cm^{-2} and STH efficiency of 18% under AM 1.5G illumination.[262] Grätzel and co-workers reported a Cu$_2$O-nanowires/AZO/TiO$_2$/RuO$_x$ photocathode prepared by sputtering, anodization, post-annealing and atomic layer deposition.[263] A higher photocurrent density of

~8 mA cm^{-2} at 0 V vs. RHE was achieved compared to a planar Cu$_2$O photocathode. Later, the same group further improved its photoactivity by replacing AZO with a Ga$_2$O$_3$ layer to form a Cu$_2$O-nanowires/Ga$_2$O$_3$/TiO$_2$/RuO$_x$ photocathode.[264] The Cu$_2$O/Ga$_2$O$_3$-buried p-n junction led to efficient light harvesting at $\lambda < 600$ nm and an external quantum yield of almost 80% for H$_2$ production. The photocathode also exhibited an onset potential of +1 V vs. RHE and a photocurrent density of ~10 mA cm^{-2} at 0 V vs. RHE. The planar Cu$_2$O photocathode with higher fill factor was chosen and combined with a Mo:BiVO$_4$ photoanode to construct an unassisted overall solar splitting tandem device (Figure 30). In this configuration, the light first passed through the BiVO$_4$ photoanode before reaching the Cu$_2$O photocathode. After optimizing the transparency of the Mo:BiVO$_4$ photoanode, a STH efficiency of ~3% was obtained with less than 10% loss under continuous illumination for 12 h.

P-type semiconductors widely used in photovoltaics are also candidates for fabrication of photocathodes, such as p-Si and copper-based chalcogenides Cu(In,Ga)Se$_2$ (CIGS) and Cu$_2$ZnSnS$_4$ (CZTS). To enhance the PEC performance, copper-based chalcogenide photocathodes were generally covered with n-type semiconductor layers and noble metal co-catalyst to provide protection and create cascade electron transfer.[265-266] This configuration enabled high cathodic photocurrents with improved photostability.[267-268] Unassisted water splitting with a STH efficiency of 0.28% was also reported by Jiang *et al.* using a Pt/In$_2$S$_3$/CdS/CZTS photocathode and a BiVO$_4$ photoanode.[269] Silicon as the most successful material used in the PV industry has also been investigated as photocathodes.[270-271] Planar n$^+$p-Si photocathode was found to show higher photovoltage than planar p-Si photocathode and higher photocurrent than microwire array n$^+$p-Si photocathode.[272-273] Interfacial engineering techniques such as adding electron-selective TaO$_x$ passivation layer further boosted the performance of Si photocathode reaching a photocurrent density of 37.1 mA cm^{-2}

at 0 V vs. RHE.[274] Unbiased photoelectrochemical water splitting was reported by Jang *et al.*
combining a hematite photoanode with turn-on voltage of 0.45 V vs. RHE and an amorphous
Si photocathode (Figure 31).[275] Although the achieved 0.91% of STH efficiency was modest,
this was the first demonstration with a meaningful efficiency using photoelectrodes that were
made of the most earth-abundant elements.
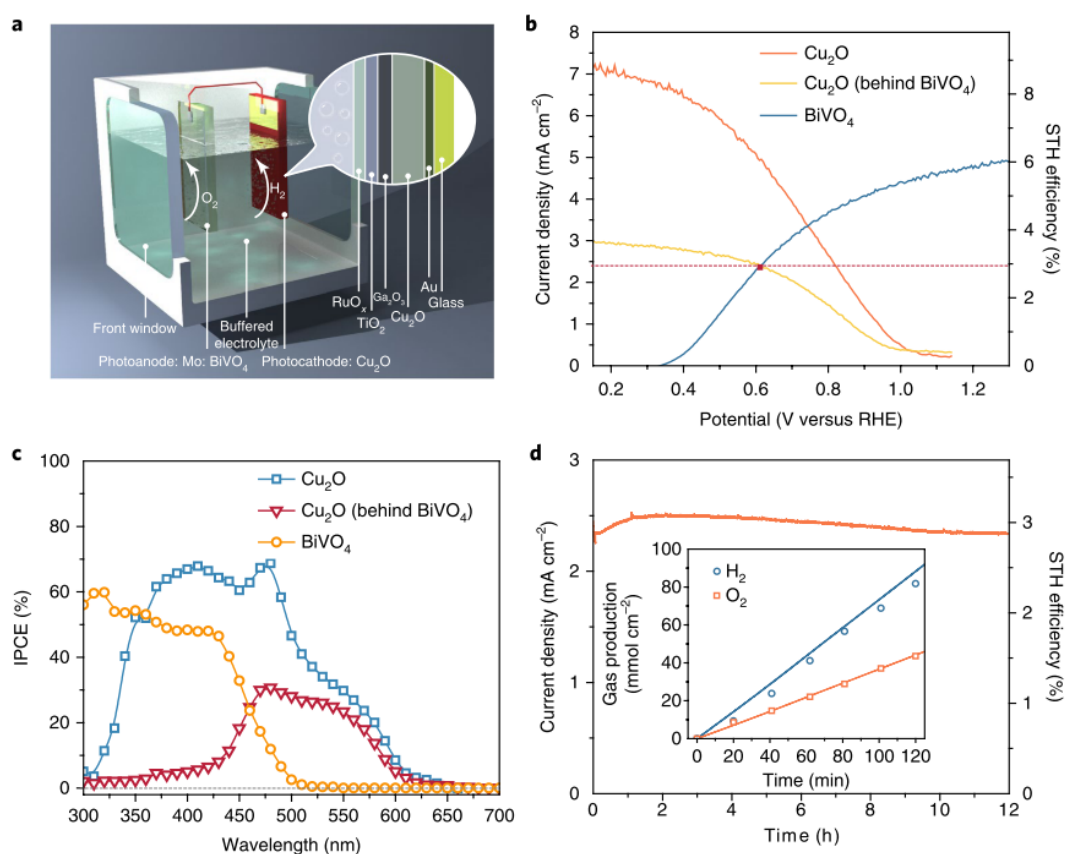
Figure 30. Unassisted all-oxide solar water splitting. (a) Schematic of the all-oxide tandem
solar water splitting device, consisting of Cu_2O as the photocathode and Mo-doped $BiVO_4$ as
the photoanode without bias. (b) *J–E* response under simulated AM 1.5 G chopped
illumination for the Cu_2O photocathode, $BiVO_4$ photoanode and Cu_2O photocathode behind
the $BiVO_4$ photoanode in 0.2 M potassium borate (pH 9.0). (c) Wavelength-dependent IPCE
spectra. (d) Unbiased stability test in 0.2 M potassium borate. Reproduced with permission
from Ref. [264], copyright (2018) Nature Publishing Group.

Figure 31. Overall unassisted water splitting. (a) Schematic of overall unassisted water splitting with hematite photoanode and amorphous Si photocathode in tandem. (b) Net photocurrent during 10 h operation using NiFeO$_x$-modified hematite and TiO$_2$/Pt-loaded amorphous silicon photocathode in 0.5 M phosphate solution (pH 11.8). The inset shows the photocurrent-potential curves of hematit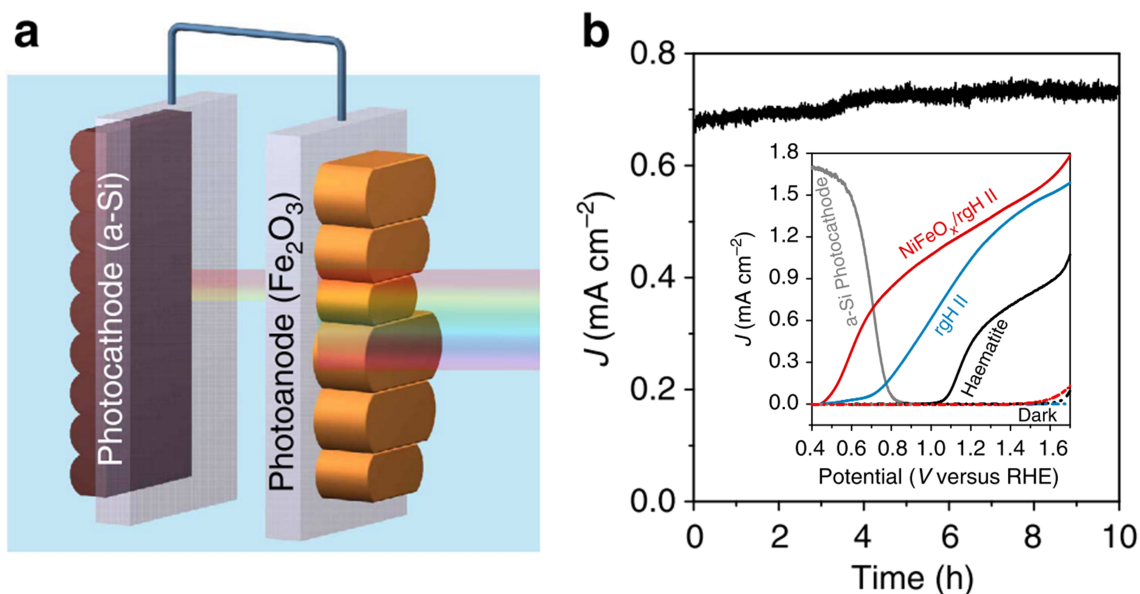e photoanode and Si photocathode placed behind the photoanode. Reproduced with permission from Ref. [275], copyright (2015) Nature Publishing Group.

5.3 Non-integrated/modular devices

A modular PV-electrolysis water splitting system is the most straightforward strategy towards large-scale hydrogen production by simply combining commercial PV cells with electrolysers. In theory, a modular system could reach STH efficiencies of ~57% using a triple-junction cell and ~62% using a four-junction or five-junction cell.[276-277] However, they have been previously considered as too expensive to be economically viable, which was mainly ascribed to the use of noble-metal catalysts and high-cost and/or low-efficiency PV cells. Encouragingly, within the last decade, PV efficiency has been dramatically improved with decreasing cost. Highly active and robust earth-abundant water splitting catalysts have also been developed, which showed comparable catalytic performance with noble metal-based catalysts. Moreover, recently reported system design and integration strategies of

70

modular water splitting devices have enabled stable production of hydrogen with high overall STH efficiency.

5.3.1 Membrane-based modular devices

Currently, there are two common membrane/diaphragm-based electrolyser technologies, *i.e.* polymer electrolyte membrane (PEM) electrolysers and alkaline electrolysers (Figure 32).[278] The membrane and diaphragm of both electrolyser types permit the transport of ions (protons/hydroxide ions) between the anode and cathode. In addition, they were also used to separate the gases H_2 and O_2 products to prevent them from forming an explosive mixture.
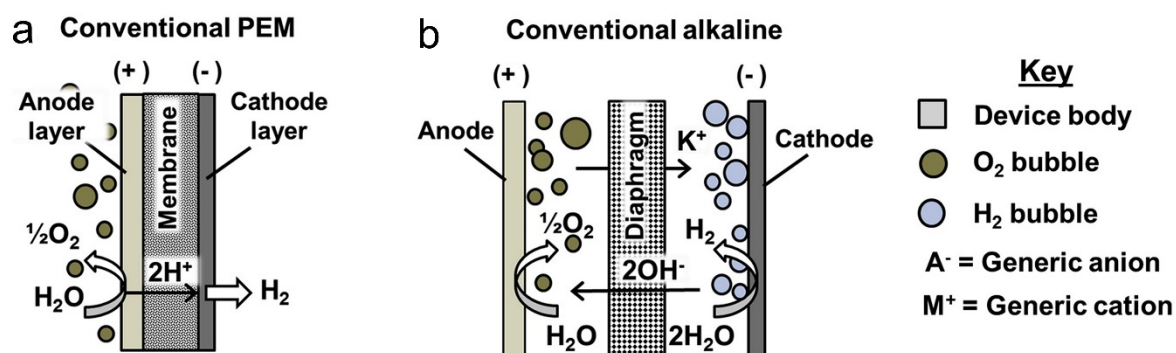
Figure 32. Side-view schematics of low-temperature electrolysers. Conventional (a) PEM and (b) alkaline electrolyser cells. Reproduced with permission from Ref. [278], copyright (2017) Elsevier Inc.

To date the highest STH efficiency of ~30% was delivered using a InGaP/GaAs/GaInNAsSb triple-junction solar cell (0.316 cm^2 area) and two PEM electrolysers under 42 suns (Figure 33).[277] However, nearly 10% photocurrent loss was observed after 48 h continuous operation, which might be caused by a decrease in performance of the custom-built electrolysers. A lower STH efficiency of 24.4% was reported by Nakamura *et al.* in an outdoor field test by combining 5 polymer-electrolyte electrochemical cells in series and 3 concentrator PV modules (light-receiving area of 57 mm^2) with InGaP/GaAs/Ge triple-junction cells (2.5 mm^2) in series.[279] Long-term stability test was not shown in this work.

In addition to increasing the system efficiency, it is crucial to improve the stability as most reports show the operation duration of less than 24 hours.[8] Spiccia and co-workers demonstrated a both efficient and robust modular setup that maintained a STH efficiency of 22.4% over 72 h during 12 h on-off cycling under 100 suns.[280] In this setup, a GaInP/GaAs/Ge multi-junction solar cell was connected to 10 cm^2 Ni foam electrodes immersed in 1 M NaOH. After replacing the electrodes with 15 cm^2 Ni foams and the electrolyte with a mixture of 0.6 M borate buffer and 0.23 M Na_2SO_4, the same high STH efficiency of 22.4% was still preserved over 24 h photoelectrochemical water splitting test. Series-connected crystalline Si solar cells as a dominating technology are attractive for application in a modular system to provide photovoltages of above 1.23 V that is the thermodynamic potential for water splitting reaction. Through modelling of connected Si PV and electrolyser system, Winkler *et al.* predicted that the maximum STH efficiency is ~27% for two series-connected cells with the absorber's band gaps of 1.04-1.12 eV.[281]

Several Si PV-electrolyser setups have been presented with STH efficiencies ranging from 9.5% to 14.2% and stable operation over more than 100 hours under reported conditions.[282-284] A larger-scale device was fabricated comprising a 64 cm^2 a-Si:H/a-Si:H/μc-Si:H triple junction PV cell and two Ti sheet electrodes loaded with Pt and IrO_x catalysts, respectively (Figure 34).[285] The whole PV was composed of 64 individual solar cells with an area of 1×1 cm^2 each, which was manufactured by PECVD, magnetron sputtering, thermal evaporation and laser scribing. This device yielded a STH efficiency of 4.8% in 1 M H_2SO_4 under a simulated AM1.5G spectrum (1000 W m^{-2}). Very recently, Shen and co-workers proposed a Si PV-PEC tandem configuration composed of 2 series-connected Si PV cells, an n^+np^+-Si photocathode and p^+pn^+-Si photoanode.[286] Both the photoanode and photocathode were protected with a Ni layer and loaded with a bifunctional Ni-Mo catalyst. A STH efficiency of 9.8% was maintained over 100 h in 1 M KOH under parallel AM 1.5G 1 sun illumination. In

addition, metal halide perovskites with the potential to deliver more efficient and cheaper PV than silicon-based technology have attracted extensive research attention.[287]

The performance of perovskite solar cells has been rapidly boosted up to 23.7% over the past few years.[288] In 2014, Luo *et al.* combined two solution-processed perovskite solar cells connected in series and bifunctional NiFe catalyst-loaded Ni foams as electrodes for water splitting.[289] The combined device yielded a STH efficiency of 12.3%. However, its lifetime was limited by the intrinsic instability of the perovskite. Since then the photo-, moisture and thermal stability of perovskite solar cells has been gradually improved,[290-292] perovskite-based solar-driven water splitting devices with better stability have been demonstrated.[293]
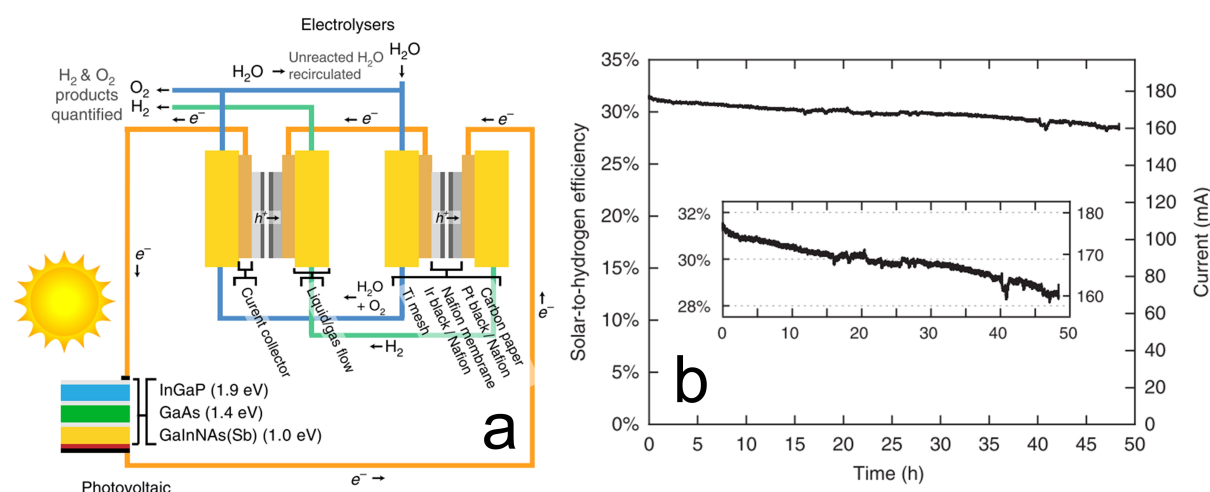

Figure 33. (a) Schematic representation of the PV-electrolysis device. (b) The photocurrent and corresponding STH efficiency of the PV-electrolysis system measured over 48 h of continuous operation. The inset highlights a smaller *y* axis range for improved clarity. Reproduced with permission from Ref. [277], copyright (2016) Nature Publishing Group.
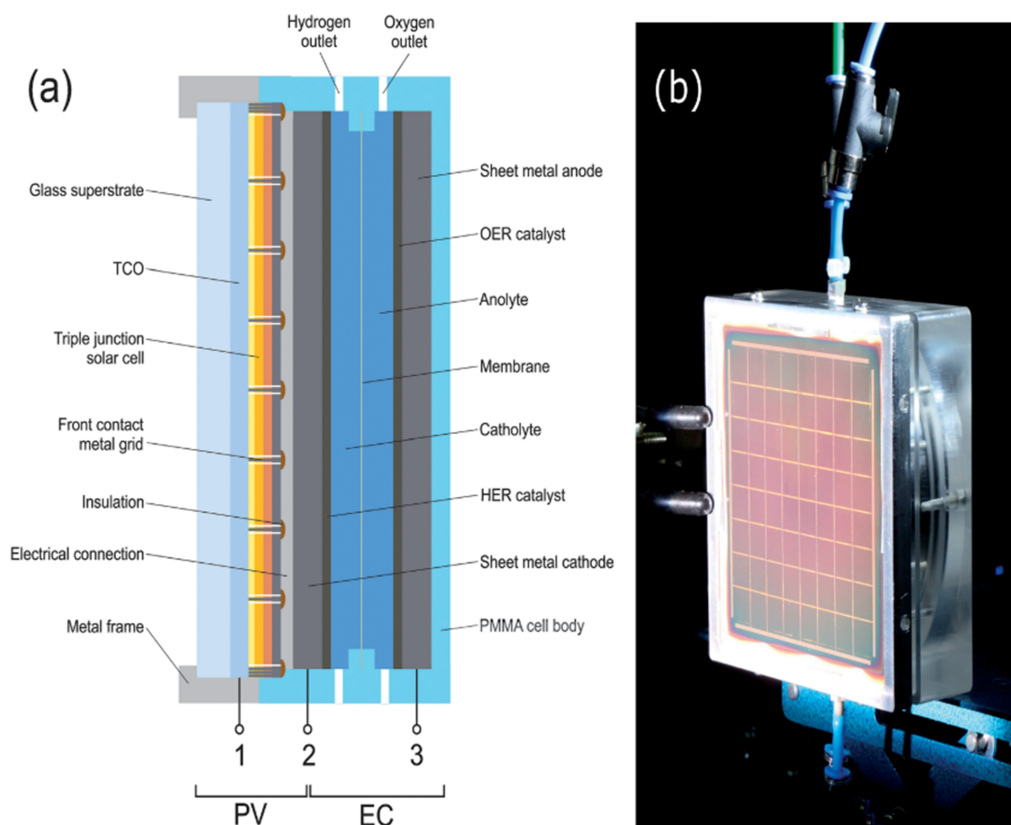
Figure 34. (a) Schematic cross-section of the PV-electrolysis device. The electronic properties of the PV, the electrochemical cell (EC), and the combined PV-EC module are accessible via the three contacts (1–3). (b) Photograph of the integrated PV-EC module under illumination from the front side. Reproduced with permission from Ref. [285], copyright (2017) The Royal Society of Chemistry.

In addition to tests under laboratory conditions, a comprehensive understanding of PV-electrolysis field performance under realistic operating conditions will facilitate holistic system design and scalability. In 2007, a STH efficiency of 18% was obtained based on an outdoor test of a prototype system with an area of 96 cm^2, which was comprised of III-V solar cells and a PEM electrolyser.[294] Recently, a two-month outdoor measurement was performed combining eight individual hydrogen concentrator cells (Figure 35).[295] Each cell consisted of a III-V double-junction PV and an PEM electrolyser. Although the STH efficiency of the system fluctuated under the changing environmental conditions, a maximum efficiency of 19.8% and a current density of 0.8 A cm^{-2} were reached. During this field test,

around 1 m^3 of hydrogen was produced and no overheating issue was encountered under natural convection.
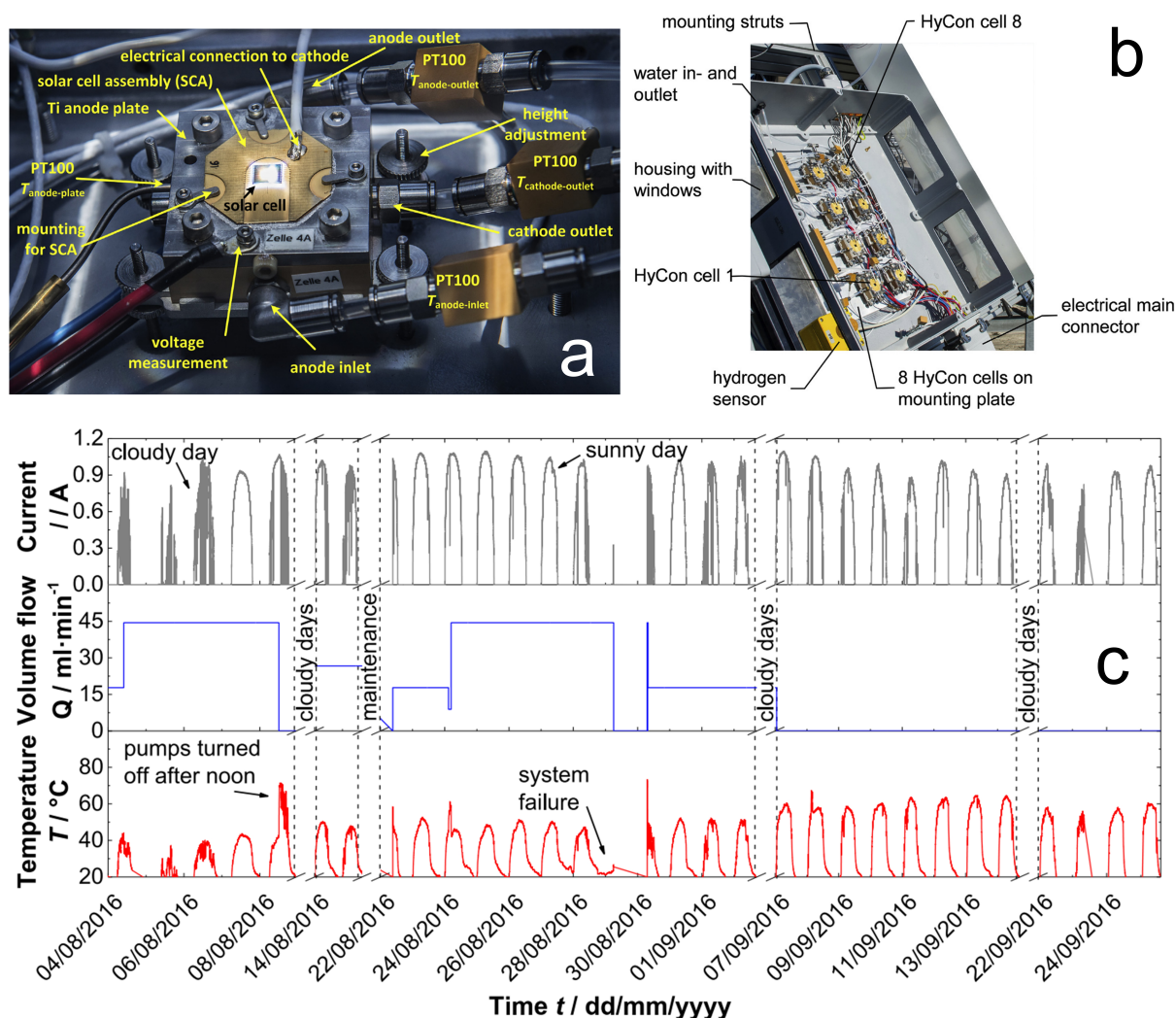
Figure 35. (a) Photograph of a mounted hydrogen concentrator cell. (b) Hydrogen concentrator demonstrator module mounted on a tracker on top of a Fraunhofer ISE building. The housing cover with integrated lenses is disassembled to show the interior parts. (c) Arithmetic mean of the current of all 8 cells (top), the deionized water volume flow (middle) and the temperature of the anode plate of hydrogen concentrator cell 1 (bottom) over the measurement period of 60 days. Reproduced with permission from Ref. [295], copyright (2017) Elsevier Inc.

5.3.2 Membraneless electrolyser-based system

Another advantage of a modular system is that each component, *i.e.* the solar cell, the HER and OER catalysts, the electrolyte and the membrane, can be individually designed and

optimized. Recent works also proposed some new configurations of membraneless electrolysers, which represented a promising approach to decrease capital costs required for water electrolysis (Figure 36).[278] In type I devices (Figure 36a), aqueous electrolyte carries hydrogen and oxygen gases flowing parallel to the electrode surfaces, then in the downstream region the electrolyte was separated into two effluent channels with mainly H_2- and O_2-rich electrolyte, respectively. This type of device has been demonstrated by Psaltis and co-workers, showing continuous and robust operation with various catalysts and electrolytes across the pH scale.[296] In type II configuration (Figure 36b), the metallic mesh electrodes allow the electrolyte to flow through the electrode gap and diverge, carrying the H_2 and O_2 gases into separate effluent channels. A H_2 purity of 99.83% and current density of 3.5 A cm^{-2} were achieved.[297] A modified design with the device body as a single, monolithic component was later reported by O'Neil et al. using angled mesh flow-through electrodes.[298] Another new concept was proposed using $NiOOH/Ni(OH)_2$ redox couple as auxiliary electrodes for water electrolysis. H_2 and O_2 could either be sequentially generated in two steps,[299] or continuously co-generated in separate cells.[300] Upon coupling with four Si PV cells connected in series, the resulting PV-electrolysis system delivered a STH efficiency of 7.5%, averaged over 1 h operation.[300]
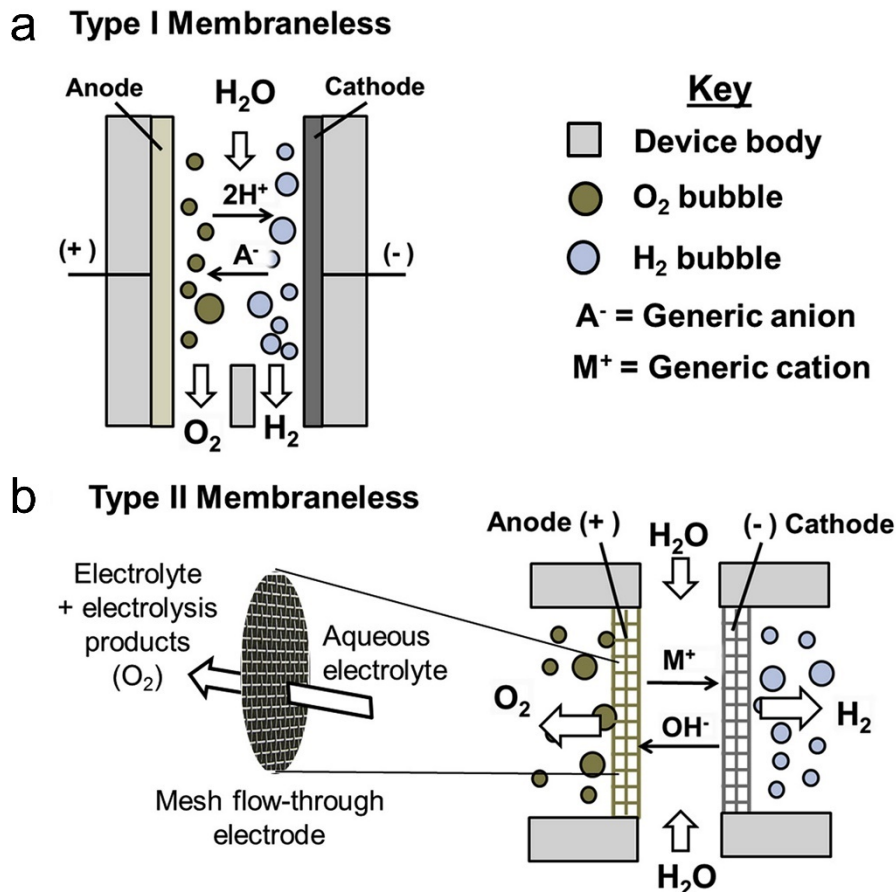
Figure 36. Side-view schematics of low-temperature electrolysers. Emerging membraneless electrolysers based on (a) flow-by electrodes and (b) flow-through electrodes. The inset in (b) illustrates a 3D view of a mesh flow-through electrode evolving O_2 while electrolyte passing through holes in the mesh. Reproduced with permission from Ref. [278], copyright (2017) Elsevier Inc.

5.4 Challenges in scale-up

5.4.1 Industrially viable fabrication techniques

Development of industrially viable techniques to fabricate electrodes, photoelectrodes and PV is crucial for the large-scale hydrogen production. Encouragingly, fabrication strategies for PV grade materials have been well established as PV panels are commercially available with the sizes of above 1 m^2. However, III-V light absorbers, which contributed to the high efficiency PEC and PV-electrolysis systems, were usually produced by metal organic vapor phase epitaxy (MOVPE) and other highly complex methods under oxygen-free atmosphere.[301]
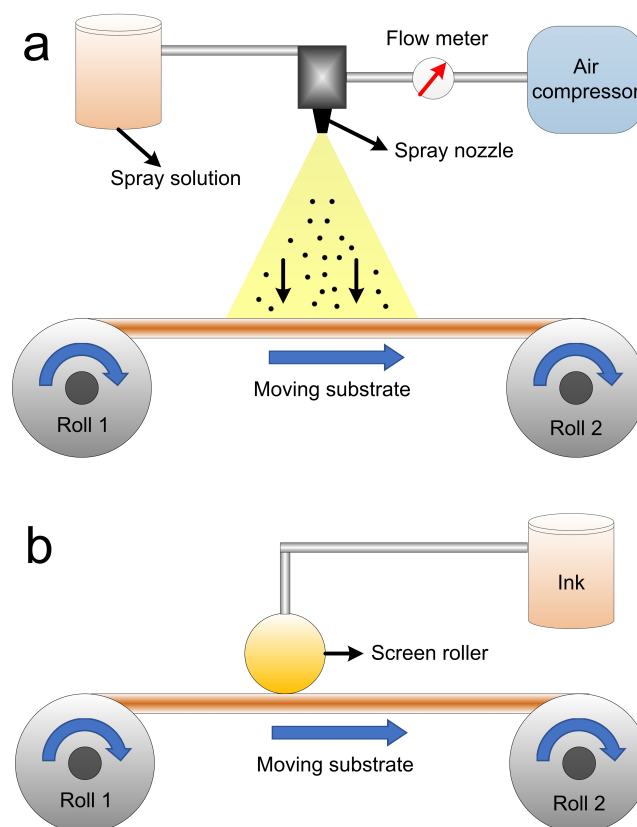
Figure 37. Schematics of roll-to-roll fabrication techniques. (a) Spray pyrolysis roll-to-roll coating technique. (b) Rotary screen printing technique.

A roll-to-roll technique is promising to achieve industrial-scale fabrication of electrodes/photoelectrodes or deposition of co-catalysts on photoelectrodes. Amongst various deposition methods, spray pyrolysis (Figure 37a) and screen printing (Figure 37b) are compatible with this technique. Both traditional wet spray pyrolysis and screen printing techniques have been reported for fabrication of electrodes and photoelectrodes.[248, 302-306] Flame spray pyrolysis as an aerosol deposition method is also highly scalable for facile and fast fabrication of various nanostructured (photo)electrodes.[307-310] A production rate of a few kilograms per hour is achievable using lab-scale burners with tunable specific surface area and catalytic activity of the produced nanomaterials.[311-312] Notably, although the electrocatalysts produced by these industrially viable fabrication techniques demonstrated excellent catalytic activities,[310, 313] the photoelectrodes fabricated using them still showed

poorer photoactivities than those state-of-the-art photoelectrodes using conventional lab-scale fabrication techniques.[254, 314]

5.4.2 Design of scaled-up cells

Holistic design guidelines are crucial for the development of commercially viable solar hydrogen production devices and systems. Dumortier *et al.* reported a simulation platform to assess 16 different design types of PV-electrolyser systems using four indicators - operation time-averaged STH efficiency, hydrogen cost, device manufacture and operation energy demand per mass unit of hydrogen produced, and operational time (Figure 38).[315] They discovered that the device types utilizing high irradiation concentration, costly photoabsorbers and electrocatalysts demonstrated maximum efficiency, minimum cost and energy demand of manufacture and operation. These results were valid for a variable device size as cost and energy requirement in their study were assessed per unit area of the device.
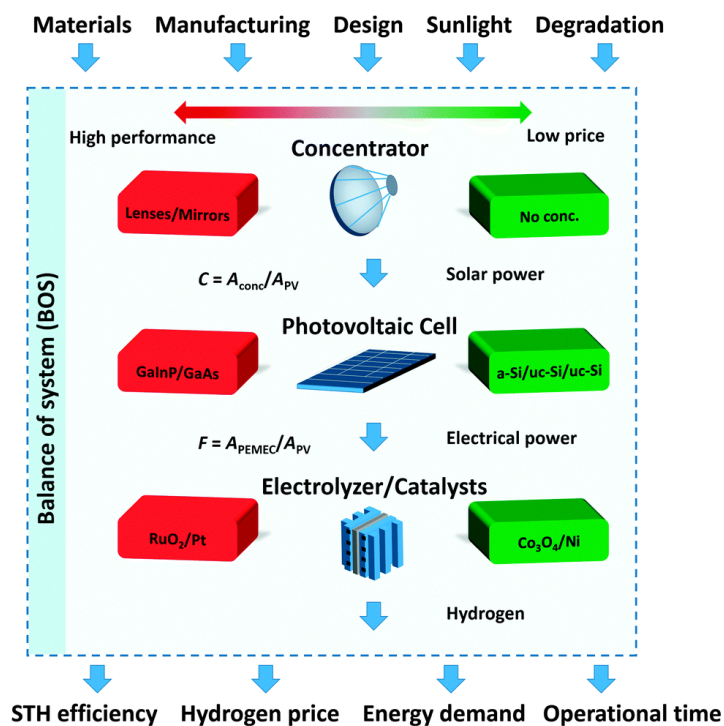

Figure 38. Schematic of device component choices with various inputs and outputs. The choice between advantageous performance and cost of the concentrator, PV cell and PEM electrolyser results in 8 possible device solutions, which are extended by considering current

concentration for each case, resulting in 16 device types investigated. Reproduced with permission from Ref. [315], copyright (2015) The Royal Society of Chemistry.

Different from the lab-scale photoelectrodes, substrate ohmic losses have pronounced influence on the photoelectrochemical performance of scaled-up ones. Holmes-Gentle *et al.* reported that large size led to a significant potential drop for the same photoelectrode (Figure 39a, b).[316] All model photoelectrodes in their study with the size of 50 cm × 50 cm showed ~80% photocurrent density losses (Figure 39c) compared to the lab-scale ones (0.1 cm^2), which remains an obstacle to scaling up photoelectrodes on low conductivity substrates such as transparent conductive oxides. In addition, optical losses will be caused by scattering and reflecting incidence solar photons by bubbly mixture.[317] These losses may be significant for PEC systems with large illuminated areas. Effective mitigation strategies are required to address this issue, such as removing bubbles faster by increasing convection, reflecting scattered light back onto photoabsorbers, hydrodynamically transporting the bubbles behind the photoelectrodes out of the path of light *et al.*[317] However, there strategies will inevitably increase the energy input or system complexity.

Temperature, as a key parameter to the PEC system performance during field tests, was investigated via modelling by Lewis and co-workers.[318] They concluded that the annually averaged efficiency of a PEC device with a limiting overpotential can be improved if it is dynamically adapted to higher operating temperatures as the solar irradiation increases, which will occur naturally throughout a day. A given example was that, compared to a cooled system under constant operation at 300 K, the conversion efficiency could be increased by 1% in July by dynamically adapting to the temperature during the day. On the other hand, this work was indicative of the complex interaction between system performance and the variations of environmental factors during outdoor operation. For real-world applications, a

comprehensive modelling approach must be implemented considering illumination intensity, PEC behaviour, local weather, insolation conditions and heat balances.[319]
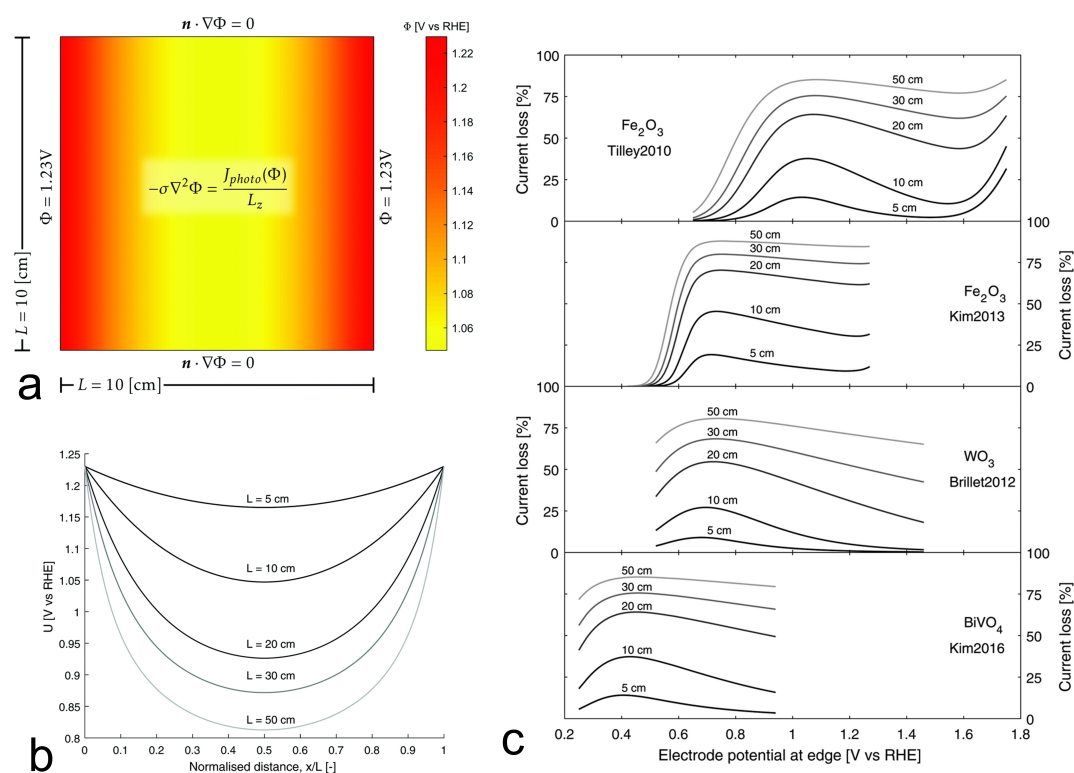
Figure 39. (a) Color map of substrate potential overlaid with model equations and boundary conditions, for U_0 = 1.23 V *vs.* RHE and L = 10 cm. (b) Potential distribution at $y = L/2$ for a boundary condition U_0 = 1.23 V *vs.* RHE for various electrode sizes. (c) Current losses at various electrode widths for model photoelectrode datasets. Reproduced with permission from Ref. [316], copyright (2018) The Royal Society of Chemistry.

5.5 Efforts to address challenges in scale-up

Recently, there are a few demonstrations tentatively addressing the above-mentioned challenges in scale-up of PEC water splitting systems. Vilanova *et al.* designed a 50 cm^2 tandem photoanode-PV cell using various systematic optimization strategies to improve its overall performance.[320] The PEC cell presented highly stable water splitting activity upon continuous operation for 1008 h in 1.0 M KOH under 1000 W m^{-2}, which was comprised of a 50 cm^2 hematite photoanode prepared by spray pyrolysis, a platinized-Ti mesh as cathode, an

ion-exchange membrane and two 50 cm^2 silicon heterojunction solar cells connected in series (Figure 40). The hematite/FTO glass photoanode also functioned as one of the windows of the cell. Both computational fluid dynamics and observation of dyed electrolyte flow were applied to reduce bubbles-induced optical loss from ~82% for non-optimized cell to ~17% for the optimized one (Figure 40b). Furthermore, temperature contours of the electrolyte under concentrated sunlight (17 kW m^{-2}) inside the cell were simulated. Constant electrolyte feeding (0.5 L min^{-1}) was maintained at a moderate temperature of 45 °C without a significant gradient in the reactor.

Substrate ohmic loss and charge transport issue of large-scale photoelectrodes were addressed by creating metal grid structures as demonstrated in the PECDEMO project.[321] During large-area fabrication of a BiVO$_4$ photoanode (7.1 × 7.1 cm^2), molybdenum metal grids were deposited on FTO glass to improve the charge collection efficiency (Figure 41a). An absolute photocurrent of 55 mA was achieved at 1.23 vs. RHE under 1 sun in 0.1 M phosphate + 0.5 M Na$_2$SO$_3$ electrolyte (Figure 41b). However, its photocurrent density was still around one third of that for small-area BiVO$_4$. Similarly, a 4-striped type Cu$_2$O-AZO/TiO$_2$-RuO$_x$ photocathode (50.4 cm^2) with Au or Ag metal grid lines were produced by electrodeposition, atomic layer deposition and photodeposition (Figure 41c). The Ag grid was better than the Au grid for improving the charge transport due to its better conductivity and adhesion to the FTO substrate. Consequently, the photocurrent density of large-area Cu$_2$O photocathode with Ag grid lines reached 2 mA cm^{-2} at 0 V vs. RHE in pH 5 electrolyte under 0.6 sun illumination (Figure 41d).
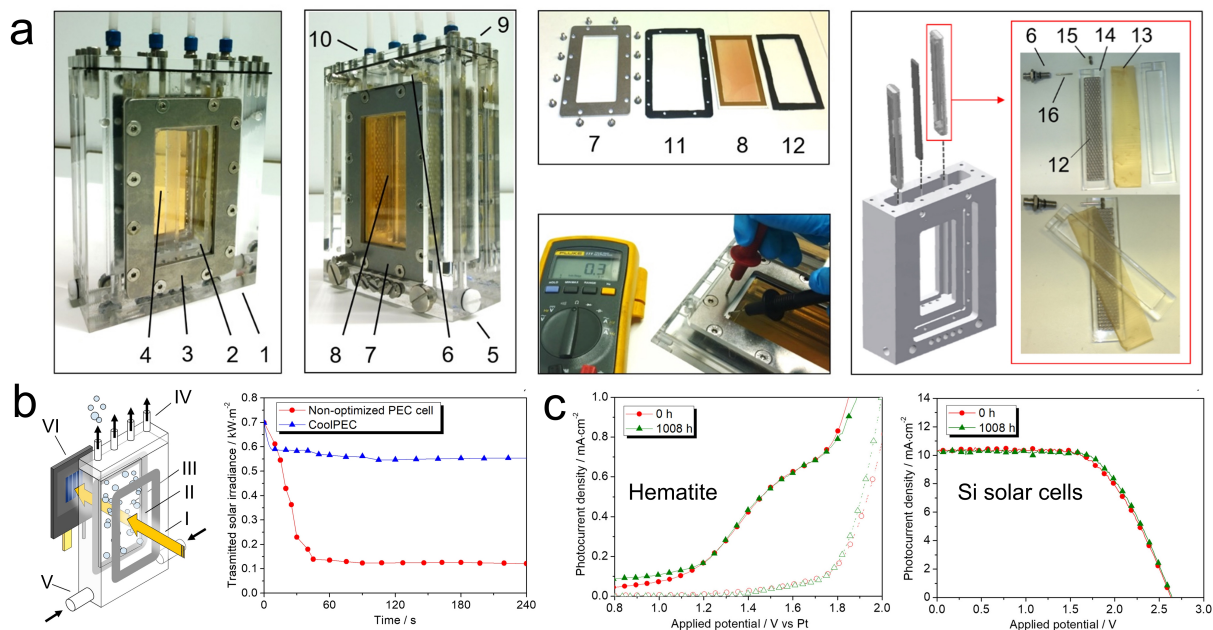
Figure 40. (a) CoolPEC cell. 1 – acrylic embodiment; 2 – front window (synthetic quartz); 3 – front stainless steel frame; 4 – internal acrylic plate dividing the working electrode compartment; 5 – main electrolyte inlet; 6 – external screw (current collector for the counter electrode); 7 – back stainless steel frame; 8 – back window (photoelectrode); 9 – acrylic cap; 10 – electrolyte outlet; 11 - internal gasket; 12 - external gasket; 13 – Platinized-Ti mesh; 14 – ion exchange membrane; 15 – acrylic holders; 16 – metal connectors between the Pt-Ti mesh and the external screw. (b) Assessment of light trapping due to bubbles accumulation inside the PEC cell. I – simulated sunlight (1000 W m^{-2}); II – front window (synthetic quartz); III – back window (FTO glass); IV – electrolyte outlet; V – electrolyte inlet; VI – Si calibrator used to monitor the solar irradiance reaching the outer surface of the back window; solar irradiance reaching the external surface of the back window monitored over 4 min with the PEC cell operating at 5.4 mA cm^{-2} with 1.0 M KOH and a feeding flow rate of 0.5 L min^{-1}. (c) J-V characteristics of 50 cm^2 hematite photoanode and two 50 cm^2 silicon heterojunction solar cells connected in series before and after long-term stability test for 1008 h. Reproduced with permission from Ref. [320], copyright (2018) Elsevier Ltd.
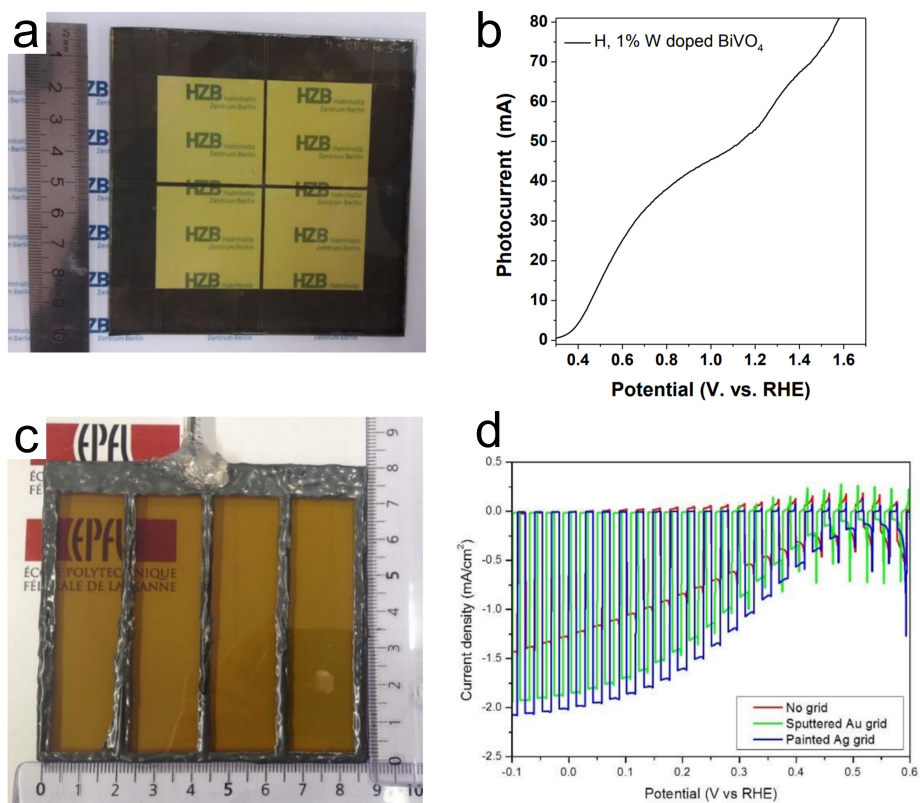
Figure 41. Large-scale fabrication of photoelectrodes. (a) Large-area $BiVO_4$ photoanode (7.1 × 7.1 cm^2). (b) J-V curve of large-area $BiVO_4$ photoanode (1 sun, 0.1 M phosphate + 0.5 M Na_2SO_3). (c) Large-area Cu_2O photocathode with grid lines (50.4 cm^2 active area). (d) Linear sweep voltammetry scans of large-area Cu_2O photocathode for the vertical PEC cell under chopped illumination (0.6 sun) in the pH 5 electrolyte. Reproduced from Ref. [321].

In the PECDEMO project, field tests were also conducted using two photoanode-PV systems under concentrated sunlight, *i.e.* $BiVO_4$-intrinsic thin layer (HIT) Si PV and Fe_2O_3-HIT Si PV (Figure 42).[322] Fe_2O_3-HIT Si PV (4 × 50 cm^2) reached maximum unbiased photocurrent density of 0.52 mA cm^{-2} in 1 M KOH under solar irradiance of 12.4-14.0 kW m^{-2}. For $BiVO_4$-HIT Si PV (8 × 50 cm^2), an average photocurrent density of 0.87 mA cm^{-2} and a maximum value of 1.88 mA cm^{-2} were achieved in 0.5 M K_2SO_4 + 0.1 M K_2HPO_4/KH_2PO_4 buffer with pH 7 at ~13 kW m^{-2}. A STH efficiency of 0.058% was maintained over 15 h operation for Fe_2O_3-HIT Si PV. However, the STH efficiency for $BiVO_4$-HIT Si PV fluctuated between 0.12% and 0.42%, which was attributed to the large

intermittence of outdoor solar irradiation. In the Artiphyction project, a photoanode-PV system was developed. The 1.6 m^2 prototype was made of 100 PEC cells for direct production of hydrogen via solar-driven water splitting, which showed a STH efficiency of up to ~3% (Figure 43).[323] Each cell consisted of a 8 × 8 cm^2 CoPi/Mo:BiVO$_4$ photoanode fabricated by spin-coating and Co nanoparticle electrocatalyst on the cathode. Notably, the cells were biased with Si PV with the maximum output matched well with each photoanode, resulting in an overall H$_2$ production rate of above 1 g h^{-1}. During long-term operation, the STH efficiency decreased to ~2%, which could be attributed to the bubbles-induced optical losses.
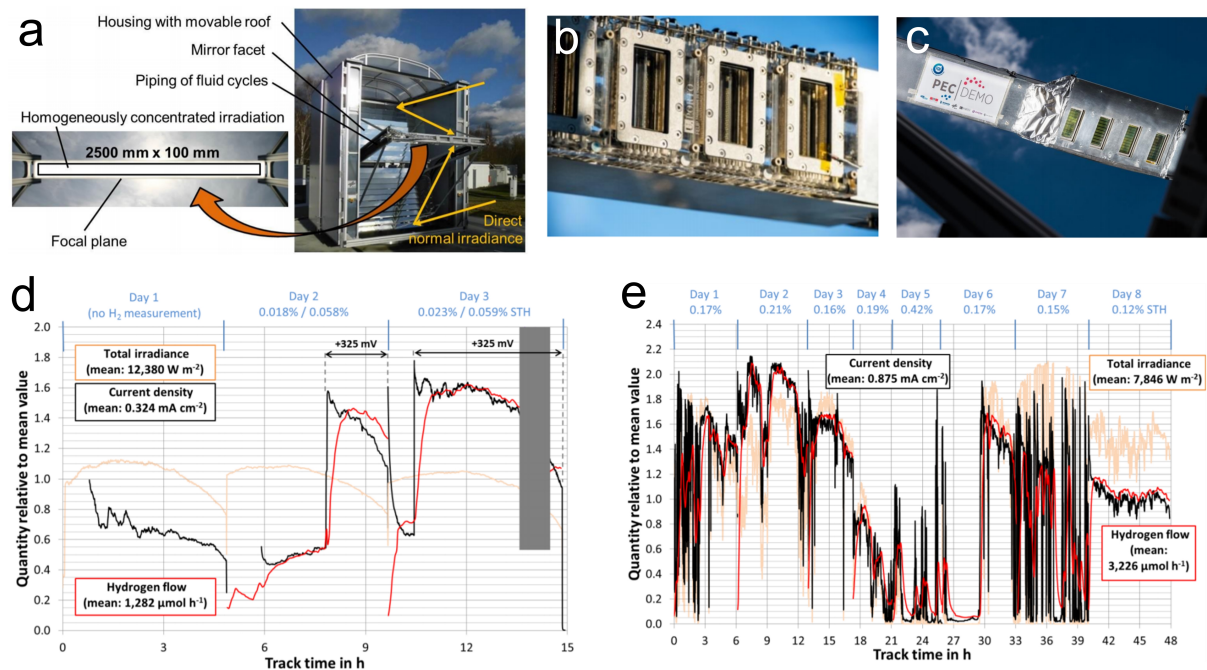
Figure 42. Photoanode-PV devices under concentrated sunlight. (a) The test facility SoCRatus of German Aerospace Center with its main components. (b) Modular prototype with hematite photoanodes (4 × 50 cm^2) mounted in the focal plane of the SoCRatus (here without reflective shields). (c) Modular prototype equipped with BiVO$_4$ photoanodes (8 × 50 cm^2) irradiated with concentrated sunlight in the focal plane of the SoCRatus with reflective shields to protect sensitive parts of the setup. (d) Total irradiation on the prototype, average current density, and hydrogen flow relative to respective mean values as well as average STH
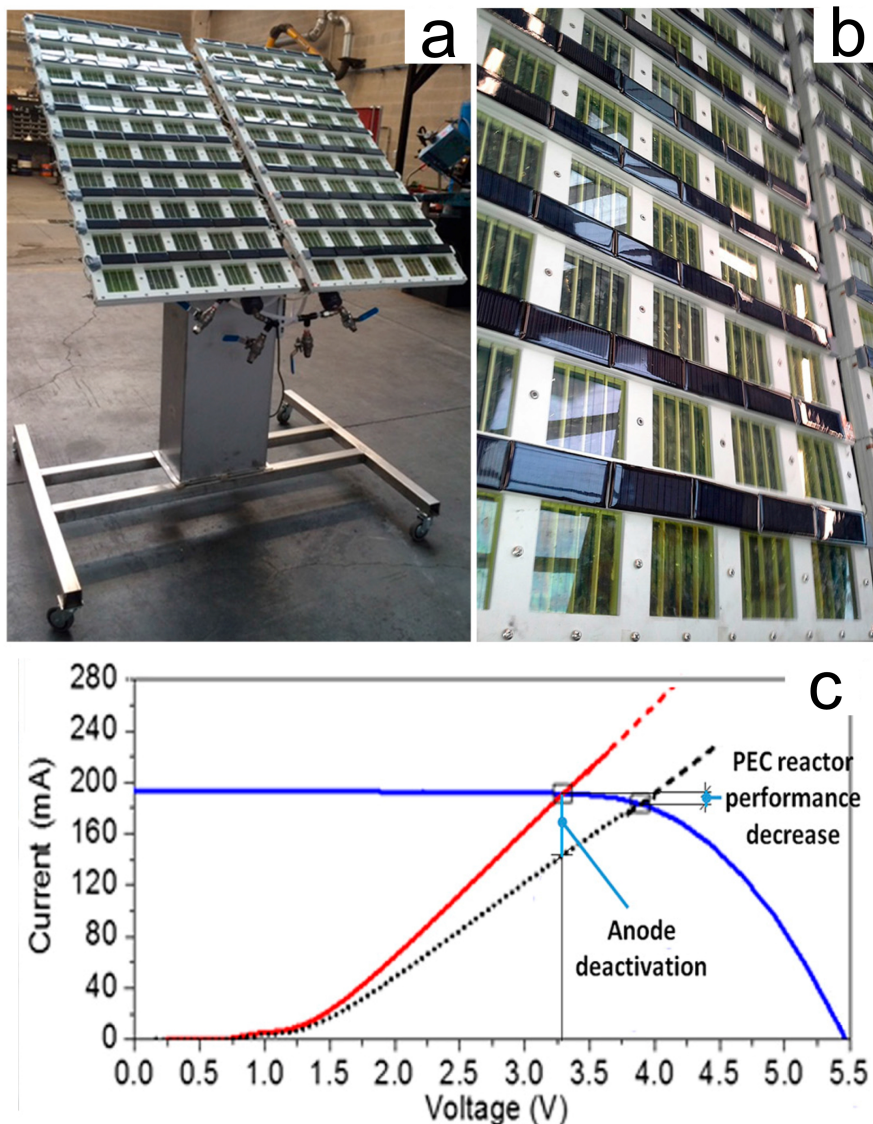
Figure 43. (a) Photograph and (b) close view of the 1.6 m^2 Artiphyction prototype made of 100 PEC cells (each of them included an 8 × 8 cm^2 $BiVO_4$-based photoanode and Co nanoparticles as cathode) for direct hydrogen production via solar-driven water splitting. (c) J-V curve for a single PEC window. Blue line: I-V power generation curve of the Si PV for

each window; red and black line/dotted line: initial and final PEC cell performance under 1 sun irradiation (AM 1.5 G); light-blue lines: possible performance degradation of a PEC cell prototype. Reproduced with permission from Ref. [324], copyright (2017) MDPI.

Encouragingly, Haussener and co-workers used active thermal management for a concentrated PEC device to reach current densities of higher than 0.88 A cm^{-2} at STH efficiencies of above 15%, which were among the highest operating current densities at high efficiency.[325] Conduction and forced convection were employed to cool the photoabsorber that suffered from larger losses at higher temperatures, and heat up the catalytic sites, which showed smaller overpotential at higher temperatures, with the excess heat from the photoabsorber (Figure 44). The device consisted of a triple-junction InGaP/InGaAs/Ge PV with an active area of 4 cm^2, platinized titanium gas diffusion layers, 25 cm^2 Nafion 115 membrane coated with InRuO$_x$-Pt catalysts and 3D-printed titanium anodic and cathodic flow plates. The highest current density of 0.88 A cm^{-2} and photovoltaic current density of 6.04 A cm^{-2} were achieved at irradiation concentration of 474 kW m^{-2}, while the stability of the integrated device was confirmed by the measured stable hydrogen flow rate for 2 h at lower irradiation concentration of 117 kW m^{-2}. The authors also pointed out that it is only practical for competitive implementation when the PEC devices can operate at both high current densities and high STH efficiencies. Recently, more and more recent works have focused on the development and optimization of up-scaled devices for solar-driven water splitting (Table 5), gradually addressing the obstacles to achieving commercially viable large-scale solar hydrogen production.
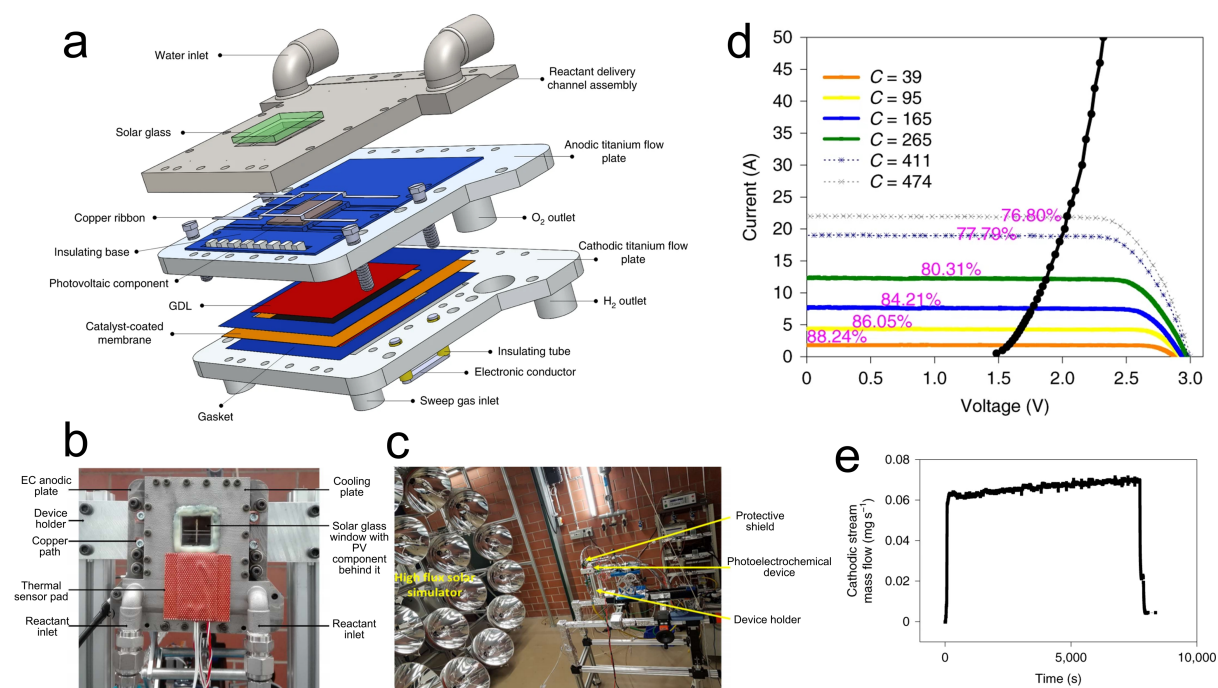
Figure 44. (a) Illustration of the integrated PEC device. (b) Photo of the fabricated and tested concentrated PEC device mounted on the test bench. (c) Photo of the test bench with the PEC device mounted on an adjustable chassis via a device holder, with the high-flux solar simulator on the left and the PEC device on the chassis on the right. (d) Measured characteristic *I–V* curves of the photovoltaic and electrochemical components (measured separately) of the concentrated PEC device at varying irradiation concentrations. (e) Longer-term test (total time of about 2 h) with a stable output hydrogen flow rate at irradiation concentration of 117 kW m^{-2}. Reproduced with permission from Ref. [325], copyright (2019) Nature Publishing Group.

Table 5. Selected up-scaled photoelectrode-PV and PV-electrolysis devices for solar-driven water splitting.

Cell structure	Illumination condition	Size (cm^2)	STH Efficiency	Stability	Electrolyte	Ref.
Fe$_2$O$_3$ + Si	1 sun	50	0.6%	1008 h,	1 M KOH	[320]

heterojunction PV		(photoanode), 2×50 (PV)		stable current		
Fe_2O_3 + HIT Si PV	12.4-14.0 suns	4 × 50 (photoanode)	0.058%	15 h, stable current	1 M KOH	[322]
$BiVO_4$ + HIT Si PV	~13 suns	8 × 50 (photoanode)	0.12%-0.42%	48 h (outdoor)	0.5 M K_2SO_4 + 0.1 M K_2HPO_4/KH_2PO_4	[322]
CoPi/Mo:$BiVO_4$ + Si PV	1 sun	100 × 64 (photoanode)	~3%	300 h, 19% current loss	0.1 M KPi	[323]
WO_3 + DSSC	1 sun	130.56 (photoanode)	1.41%	Not reported	0.5 M H_2SO_4	[306]
Ni-Ni + c-Si PV	1 sun	60 (electrodes), 5.7 (PV)	14.2%	100 h, stable current	1 M KOH	[284]
NiB_i-NiMoZn + c-Si PV	1 sun	6 (PV)	10%	168 h, stable current	0.5 M KB_i/0.5 M K_2SO_4	[282]
PEM electrolyser, InRuO$_x$-Pt + InGaP/InGaAs/Ge PV	474 suns	4 (PV), 25 (PEM)	>15%, 0.88 A/cm^2	2 h, stable current	Water	[325]
PEM electrolyser Ti-Ti + III-V PV	Concentrated	8 × 0.36 (PV)	19.8%, 0.8 A/cm^2	60 days (outdoor)	Water	[295]

Pt-IrO$_x$ + a-Si:H/a-Si:H/μc-Si:H PV	1 sun	50 (electrodes), 64 × 1 (PV)	4.8%	80 min, stable current	1 M H$_2$SO$_4$	[285]
Ni-Ni + a-Si:H or a-Si:H/μc-Si:H PV	1 sun	52.8 (electrodes)	~3.9%	3 h, stable H$_2$ production rate	1 M KOH	[239]

6. Techno-economic aspect

Unlike in fundamental research where gaining insight in to processes that occur in nature is the most important aspect of the work, the success of an applied technology depends on its profitability which is the major driving force of its adoption. Being emerging technologies, most of the solar hydrogen production methods discussed in this article are still in the research stage. Economic assessment of these technologies is made difficult by the unavailability of key components in the market, which necessitates coarse assumptions. As the assumptions are not standardized, direct comparison between different techno-economic studies provides little insight and should not be used to judge the relative viability of the solar hydrogen technologies. Nevertheless, they do provide an important perspective to the direction of future research.

Modular PEC water splitting has received the most techno-economic study so far, because photovoltaics and water electrolysis are well established industrially. As shown in Table 6 the levelized cost of hydrogen (LCH) estimated by different authors varies from 4.7 to over 13 USD/kg. Note that all the LCH data in the table have been converted to equivalent USD in 2019. An important technological assumption leading to the variation is the capacity factor of the electrolyzer unit, *i.e.* the ratio between average actual production rate and design capacity.

It directly determines the size and hence capital cost of the electrolyzer. At the lower bound of LCH, the electrolyzer is assumed to operate at constant full capacity equal to the designed hydrogen production rate.[326] The resulting model thus includes a minimally sized electrolysis plant, the capital cost of which accounts for less than 15% of the LCH in the case of PEM electrolyzer,[326] similar to the case of grid-powered electrolysis.[327] Given the intermittent nature of solar power, however, this design is impractical without a proper energy storage system to provide a stable source of electricity. Another way of sizing the electrolyzer typically found at the upper bound of LCH is to match its capacity to the peak power of the photovoltaic plant so that all the photovoltaic power can be utilized by the electrolyzer.[328-329] It significantly increases the contribution of the capital cost of electrolyzer to LCH which can be up to 40%.[328] In such designs the electrolyzer capacity is severely underused. Grid electricity has been proposed as supplement to photovoltaic power to keep the electrolyzer operating at full capacity, but the main source of energy in this case became the grid.[328] As currently the grid is dominated by nonrenewable energy, such a design has a high carbon footprint, not to mention that the estimated LCH was still higher than that of grid-powered electrolysis (6.6 versus 5.9 USD/kg).

In recent years solid oxide steam electrolysis (SOSE) has been suggested as an energetically more efficient alternative to alkaline/PEM electrolysis due to the lower kinetic barrier and electrical potential of water splitting at high temperatures. However, at the present stage such advantage is offset by the high capital cost of the electrolyzer assembly and associated heating equipment, ending up with a higher LCH than using conventional electrolyzers.[329] In such systems the capital cost of SOSE exceeds that of photovoltaics. While it has been shown that integrating a concentrated solar thermal plant into the system to supply the heat and steam for SOSE could reduce the LCH to 6.6 USD/kg, the calculation was based on the optimistic assumption of 100% capacity factor for the electrolyzer.[330] LCH

of as low as 5.7 USD/kg has been estimated for similar systems,[331] but we note that the specific capital cost of the electrolyzer in this work, 0.17 USD/W, was an order of magnitude lower than the demonstrated value of 3-4 USD/W and even lower than the ~0.4 USD/W of PEM electrolyzers.[327, 330] Furthermore, the discount rate or interest rate used in the financial calculation has a major but often overlooked influence on the LCH. In fact, the sensitivity of levelized cost of energy from photovoltaics has been found to be highest towards the discount rate rather than energy efficiency or specific capital cost.[332] Indeed, optimistic values of 6% are found with reports of low LCH [326, 330] and more conservative values of 10-12% with high LCH.[328-329]

The economic feasibility of integrated and modular PEC water splitting has been directly compared in the same framework of assessment, with the former showing slight economic advantage (12.3 versus 13.1 USD/kg) because it does not require electrical interface equipment between the photovoltaic and electrolytic components.[328] However, this conclusion was based on the assumption of similar efficiency, lifetime, and cost of the photovoltaic and electrolytic components in the two technologies, which has not been testified so far. The same study suggested an improvement in LCH of integrated PEC to 10.0 USD/kg using solar concentrator and tracker. An important assumption leading to the improvement was a much higher STH efficiency to counter the cost of the concentrating and tracking apparatus. While the remarkable efficiency is supported by laboratory research, the high capital cost of the semiconductor material itself to achieve the efficiency limits the benefits and became the dominant factor in LCH. Similar results for integrated PEC have been reported in an earlier work where the estimated LCH for a non-concentrating system was 13.6 USD/kg.[33, 113] The LCH for concentrated PEC was much lower at 5.3 USD/kg compared to the recent study mainly due to more than 5 times lower capital cost of the PEC module assumed. Consequently, the sensitivity of LCH towards capital cost of the PEC

module dropped below that towards STH efficiency. It should be emphasized that no commercial process exists to date for the manufacture of the PEC modules and the LCH of 5.3 USD/kg was reached assuming the applicability of current manufacturing process for photovoltaic panels.

Remarkably, very low LCH of 2.1 and 4.2 USD/kg have been estimated for single semiconductor and Z-scheme photocatalytic water splitting, respectively, which is within the U. S. Department of Energy target and potentially competitive with hydrogen generated by methane steam reforming, which has an estimated cost of approximately 1.4 USD/kg.[33, 113, 328] However, it represents an optimistic outlook rather than an estimation based on current state of the art. The STH efficiency, in particular, far exceeds experimentally demonstrated maximum of 1-2% and the assumed lifetime of the catalyst (5 years) has yet to be realized. The effect of overestimating the efficiency can be observed in the sensitivity analysis of the Z-scheme system where reducing the STH to 2.5% led to a LCH of 6.8 USD/kg. Moreover, the proposed photocatalytic reactors constructed from thin polyethylene film present reliability issues in the outdoor environment. As the capital cost associated with the reactor materials accounts for ~6% (for the single semiconductor system) to ~24% (for the Z-scheme system) of the LCH, additional replacement cost incurred by a shorter lifetime than the assumed 5 years increases the LCH significantly.

Similar to modular PEC water splitting, biological hydrogen production by photofermentation of organic materials is possible based solely on existing technology. With a realistic STH efficiency of 1.5% and a hypothetical pond-type flow reactor, the lowest estimation for LCH of such systems has been 18.3 USD/kg.[333] The cost of feedstock, in this case acetic acid, had a remarkable contribution of ~27% to the LCH even at stoichiometric conversion efficiency. Incorporation of a dark fermentation step before photofermentation allows for the use of cheaper feedstock such as crop residue, potato peels, and molasses, but

93

the LCH has been estimated to be much higher at 25.1-62.6 USD/kg.[334-336] In these studies the LCH is dominated by the capital and replacement cost of photoreactors which were assumed to be polyethylene tubes with a lifetime of 1 year. It should be noted that the assumed lifetime of polyethylene is much shorter than in other reports discussed so far, and that the sizing of photoreactors is based on specific productivity instead of STH efficiency in Ref[333] where the calculated specific productivity is ~1.1 mmol/L·h. The sheer scale of the photoreactor rendered the cost related to all other factors insignificant. Hydrogen production by biophotolysis minimizes the need for organic feedstock, and the LCH in this case has again been shown to depend heavily on cost associated with the photoreactor which in turn is determined by STH efficiency of the process.[333] While attractive LCH of 3.9 USD/kg has been reported, the assumed STH efficiency of 9.2% is much higher than the testified value of ~1%, let alone the fact that stable oxygenic biophotolysis has not been demonstrated.[333]

Techno-economic studies on solar thermal hydrogen production are scarce, and the estimated LCH varies across an order of magnitude. The lowest reported value, 6.9 USD/kg, was derived from a hybrid sulfur cycle where H_2SO_4 is first pyrolyzed to H_2O, SO_2 and O_2, followed by absorption of the SO_2 and electrolysis of the resulting H_2SO_3 solution to produce hydrogen and regenerate H_2SO_4.[337] Compared with a metal oxide cycle based on $NiFe_2O_4$, it has the advantage of not requiring regular replacement of the active material. As a result, the reduced operating cost countered the increased capital cost incurred by the need for special corrosion-proof equipment and led to a lower LCH.[337] The cost of replacing the active material in metal oxide cycles has been estimated to account for 20% of the LCH.[338] Interestingly, the LCH of similar $NiFe_2O_4$-based systems differs by a factor of ~5 between the two works despite more than 2 times higher capital investment associated with the lower LCH.[337-338] One of the main reasons for the large discrepancy may be different STH efficiency, which is the determining factor in the economics of all the aforementioned solar

hydrogen production technologies. Unfortunately the value was not reported by one of the studies, preventing a direct comparison. Another possible source of discrepancy is the discount/interest rate as discussed earlier. The lower LCH was calculated using a value of 6% and the higher LCH 13%.

Table 6. Techno-economic assessment of various solar hydrogen production technologies

Type	Scale*	STH or specific H_2 productivity	LCH (USD/kg)	Ref.
Methane steam reforming	-	-	1.4	[328]
Photocatalytic, single semiconductor	10 t/d	10%	2.1	[33, 113]
Oxygenic biophotolysis	10 t/d	9.2%	3.9	[333]
Photocatalytic, Z-scheme	10 t/d	5%	4.2	[33, 113]
Photovoltaic PEM electrolysis	1 t/d	10.8%	4.7	[326]
Integrated PEC, 10x solar concentration and tracking	10 t/d	15%	5.3	[33, 113]
Anoxic biophotolysis	10 t/d	5.2%	5.5	[333]
Integrated photovoltaic-concentrated solar thermal SOSE	8 MW$_{PV}$	-	5.7	[331]
Grid-assisted photovoltaic PEM electrolysis	10 t/d	9.8%	6.6	[328]
Integrated photovoltaic-concentrated solar thermal SOSE	0.4 t/d	9.9%	6.6	[330]
Solar thermal hybrid H_2SO_4	50 MW$_{th}$ 10.2 t/d	-	6.9	[337]
Anoxic biophotolysis by immobilized green algae	10 t/d	2.25%	7.9	[333]
Photovoltaic SOSE	0.4 t/d	6.3%	8.4	[330]
Solar thermal NiFe$_2$O$_4$	50 MW$_{th}$ 11.4 t/d	-	8.6	[337]
Integrated PEC, 10x solar concentration and tracking	10 t/d	20%	10.0	[328]
Photovoltaic electrolysis	-	11.5%	10.0	[339]
Photovoltaic electrolysis, 10x solar concentration	-	-	10.1	[340]
Integrated PEC, fixed panel	10 t/d	9.8%	12.3	[328]
Photovoltaic SOSE	-	-	12.8	[329]
Photovoltaic PEM electrolysis	10 t/d	9.8%	13.1	[328]
Integrated PEC, fixed panel	10 t/d	10%	13.6	[33, 113]
Photo-fermentation	10 t/d	3.5% (1.5%)	13.6 (18.3)	[333]
Solar thermal CeO$_2$	90 MW$_{th}$	13.4%	14.7	[338]
Integrated dark/photo-fermentation	1.3 t/d	0.33 mmol/Lh	25.1	[335]
Integrated dark/photo-fermentation	1.4 t/d	0.5 mmol/Lh	37.5	[336]

| Solar thermal NiFe$_2$O$_4$ | 90 MW$_{th}$ | 6.4% | 43.8 | [338] |
| Integrated dark/photo-fermentation | 27.1 t/d | 0.21 mmol/Lh | 62.6 | [334] |

*Scale of the plant is expressed as mass rate of H$_2$ production, nominal power of the photovoltaic module (MW$_{PV}$), or nominal power of the solar thermal collector (MW$_{th}$).
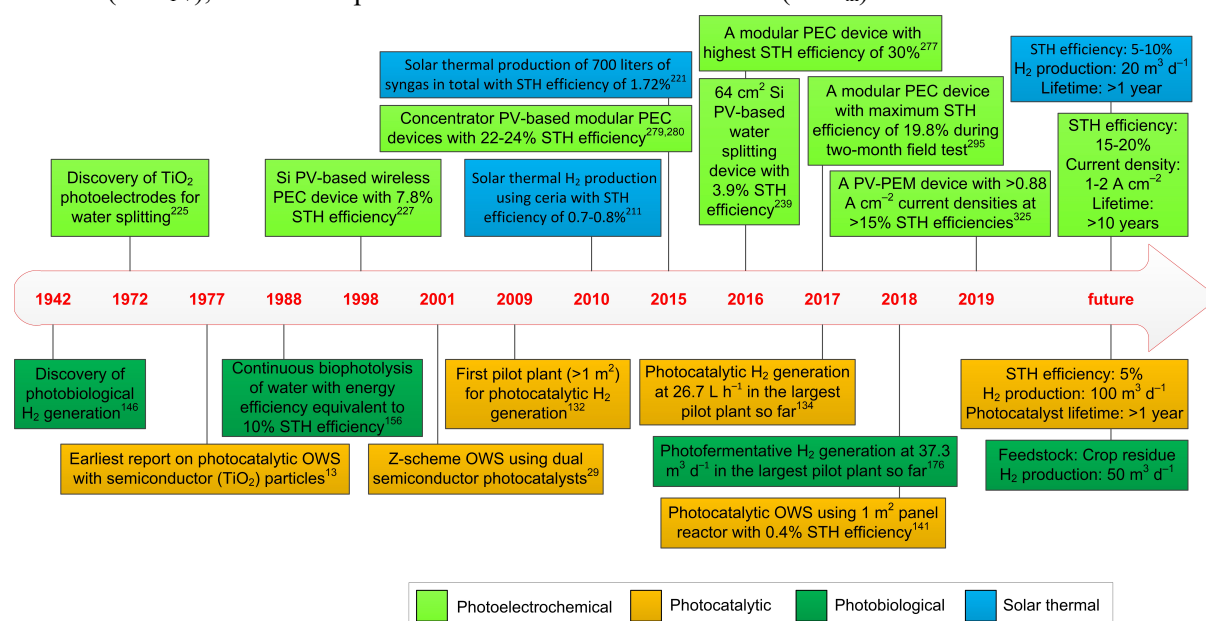
Figure 45. Timeline showing the key developments in solar hydrogen production from water.

Conclusions and Outlook

In summary, the recent research efforts towards practical solar H$_2$ generation have been reviewed, particularly on four different pathways which are photocatalytic, photobiological, solar thermal and photoelectrochemical hydrogen production. It is encouraging to note that beyond lab-scale studies, more and more research groups around the world start to develop larger-scale systems to potentially deliver solar H$_2$ production at affordable prices (Figure 45). Nonetheless, there exist formidable challenges to achieve such a goal among which solar to hydrogen conversion efficiency, materials and system long-term stability and performance consistency at large scale are the major limiting factors. While these factors are likely to remain relevant to all the aforementioned solar H$_2$ production technologies, we highlight that the most urgent issues preventing the upscaling of each technology are different as elaborated in Table 7. Furthermore, based on the current development status of the four solar hydrogen production pathways, we provide predictions about their threshold requirements to be achieved in the near future in Figure 45. At this stage, it is still unclear which pathway is

more promising as they differ from each other in terms of efficiency, cost and system complexity. However, fabrication of concentrator PV-electrolyser systems could be the most straightforward approach to achieve large-scale solar hydrogen production. Photobiological hydrogen production systems are more beneficial in areas where abundant feedstocks (e.g. crop residues) are available. A breakthrough is still required to significantly improve the commercial viability for both photocatalytic and solar thermal hydrogen production systems.

Table 7. Comparison of solar H_2 production technologies

Pathway to solar H_2 production	Advantages	Major obstacles to upscaling
Photocatalytic	Low materials cost Simple system	Low STH
Photobiological	Mature technology	Sensitivity to environment Need for organic feeds
Solar thermal	Efficient utilization of reactor volume	Low catalyst durability
Fully/Partially integrated PEC	High STH	Performance degradation at high current density
PV-electrolyser	High STH Mature technology	Intermittent power supply to electrolyser

Besides continuous efforts to overcome these obstacles through fundamental research, two aspects are suggested to be paid with more attention. Firstly, there are tremendous amounts of new research data and findings being constantly generated as more researchers enter into the field. Therefore, it is of critical importance that the existing findings are able to guide new research endeavour in the right direction to further advance the field towards practical use. To achieve this outcome in the area of solar hydrogen generation, it will be useful that certain standard and meaningful H_2 evolution reaction protocols are to be established across small to pilot scales. By doing so, data can be compared among different systems and with the state of the art. This has been probably done in PEC H_2 evolution research at the small scale, but not so in the other processes. Secondly, collaboration among different disciplines is highly desirable in order to spark innovative ideas. In the context of the current topic, it is suggested

that materials scientists and chemists who have achieved certain benchmark performance at lab scale should engage experts on process system engineering to understand further technical requirements before scaling up. As the field continues to develop, it is believed that more efforts shall be committed to translate the basic research findings to commercial applications. This is even more crucial for solar hydrogen production since it concerns long-term sustainability.

In addition, it is worth noting that carbon-based fuels, such as methane, carbon monoxide and methanol, can also be produced via the four pathways described in this review. The generated hydrogen and simple carbon-based fuels during solar-driven water splitting and carbon dioxide reduction processes can be used as feedstocks through existing industrial technologies to produce value-added fertilisers, plastics, pharmaceuticals, synthetic fuels for transport, etc.

Author Contributions

The manuscript was written through contributions of all authors. All authors have given approval to the final version of the manuscript.

Notes

The authors declare no competing financial interests.

References

(1) Ardo, S., Rivas, D. F., Modestino, M. A., Greiving, V. S., Abdi, F. F., Llado, E. A., Artero, V., Ayers, K., Battaglia, C., Becker, J. P., et al. Pathways to electrochemical solar-hydrogen technologies. *Energy Environ. Sci.* **11**, 2768-2783 (2018).

(2) Jacobson, M. Z., Colella, W. G., Golden, D. M. Cleaning the air and improving health with hydrogen fuel-cell vehicles. *Science* **308**, 1901-1905 (2005).

(3) Staffell, I., Scamman, D., Velazquez Abad, A., Balcombe, P., Dodds, P. E., Ekins, P., Shah, N., Ward, K. R. The role of hydrogen and fuel cells in the global energy system. *Energy Environ. Sci.* **12**, 463-491 (2019).

(4) Chu, S., Majumdar, A. Opportunities and challenges for a sustainable energy future. *Nature* **488**, 294-303 (2012).

(5) Cook, T. R., Dogutan, D. K., Reece, S. Y., Surendranath, Y., Teets, T. S., Nocera, D. G. Solar Energy Supply and Storage for the Legacy and Nonlegacy Worlds. *Chem. Rev.* **110**, 6474-6502 (2010).

(6) Armaroli, N., Balzani, V. The Hydrogen Issue. *Chemsuschem* **4**, 21-36 (2011).

(7) Sathre, R., Scown, C. D., Morrow, W. R., Stevens, J. C., Sharp, I. D., Ager, J. W., Walczak, K., Houle, F. A., Greenblatt, J. B. Life-cycle net energy assessment of large-scale hydrogen production via photoelectrochemical water splitting. *Energy Environ. Sci.* **7**, 3264-3278 (2014).

(8) Ager, J. W., Shaner, M. R., Walczak, K. A., Sharp, I. D., Ardo, S. Experimental demonstrations of spontaneous, solar-driven photoelectrochemical water splitting. *Energy Environ. Sci.* **8**, 2811-2824 (2015).

(9) Kim, J. H., Hansora, D., Sharma, P., Jang, J. W., Lee, J. S. Toward practical solar hydrogen production - an artificial photosynthetic leaf-to-farm challenge. *Chem. Soc. Rev.* **48**, 1908-1971 (2019).

(10) He, Y. M., Wang, D. W. Toward Practical Solar Hydrogen Production. *Chem-Us* **4**, 405-408 (2018).

(11) Ronge, J., Bosserez, T., Martel, D., Nervi, C., Boarino, L., Taulelle, F., Decher, G., Bordiga, S., Martens, J. A. Monolithic cells for solar fuels. *Chem. Soc. Rev.* **43**, 7963-7981 (2014).

(12) Yamada, T., Domen, K. Development of Sunlight Driven Water Splitting Devices towards Future Artificial Photosynthetic Industry. *ChemEngineering* **2**, 36 (2018).

(13) Schrauzer, G. N., Guth, T. D. Photolysis of Water and Photoreduction of Nitrogen on Titanium Dioxide. *J. Am. Chem. Soc.* **99**, 7189-7193 (1977).

(14) Bolton, J. R., Strickler, S. J., Connolly, J. S. Limiting and realizable efficiencies of solar photolysis of water. *Nature* **316**, 495-500 (1985).

(15) Seitz, L. C., Chen, Z., Forman, A. J., Pinaud, B. A., Benck, J. D., Jaramillo, T. F. Modeling Practical Performance Limits of Photoelectrochemical Water Splitting Based on the Current State of Materials Research. *ChemSusChem* **7**, 1372-1385 (2014).

(16) Ma, Y., Wang, X., Jia, Y., Chen, X., Han, H., Li, C. Titanium dioxide-based nanomaterials for photocatalytic fuel generations. *Chem. Rev.* **114**, 9987-10043 (2014).

(17) Ham, Y., Hisatomi, T., Goto, Y., Moriya, Y., Sakata, Y., Yamakata, A., Kubota, J., Domen, K. Flux-mediated doping of $SrTiO_3$ photocatalysts for efficient overall water splitting. *J. Mater. Chem. A* **4**, 3027-3033 (2016).

(18) Kato, H., Asakura, K., Kudo, A. Highly efficient water splitting into H_2 and O_2 over lanthanum-doped $NaTaO_3$ photocatalysts with high crystallinity and surface nanostructure. *J. Am. Chem. Soc.* **125**, 3082-9 (2003).

(19) Maeda, K., Domen, K. Solid Solution of GaN and ZnO as a Stable Photocatalyst for Overall Water Splitting under Visible Light. *Chem. Mater.* **22**, 612-623 (2010).

(20) Ong, W.-J., Tan, L.-L., Ng, Y. H., Yong, S.-T., Chai, S.-P. Graphitic Carbon Nitride (g-C$_3$N$_4$)-Based Photocatalysts for Artificial Photosynthesis and Environmental Remediation: Are We a Step Closer To Achieving Sustainability? *Chem. Rev.* **116**, 7159-7329 (2016).

(21) Zhang, P., Wang, T., Gong, J. Current Mechanistic Understanding of Surface Reactions over Water-Splitting Photocatalysts. *Chem* **4**, 223-245 (2018).

(22) Meissner, D., Memming, R., Kastening, B. Photoelectrochemistry of cadmium sulfide. 1. Reanalysis of photocorrosion and flat-band potential. *J. Phys. Chem.* **92**, 3476-3483 (1988).

(23) van Sark, W. G. J. H. M., Frederix, P. L. T. M., Van den Heuvel, D. J., Gerritsen, H. C., Bol, A. A., van Lingen, J. N. J., de Mello Donegá, C., Meijerink, A. Photooxidation and Photobleaching of Single CdSe/ZnS Quantum Dots Probed by Room-Temperature Time-Resolved Spectroscopy. *J. Phys. Chem. B* **105**, 8281-8284 (2001).

(24) Baker, D. R., Lundgren, C. A. Electrochemical determination of the gallium-nitride photocorrosion potential in acidic media. *J. Mater. Chem. A* **5**, 20978-20984 (2017).

(25) Sayad, Y., Kaminski, A., Blanc, D., Nouiri, A., Lemiti, M. Determination of diffusion length in photovoltaic crystalline silicon by modelisation of light beam induced current. *Superlattices Microstruct.* **45**, 393-401 (2009).

(26) Salvador, P. Hole diffusion length in n-TiO$_2$ single crystals and sintered electrodes: Photoelectrochemical determination and comparative analysis. *J. Appl. Phys.* **55**, 2977-2985 (1984).

(27) Takanabe, K. Photocatalytic Water Splitting: Quantitative Approaches toward Photocatalyst by Design. *ACS Catal.* **7**, 8006-8022 (2017).

(28) Bard, A. J. Photoelectrochemistry and heterogeneous photo-catalysis at semiconductors. *J. Photochem.* **10**, 59-75 (1979).

(29) Abe, R., Sayama, K., Domen, K., Arakawa, H. A new type of water splitting system composed of two different TiO$_2$ photocatalysts (anatase, rutile) and a IO$_3^-$/I$^-$ shuttle redox mediator. *Chem. Phys. Lett.* **344**, 339-344 (2001).

(30) Wang, Q., Hisatomi, T., Suzuki, Y., Pan, Z., Seo, J., Katayama, M., Minegishi, T., Nishiyama, H., Takata, T., Seki, K., et al. Particulate Photocatalyst Sheets Based on Carbon Conductor Layer for Efficient Z-Scheme Pure-Water Splitting at Ambient Pressure. *J. Am. Chem. Soc.* **139**, 1675-1683 (2017).

(31) Wang, Y., Suzuki, H., Xie, J., Tomita, O., Martin, D. J., Higashi, M., Kong, D., Abe, R., Tang, J. Mimicking Natural Photosynthesis: Solar to Renewable H_2 Fuel Synthesis by Z-Scheme Water Splitting Systems. *Chem. Rev.* **118**, 5201-5241 (2018).

(32) Chen, S., Takata, T., Domen, K. Particulate photocatalysts for overall water splitting. *Nat. Rev. Mater.* **2**, (2017).

(33) James, B. D., Baum, G. N., Perez, J., Baum, K. N. Technoeconomic Analysis of Photoelectrochemical (PEC) Hydrogen Production. *DOE Report*, (2009).

(34) Fajrina, N., Tahir, M. A critical review in strategies to improve photocatalytic water splitting towards hydrogen production. *Int. J. Hydrogen Energy*, (2018).

(35) Qi, J., Zhang, W., Cao, R. Solar-to-Hydrogen Energy Conversion Based on Water Splitting. *Adv. Energy Mater.* **8**, (2018).

(36) Stolarczyk, J. K., Bhattacharyya, S., Polavarapu, L., Feldmann, J. Challenges and Prospects in Solar Water Splitting and CO_2 Reduction with Inorganic and Hybrid Nanostructures. *ACS Catal.* **8**, 3602-3635 (2018).

(37) Su, T., Shao, Q., Qin, Z., Guo, Z., Wu, Z. Role of Interfaces in Two-Dimensional Photocatalyst for Water Splitting. *ACS Catal.* **8**, 2253-2276 (2018).

(38) Wang, Z., Li, C., Domen, K. Recent developments in heterogeneous photocatalysts for solar-driven overall water splitting. *Chem. Soc. Rev.* **48**, 2109-2125 (2019).

(39) Takata, T., Domen, K. Particulate Photocatalysts for Water Splitting: Recent Advances and Future Prospects. *ACS Energy Lett.* **4**, 542-549 (2019).

(40) Chen, X., Shen, S., Guo, L., Mao, S. S. Semiconductor-based photocatalytic hydrogen generation. *Chem. Rev.* **110**, 6503-70 (2010).

(41) Asai, R., Nemoto, H., Jia, Q., Saito, K., Iwase, A., Kudo, A. A visible light responsive rhodium and antimony-codoped SrTiO3 powdered photocatalyst loaded with an IrO2 cocatalyst for solar water splitting. *Chem. Commun. (Cambridge, U. K.)* **50**, 2543-6 (2014).

(42) Pan, C., Takata, T., Nakabayashi, M., Matsumoto, T., Shibata, N., Ikuhara, Y., Domen, K. A complex perovskite-type oxynitride: the first photocatalyst for water splitting operable at up to 600 nm. *Angew. Chem. Int. Ed. Engl.* **54**, 2955-9 (2015).

(43) Maeda, K., Takata, T., Hara, M., Saito, N., Inoue, Y., Kobayashi, H., Domen, K. GaN:ZnO solid solution as a photocatalyst for visible-light-driven overall water splitting. *J. Am. Chem. Soc.* **127**, 8286-7 (2005).

(44) Li, R., Li, C. Photocatalytic Water Splitting on Semiconductor-Based Photocatalysts. 2017; pp 1-57.

(45) Marschall, R. Semiconductor Composites: Strategies for Enhancing Charge Carrier Separation to Improve Photocatalytic Activity. *Adv. Funct. Mater.* **24**, 2421-2440 (2014).

(46) Moniz, S. J. A., Shevlin, S. A., Martin, D. J., Guo, Z.-X., Tang, J. Visible-light driven heterojunction photocatalysts for water splitting – a critical review. *Energy Environ. Sci.* **8**, 731-759 (2015).

(47) Chen, S., Qi, Y., Li, C., Domen, K., Zhang, F. Surface Strategies for Particulate Photocatalysts toward Artificial Photosynthesis. *Joule* **2**, 2260-2288 (2018).

(48) Maeda, K., Teramura, K., Domen, K. Effect of post-calcination on photocatalytic activity of $(Ga_{1-x}Zn_x)(N_{1-x}O_x)$ solid solution for overall water splitting under visible light. *J. Catal.* **254**, 198-204 (2008).

(49) Guo, L., Chen, Y., Su, J., Liu, M., Liu, Y. Obstacles of solar-powered photocatalytic water splitting for hydrogen production: A perspective from energy flow and mass flow. *Energy* **172**, 1079-1086 (2019).

(50) Domen, K., Naito, S., Soma, M., Onishi, T., Tamaru, K. Photocatalytic decomposition of water vapour on an NiO–SrTiO$_3$ catalyst. *J. Chem. Soc., Chem. Commun.*, 543-544 (1980).

(51) Cao, S., Wang, C. J., Fu, W. F., Chen, Y. Metal Phosphides as Co-Catalysts for Photocatalytic and Photoelectrocatalytic Water Splitting. *ChemSusChem* **10**, 4306-4323 (2017).

(52) Han, B., Hu, Y. H. MoS2as a co-catalyst for photocatalytic hydrogen production from water. *Energy Sci. Eng.* **4**, 285-304 (2016).

(53) Morikawa, T., Sato, S., Sekizawa, K., Arai, T., Suzuki, T. M. Molecular Catalysts Immobilized on Semiconductor Photosensitizers for Proton Reduction toward Visible-Light-Driven Overall Water Splitting. *ChemSusChem* **12**, 1807-1824 (2019).

(54) Yan, H., Yang, J., Ma, G., Wu, G., Zong, X., Lei, Z., Shi, J., Li, C. Visible-light-driven hydrogen production with extremely high quantum efficiency on Pt–PdS/CdS photocatalyst. *J. Catal.* **266**, 165-168 (2009).

(55) Maeda, K., Xiong, A., Yoshinaga, T., Ikeda, T., Sakamoto, N., Hisatomi, T., Takashima, M., Lu, D., Kanehara, M., Setoyama, T., et al. Photocatalytic overall water splitting promoted by two different cocatalysts for hydrogen and oxygen evolution under visible light. *Angew. Chem. Int. Ed. Engl.* **49**, 4096-9 (2010).

(56) Yang, J., Wang, D., Han, H., Li, C. Roles of cocatalysts in photocatalysis and photoelectrocatalysis. *Acc. Chem. Res.* **46**, 1900-9 (2013).

(57) Brooks, J. L., Warkentin, C. L., Saha, D., Keller, E. L., Frontiera, R. R. Toward a mechanistic understanding of plasmon-mediated photocatalysis. *Nanophotonics* **7**, 1697-1724 (2018).

(58) Hou, W., Cronin, S. B. A Review of Surface Plasmon Resonance-Enhanced Photocatalysis. *Adv. Funct. Mater.* **23**, 1612-1619 (2013).

(59) Yoshida, M., Takanabe, K., Maeda, K., Ishikawa, A., Kubota, J., Sakata, Y., Ikezawa, Y., Domen, K. Role and Function of Noble-Metal/Cr-Layer Core/Shell Structure Cocatalysts for Photocatalytic Overall Water Splitting Studied by Model Electrodes. *J. Phys. Chem. C* **113**, 10151-10157 (2009).

(60) Garcia-Esparza, A. T., Shinagawa, T., Ould-Chikh, S., Qureshi, M., Peng, X., Wei, N., Anjum, D. H., Clo, A., Weng, T. C., Nordlund, D., et al. An Oxygen-Insensitive Hydrogen Evolution Catalyst Coated by a Molybdenum-Based Layer for Overall Water Splitting. *Angew. Chem. Int. Ed. Engl.* **56**, 5780-5784 (2017).

(61) Yi, S.-S., Zhang, X.-B., Wulan, B.-R., Yan, J.-M., Jiang, Q. Non-noble metals applied to solar water splitting. *Energy Environ. Sci.* **11**, 3128-3156 (2018).

(62) Zou, X., Zhang, Y. Noble metal-free hydrogen evolution catalysts for water splitting. *Chem. Soc. Rev.* **44**, 5148-80 (2015).

(63) Zhang, B., Zheng, X., Voznyy, O., Comin, R., Bajdich, M., Garcia-Melchor, M., Han, L., Xu, J., Liu, M., Zheng, L., et al. Homogeneously dispersed multimetal oxygen-evolving catalysts. *Science* **352**, 333-7 (2016).

(64) Liu, J., Liu, Y., Liu, N., Han, Y., Zhang, X., Huang, H., Lifshitz, Y., Lee, S. T., Zhong, J., Kang, Z. Water splitting. Metal-free efficient photocatalyst for stable visible water splitting via a two-electron pathway. *Science* **347**, 970-4 (2015).

(65) Thanh, N. T. K., Maclean, N., Mahiddine, S. Mechanisms of Nucleation and Growth of Nanoparticles in Solution. *Chem. Rev.* **114**, 7610-7630 (2014).

(66) Fu, W., Xue, F., Liu, M. Kilogram-scale production of highly active chalcogenide photocatalyst for solar hydrogen generation. *Int. J. Hydrogen Energy* **43**, 13738-13744 (2018).

(67) Liu, M., Wang, L., Lu, G., Yao, X., Guo, L. Twins in $Cd_{1-x}Zn_xS$ solid solution: Highly efficient photocatalyst for hydrogen generation from water. *Energy Environ. Sci.* **4**, (2011).

(68) Baghbanzadeh, M., Carbone, L., Cozzoli, P. D., Kappe, C. O. Microwave-assisted synthesis of colloidal inorganic nanocrystals. *Angew. Chem. Int. Ed. Engl.* **50**, 11312-59 (2011).

(69) Hwang, J.-Y., Shi, S., Xu, Z., Peterson, K. W. Synthesis of Monodispersed Iron Oxide Particles by a Large-Scale Microwave Reactor. *Chem. Eng. Commun.* **193**, 1586-1591 (2007).

(70) Pan, L., Liu, X., Sun, Z., Sun, C. Q. Nanophotocatalysts via microwave-assisted solution-phase synthesis for efficient photocatalysis. *J. Mater. Chem. A* **1**, (2013).

(71) Thostenson, E. T., Chou, T. W. Microwave processing: fundamentals and applications. *Composites, Part A* **30**, 1055-1071 (1999).

(72) Xiao, J., Liu, P., Wang, C. X., Yang, G. W. External field-assisted laser ablation in liquid: An efficient strategy for nanocrystal synthesis and nanostructure assembly. *Prog. Mater. Sci.* **87**, 140-220 (2017).

(73) Liao, L., Zhang, Q., Su, Z., Zhao, Z., Wang, Y., Li, Y., Lu, X., Wei, D., Feng, G., Yu, Q., et al. Efficient solar water-splitting using a nanocrystalline CoO photocatalyst. *Nat. Nanotechnol.* **9**, 69-73 (2014).

(74) Jedsukontorn, T., Ueno, T., Saito, N., Hunsom, M. Facile preparation of defective black TiO_2 through the solution plasma process: Effect of parametric changes for plasma discharge on its structural and optical properties. *J. Alloys Compd.* **726**, 567-577 (2017).

(75) Zhang, Z. K., Bai, M. L., Guo, D. Z., Hou, S. M., Zhang, G. M. Plasma-electrolysis synthesis of TiO_2 nano/microspheres with optical absorption extended into the infra-red region. *Chem. Commun. (Cambridge, U. K.)* **47**, 8439-41 (2011).

(76) Wu, J., Li, N., Fang, H.-B., Li, X., Zheng, Y.-Z., Tao, X. Nitrogen vacancies modified graphitic carbon nitride: Scalable and one-step fabrication with efficient visible-light-driven hydrogen evolution. *Chem. Eng. J.* **358**, 20-29 (2019).

(77) Yuan, Y.-P., Yin, L.-S., Cao, S.-W., Gu, L.-N., Xu, G.-S., Du, P., Chai, H., Liao, Y.-S., Xue, C. Microwave-assisted heating synthesis: a general and rapid strategy for large-scale production of highly crystalline g-C_3N_4 with enhanced photocatalytic H2 production. *Green Chem.* **16**, 4663-4668 (2014).

(78) Kimura, T. Molten Salt Synthesis of Ceramic Powders. In *Advances in Ceramics*; Sikalidis, C., Ed.; IntechOpen: 2011.

(79) Sun, J., Chen, G., Pei, J., Jin, R., Wang, Q., Guang, X. A simple approach to strontium sodium tantalite mesocrystals with ultra-high photocatalytic properties for water splitting. *J. Mater. Chem.* **22**, (2012).

(80) Darr, J. A., Zhang, J., Makwana, N. M., Weng, X. Continuous Hydrothermal Synthesis of Inorganic Nanoparticles: Applications and Future Directions. *Chem. Rev.* **117**, 11125-11238 (2017).

(81) Makwana, N. M., Tighe, C. J., Gruar, R. I., McMillan, P. F., Darr, J. A. Pilot plant scale continuous hydrothermal synthesis of nano-titania; effect of size on photocatalytic activity. *Mater. Sci. Semicond. Process.* **42**, 131-137 (2016).

(82) Gruar, R. I., Tighe, C. J., Darr, J. A. Scaling-up a Confined Jet Reactor for the Continuous Hydrothermal Manufacture of Nanomaterials. *Ind. Eng. Chem. Res.* **52**, 5270-5281 (2013).

(83) Weng, X., Zeng, Q., Zhang, Y., Dong, F., Wu, Z. Facile Approach for the Syntheses of Ultrafine TiO_2 Nanocrystallites with Defects and C Heterojunction for Photocatalytic Water Splitting. *ACS Sustain. Chem. Eng.* **4**, 4314-4320 (2016).

(84) Hakuta, Y., Hayashi, H., Arai, K. Hydrothermal synthesis of photocatalyst potassium hexatitanate nanowires under supercritical conditions. *J. Mater. Sci.* **39**, 4977-4980 (2004).

(85) Evonik Industries AEROSIL® – Fumed Silica Technical Overview. http://www.aerosil.com/sites/lists/RE/DocumentsSI/Technical-Overview-AEROSIL-Fumed-Silica-EN.pdf (accessed December 2017).

(86) Liu, G., Ye, S., Yan, P., Xiong, F., Fu, P., Wang, Z., Chen, Z., Shi, J., Li, C. Enabling an integrated tantalum nitride photoanode to approach the theoretical photocurrent limit for solar water splitting. *Energy Environ. Sci.* **9**, 1327-1334 (2016).

(87) Sheng, Y., Kraft, M., Xu, R. Emerging applications of nanocatalysts synthesized by flame aerosol processes. *Curr. Opin. Chem. Eng.* **20**, 39-49 (2018).

(88) Chiarello, G. L., Dozzi, M. V., Selli, E. TiO_2 -based materials for photocatalytic hydrogen production. *J. Energy Chem.* **26**, 250-258 (2017).

(89) Chiarello, G. L., Dozzi, M. V., Scavini, M., Grunwaldt, J.-D., Selli, E. One step flame-made fluorinated Pt/TiO_2 photocatalysts for hydrogen production. *Appl. Catal., B* **160-161**, 144-151 (2014).

(90) Mueller, R., Mädler, L., Pratsinis, S. E. Nanoparticle synthesis at high production rates by flame spray pyrolysis. *Chem. Eng. Sci.* **58**, 1969-1976 (2003).

(91) Wu, S., Wang, W., Tu, W., Yin, S., Sheng, Y., Manuputty, M. Y., Kraft, M., Xu, R. Premixed Stagnation Flame Synthesized TiO_2 Nanoparticles with Mixed Phases for Efficient Photocatalytic Hydrogen Generation. *ACS Sustain. Chem. Eng.* **6**, 14470-14479 (2018).

(92) Fu, J., Daanen, N. N., Rugen, E. E., Chen, D. P., Skrabalak, S. E. Simple Reactor for Ultrasonic Spray Synthesis of Nanostructured Materials. *Chem. Mater.* **29**, 62-68 (2016).

(93) Manuputty, M. Y., Dreyer, J. A. H., Sheng, Y., Bringley, E. J., Botero, Maria L., Akroyd, J., Kraft, M. Polymorphism of nanocrystalline TiO_2 prepared in a stagnation flame: formation of the TiO_2-II phase. *Chem. Sci.*, (2019).

(94) Teoh, W. Y. A Perspective on the Flame Spray Synthesis of Photocatalyst Nanoparticles. *Materials (Basel)* **6**, 3194-3212 (2013).

(95) Kho, Y. K., Teoh, W. Y., Iwase, A., Madler, L., Kudo, A., Amal, R. Flame preparation of visible-light-responsive $BiVO_4$ oxygen evolution photocatalysts with subsequent activation via aqueous route. *ACS Appl. Mater. Interfaces* **3**, 1997-2004 (2011).

(96) Kang, H. W., Kim, E.-J., Park, S. B. Preparation of $NaTaO_3$ by Spray Pyrolysis and Evaluation of Apparent Photocatalytic Activity for Hydrogen Production from Water. *Int. J. Photoenergy* **2008**, 1-8 (2008).

(97) Kang, H. W., Park, S. B. Water photolysis by $NaTaO_3$-C composite prepared by spray pyrolysis. *Adv. Powder Technol.* **21**, 106-110 (2010).

(98) Kang, H. W., Lim, S. N., Song, D., Park, S. B. Organic-inorganic composite of g-C$_3$N$_4$–SrTiO$_3$:Rh photocatalyst for improved H$_2$ evolution under visible light irradiation. *Int. J. Hydrogen Energy* **37**, 11602-11610 (2012).

(99) Kang, H. W., Lim, S. N., Park, S. B. Effect of tri-doping on H$_2$ evolution under visible light irradiation on SrTiO$_3$:Ni/Ta/La prepared by spray pyrolysis from polymeric precursor. *Int. J. Hydrogen Energy* **37**, 10539-10548 (2012).

(100) Kang, H. W., Park, S. B. Preparation of novel SrTiO$_3$:Rh/Ta photocatalyst by spray pyrolysis and its activity for H$_2$ evolution from aqueous methanol solution under visible light. *Int. J. Hydrogen Energy* **38**, 823-831 (2013).

(101) Kang, H. W., Park, S. B., Park, A.-H. A. Effects of charge balance with Na$^+$ on SrTiO$_3$:Mo^{6+} prepared by spray pyrolysis for H$_2$ evolution under visible light irradiation. *Int. J. Hydrogen Energy* **38**, 9198-9205 (2013).

(102) Kang, H. W., Park, S. B. Doping of fluorine into SrTiO$_3$ by spray pyrolysis for H$_2$ evolution under visible light irradiation. *Chem. Eng. Sci.* **100**, 384-391 (2013).

(103) Kang, H. W., Park, S. B. Effects of Mo sources on Mo doped SrTiO$_3$ powder prepared by spray pyrolysis for H$_2$ evolution under visible light irradiation. *Mater. Sci. Eng. B* **211**, 67-74 (2016).

(104) Jing, D., Guo, L., Zhao, L., Zhang, X., Liu, H., Li, M., Shen, S., Liu, G., Hu, X., Zhang, X. Efficient solar hydrogen production by photocatalytic water splitting: From fundamental study to pilot demonstration. *Int. J. Hydrogen Energy* **35**, 7087-7097 (2010).

(105) Xing, Z., Zong, X., Pan, J., Wang, L. On the engineering part of solar hydrogen production from water splitting: Photoreactor design. *Chem. Eng. Sci.* **104**, 125-146 (2013).

(106) Nguyen, V.-H., Wu, J. C. S. Recent developments in the design of photoreactors for solar energy conversion from water splitting and CO$_2$ reduction. *Appl. Catal., A* **550**, 122-141 (2018).

(107) Alsayegh, S., Johnson, J. R., Ohs, B., Lohaus, J., Wessling, M. Systematic optimization of H_2 recovery from water splitting process using membranes and N_2 diluent. *Int. J. Hydrogen Energy* **42**, 6000-6011 (2017).

(108) Alsayegh, S., Johnson, J. R., Wei, X., Ohs, B., Lohaus, J., Wessling, M. CO_2 aided H_2 recovery from water splitting processes. *Int. J. Hydrogen Energy* **42**, 21793-21805 (2017).

(109) Yu, S.-C., Huang, C.-W., Liao, C.-H., Wu, J. C. S., Chang, S.-T., Chen, K.-H. A novel membrane reactor for separating hydrogen and oxygen in photocatalytic water splitting. *J. Membr. Sci.* **382**, 291-299 (2011).

(110) Lo, C.-C., Huang, C.-W., Liao, C.-H., Wu, J. C. S. Novel twin reactor for separate evolution of hydrogen and oxygen in photocatalytic water splitting. *Int. J. Hydrogen Energy* **35**, 1523-1529 (2010).

(111) Sasaki, Y., Kato, H., Kudo, A. $[Co(bpy)_3]^{3+/2+}$ and $[Co(phen)_3]^{3+/2+}$ electron mediators for overall water splitting under sunlight irradiation using Z-scheme photocatalyst system. *J. Am. Chem. Soc.* **135**, 5441-9 (2013).

(112) Fabian, D. M., Hu, S., Singh, N., Houle, F. A., Hisatomi, T., Domen, K., Osterloh, F. E., Ardo, S. Particle suspension reactors and materials for solar-driven water splitting. *Energy Environ. Sci.* **8**, 2825-2850 (2015).

(113) Pinaud, B. A., Benck, J. D., Seitz, L. C., Forman, A. J., Chen, Z., Deutsch, T. G., James, B. D., Baum, K. N., Baum, G. N., Ardo, S., et al. Technical and economic feasibility of centralized facilities for solar hydrogen production via photocatalysis and photoelectrochemistry. *Energy Environ. Sci.* **6**, (2013).

(114) Schwarze, M., Stellmach, D., Schroder, M., Kailasam, K., Reske, R., Thomas, A., Schomacker, R. Quantification of photocatalytic hydrogen evolution. *Phys. Chem. Chem. Phys.* **15**, 3466-72 (2013).

(115) Skillen, N., Adams, M., McCullagh, C., Ryu, S. Y., Fina, F., Hoffmann, M. R., Irvine, J. T. S., Robertson, P. K. J. The application of a novel fluidised photo reactor under UV–Visible and natural solar irradiation in the photocatalytic generation of hydrogen. *Chem. Eng. J.* **286**, 610-621 (2016).

(116) Braham, R. J., Harris, A. T. Review of Major Design and Scale-up Considerations for Solar Photocatalytic Reactors. *Ind. Eng. Chem. Res.* **48**, 8890-8905 (2009).

(117) Huang, C., Yao, W., T-Raissi, A., Muradov, N. Development of efficient photoreactors for solar hydrogen production. *Sol. Energy* **85**, 19-27 (2011).

(118) Reilly, K., Fang, B., Taghipour, F., Wilkinson, D. P. Enhanced photocatalytic hydrogen production in a UV-irradiated fluidized bed reactor. *J. Catal.* **353**, 63-73 (2017).

(119) Reilly, K., Wilkinson, D. P., Taghipour, F. Photocatalytic water splitting in a fluidized bed system: Computational modeling and experimental studies. *Appl. Energy* **222**, 423-436 (2018).

(120) Ning, X., Zhen, W., Wu, Y., Lu, G. Inhibition of CdS photocorrosion by Al_2O_3 shell for highly stable photocatalytic overall water splitting under visible light irradiation. *Appl. Catal., B* **226**, 373-383 (2018).

(121) Vagia, E. C., Muradov, N., Kalyva, A., T-Raissi, A., Qin, N., Srinivasa, A. R., Kakosimos, K. E. Solar hybrid photo-thermochemical sulfur-ammonia water-splitting cycle: Photocatalytic hydrogen production stage. *Int. J. Hydrogen Energy* **42**, 20608-20624 (2017).

(122) Hisatomi, T., Domen, K. Reaction systems for solar hydrogen production via water splitting with particulate semiconductor photocatalysts. *Nat. Catal.* **2**, 387-399 (2019).

(123) Xiong, A., Ma, G., Maeda, K., Takata, T., Hisatomi, T., Setoyama, T., Kubota, J., Domen, K. Fabrication of photocatalyst panels and the factors determining their activity for water splitting. *Catal. Sci. Technol.* **4**, 325-328 (2014).

(124) Sutisna, Rokhmat, M., Wibowo, E., Khairurrijal, Abdullah, M. Prototype of a flat-panel photoreactor using TiO 2 nanoparticles coated on transparent granules for the degradation of Methylene Blue under solar illumination. *Sustainable Environ. Res.* **27**, 172-180 (2017).

(125) Spasiano, D., Marotta, R., Malato, S., Fernandez-Ibañez, P., Di Somma, I. Solar photocatalysis: Materials, reactors, some commercial, and pre-industrialized applications. A comprehensive approach. *Appl. Catal., B* **170-171**, 90-123 (2015).

(126) Fuqiang, W., Ziming, C., Jianyu, T., Yuan, Y., Yong, S., Linhua, L. Progress in concentrated solar power technology with parabolic trough collector system: A comprehensive review. *Renew. Sustain. Energy Rev.* **79**, 1314-1328 (2017).

(127) Yang, Y., Wei, Q., Hou, J., Liu, H., Zhao, L. Solar concentrator with uniform irradiance for particulate photocatalytic hydrogen production system. *Int. J. Hydrogen Energy* **41**, 16040-16047 (2016).

(128) Cao, F., Wei, Q., Liu, H., Lu, N., Zhao, L., Guo, L. Development of the direct solar photocatalytic water splitting system for hydrogen production in Northwest China: Design and evaluation of photoreactor. *Renew. Energy* **121**, 153-163 (2018).

(129) Otálvaro-Marín, H. L., Mueses, M. A., Crittenden, J. C., Machuca-Martinez, F. Solar photoreactor design by the photon path length and optimization of the radiant field in a TiO_2 -based CPC reactor. *Chem. Eng. J.* **315**, 283-295 (2017).

(130) Yang, Y., Wei, Q., Liu, H., Zhao, L. Optimization of the radiation absorption for a scaled-up photocatalytic hydrogen production system. *Sol. Energy* **160**, 168-177 (2018).

(131) Ren, Y., Zhao, L., Jing, D., Guo, L. Investigation and modeling of CPC based tubular photocatalytic reactor for scaled-up hydrogen production. *Int. J. Hydrogen Energy* **41**, 16019-16031 (2016).

(132) Jing, D., Liu, H., Zhang, X., Zhao, L., Guo, L. Photocatalytic hydrogen production under direct solar light in a CPC based solar reactor: Reactor design and preliminary results. *Energy Conv. Manage.* **50**, 2919-2926 (2009).

**The earliest pilot plant for photocatalytic hydrogen generation with illuminated area exceeding 1 m². **

(133) Cao, F., Liu, H., Wei, Q., Zhao, L., Guo, L. Experimental study of direct solar photocatalytic water splitting for hydrogen production under natural circulation conditions. *Int. J. Hydrogen Energy* **43**, 13727-13737 (2018).

(134) Wei, Q., Yang, Y., Hou, J., Liu, H., Cao, F., Zhao, L. Direct solar photocatalytic hydrogen generation with CPC photoreactors: System development. *Sol. Energy* **153**, 215-223 (2017).

The largest photocatalytic hydrogen generation system (with sacrificial electron donor) reported so far.

(135) Wei, Q., Yang, Y., Liu, H., Hou, J., Liu, M., Cao, F., Zhao, L. Experimental study on direct solar photocatalytic water splitting for hydrogen production using surface uniform concentrators. *Int. J. Hydrogen Energy* **43**, 13745-13753 (2018).

(136) Villa, K., Domènech, X., Malato, S., Maldonado, M. I., Peral, J. Heterogeneous photocatalytic hydrogen generation in a solar pilot plant. *Int. J. Hydrogen Energy* **38**, 12718-12724 (2013).

(137) Arzate Salgado, S. Y., Ramírez Zamora, R. M., Zanella, R., Peral, J., Malato, S., Maldonado, M. I. Photocatalytic hydrogen production in a solar pilot plant using a Au/TiO$_2$ photo catalyst. *Int. J. Hydrogen Energy* **41**, 11933-11940 (2016).

(138) Maldonado, M. I., López-Martín, A., Colón, G., Peral, J., Martínez-Costa, J. I., Malato, S. Solar pilot plant scale hydrogen generation by irradiation of Cu/TiO$_2$ composites in presence of sacrificial electron donors. *Appl. Catal., B* **229**, 15-23 (2018).

(139) Schröder, M., Kailasam, K., Rudi, S., Fündling, K., Rieß, J., Lublow, M., Thomas, A., Schomäcker, R., Schwarze, M. Applying thermo-destabilization of microemulsions as a new method for co-catalyst loading on mesoporous polymeric carbon nitride – towards large scale applications. *RSC Adv.* **4**, 50017-50026 (2014).

(140) Schröder, M., Kailasam, K., Borgmeyer, J., Neumann, M., Thomas, A., Schomäcker, R., Schwarze, M. Hydrogen Evolution Reaction in a Large-Scale Reactor using a Carbon Nitride Photocatalyst under Natural Sunlight Irradiation. *Energy Technol.* **3**, 1014-1017 (2015).

(141) Goto, Y., Hisatomi, T., Wang, Q., Higashi, T., Ishikiriyama, K., Maeda, T., Sakata, Y., Okunaka, S., Tokudome, H., Katayama, M., et al. A Particulate Photocatalyst Water-Splitting Panel for Large-Scale Solar Hydrogen Generation. *Joule* **2**, 509-520 (2018).

The largest photocatalytic pure water splitting system reported so far.

(142) Wang, Q., Hisatomi, T., Jia, Q., Tokudome, H., Zhong, M., Wang, C., Pan, Z., Takata, T., Nakabayashi, M., Shibata, N., et al. Scalable water splitting on particulate photocatalyst sheets with a solar-to-hydrogen energy conversion efficiency exceeding 1. *Nat. Mater.* **15**, 611-5 (2016).

(143) Wang, Q., Okunaka, S., Tokudome, H., Hisatomi, T., Nakabayashi, M., Shibata, N., Yamada, T., Domen, K. Printable Photocatalyst Sheets Incorporating a Transparent Conductive Mediator for Z-Scheme Water Splitting. *Joule* **2**, 2667-2680 (2018).

(144) Priya, R., Kanmani, S. Design of pilot-scale solar photocatalytic reactor for the generation of hydrogen from alkaline sulfide wastewater of sewage treatment plant. *Environ. Technol.* **34**, 2817-23 (2013).

(145) Rodriguez, J., Puzenat, E., Thivel, P. X. From solar photocatalysis to fuel-cell: A hydrogen supply chain. *J. Environ. Chem. Eng.* **4**, 3001-3005 (2016).

(146) Gaffron, H., Rubin, J. Fermentative and Photochemical Production of Hydrogen in Algae. *J. Gen. Physiol.* **26**, 219-240 (1942).

(147) Ghirardi, M. L., Dubini, A., Yu, J., Maness, P. C. Photobiological hydrogen-producing systems. *Chem. Soc. Rev.* **38**, 52-61 (2009).

(148) Khetkorn, W., Rastogi, R. P., Incharoensakdi, A., Lindblad, P., Madamwar, D., Pandey, A., Larroche, C. Microalgal hydrogen production - A review. *Bioresour. Technol.* **243**, 1194-1206 (2017).

(149) Haumann, M., Stripp, S. T. The Molecular Proceedings of Biological Hydrogen Turnover. *Acc. Chem. Res.* **51**, 1755-1763 (2018).

(150) Ghirardi, M. L., Posewitz, M. C., Maness, P. C., Dubini, A., Yu, J., Seibert, M. Hydrogenases and hydrogen photoproduction in oxygenic photosynthetic organisms. *Annu. Rev. Plant Biol.* **58**, 71-91 (2007).

(151) Photobiological Production of Hydrogen *National Renewable Energy Laboratory* [Online], 2007. https://www.nrel.gov/docs/fy08osti/42285.pdf.

(152) Ghirardi, M. L. Implementation of photobiological H_2 production: the O_2 sensitivity of hydrogenases. *Photosynth. Res.* **125**, 383-93 (2015).

(153) Hallenbeck, P. Biological hydrogen production; fundamentals and limiting processes. *Int. J. Hydrogen Energy* **27**, 1185-1193 (2002).

(154) Melis, A. Solar energy conversion efficiencies in photosynthesis: Minimizing the chlorophyll antennae to maximize efficiency. *Plant Sci.* **177**, 272-280 (2009).

(155) Nagarajan, D., Lee, D. J., Kondo, A., Chang, J. S. Recent insights into biohydrogen production by microalgae - From biophotolysis to dark fermentation. *Bioresour. Technol.*, (2016).

(156) Greenbaum, E. Energetic Efficiency of Hydrogen Photoevolution by Algal Water Splitting. *Biophys. J.* **54**, 365-368 (1988).

(157) Eroglu, E., Melis, A. Photobiological hydrogen production: Recent advances and state of the art. *Bioresour. Technol.* **102**, 8403-13 (2011).

(158) Budiman, P. M., Wu, T. Y. Role of chemicals addition in affecting biohydrogen production through photofermentation. *Energy Conv. Manage.* **165**, 509-527 (2018).

(159) Adessi, A., De Philippis, R. Photobioreactor design and illumination systems for H_2 production with anoxygenic photosynthetic bacteria: A review. *Int. J. Hydrogen Energy* **39**, 3127-3141 (2014).

(160) Hallenbeck, P. C., Liu, Y. Recent advances in hydrogen production by photosynthetic bacteria. *Int. J. Hydrogen Energy* **41**, 4446-4454 (2016).

(161) Trchounian, K., Sawers, R. G., Trchounian, A. Improving biohydrogen productivity by microbial dark- and photo-fermentations: Novel data and future approaches. *Renew. Sustain. Energy Rev.* **80**, 1201-1216 (2017).

(162) Show, K. Y., Yan, Y., Ling, M., Ye, G., Li, T., Lee, D. J. Hydrogen production from algal biomass - Advances, challenges and prospects. *Bioresour. Technol.* **257**, 290-300 (2018).

(163) Zhang, Z., Zhou, X., Hu, J., Zhang, T., Zhu, S., Zhang, Q. Photo-bioreactor structure and light-heat-mass transfer properties in photo-fermentative bio-hydrogen production system: A mini review. *Int. J. Hydrogen Energy* **42**, 12143-12152 (2017).

(164) Maness, P.-C., Yu, J., Eckert, C., Ghirardi, M. L. Photobiological Hydrogen Production - Prospects and Challenges. *Microbe* **4**, 275-280 (2009).

(165) Basak, N., Jana, A. K., Das, D., Saikia, D. Photofermentative molecular biohydrogen production by purple-non-sulfur (PNS) bacteria in various modes: The present progress and future perspective. *Int. J. Hydrogen Energy* **39**, 6853-6871 (2014).

(166) Ghosh, S., Dairkee, U. K., Chowdhury, R., Bhattacharya, P. Hydrogen from food processing wastes via photofermentation using Purple Non-sulfur Bacteria (PNSB) – A review. *Energy Conv. Manage.* **141**, 299-314 (2017).

(167) Keskin, T., Abo-Hashesh, M., Hallenbeck, P. C. Photofermentative hydrogen production from wastes. *Bioresour. Technol.* **102**, 8557-68 (2011).

(168) Zhang, Q., Wang, Y., Zhang, Z., Lee, D. J., Zhou, X., Jing, Y., Ge, X., Jiang, D., Hu, J., He, C. Photo-fermentative hydrogen production from crop residue: A mini review. *Bioresour. Technol.* **229**, 222-230 (2017).

(169) Dinesh, G. K., Chauhan, R., Chakma, S. Influence and strategies for enhanced biohydrogen production from food waste. *Renew. Sustain. Energy Rev.* **92**, 807-822 (2018).

(170) Sagir, E., Alipour, S., Elkahlout, K., Koku, H., Gunduz, U., Eroglu, I., Yucel, M. Biological hydrogen production from sugar beet molasses by agar immobilized R. capsulatus in a panel photobioreactor. *Int. J. Hydrogen Energy* **43**, 14987-14995 (2018).

(171) Savasturk, D., Kayahan, E., Koku, H. Photofermentative hydrogen production from molasses: Scale-up and outdoor operation at low carbon-to-nitrogen ratio. *Int. J. Hydrogen Energy* **43**, 11676-11687 (2018).

(172) Lu, C., Zhang, Z., Zhou, X., Hu, J., Ge, X., Xia, C., Zhao, J., Wang, Y., Jing, Y., Li, Y., et al. Effect of substrate concentration on hydrogen production by photo-fermentation in the pilot-scale baffled bioreactor. *Bioresour. Technol.* **247**, 1173-1176 (2018).

(173) Kayahan, E., Eroglu, I., Koku, H. A compact tubular photobioreactor for outdoor hydrogen production from molasses. *Int. J. Hydrogen Energy* **42**, 2575-2582 (2017).

(174) Sagir, E., Alipour, S., Elkahlout, K., Koku, H., Gunduz, U., Eroglu, I., Yucel, M. Scale-up studies for stable, long-term indoor and outdoor production of hydrogen by immobilized Rhodobacter capsulatus. *Int. J. Hydrogen Energy* **42**, 22743-22755 (2017).

(175) Zhang, Q., Lu, C., Lee, D. J., Lee, Y. J., Zhang, Z., Zhou, X., Hu, J., Wang, Y., Jiang, D., He, C., et al. Photo-fermentative hydrogen production in a 4 m^3 baffled reactor: Effects of hydraulic retention time. *Bioresour. Technol.* **239**, 533-537 (2017).

(176) Zhang, Q., Zhang, Z., Wang, Y., Lee, D. J., Li, G., Zhou, X., Jiang, D., Xu, B., Lu, C., Li, Y., et al. Sequential dark and photo fermentation hydrogen production from hydrolyzed corn stover: A pilot test using 11 m^3 reactor. *Bioresour. Technol.* **253**, 382-386 (2018).

The largest photofermentative hydrogen generation system reported so far.
(177) Tian, Y., Zhao, C. Y. A review of solar collectors and thermal energy storage in solar thermal applications. *Appl. Energy* **104**, 538-553 (2013).

(178) Behar, O., Khellaf, A., Mohammedi, K. A review of studies on central receiver solar thermal power plants. *Renew. Sustain. Energy Rev.* **23**, 12-39 (2013).

(179) Kalogirou, S. A. Solar thermal collectors and applications. *Prog. Energy Combust. Sci.* **30**, 231-295 (2004).

(180) Ho, C. K., Iverson, B. D. Review of high-temperature central receiver designs for concentrating solar power. *Renew. Sustain. Energy Rev.* **29**, 835-846 (2014).

(181) Avila-Marin, A. L. Volumetric receivers in Solar Thermal Power Plants with Central Receiver System technology: A review. *Sol. Energy* **85**, 891-910 (2011).

(182) Reddy, V. S., Kaushik, S. C., Ranjan, K. R., Tyagi, S. K. State-of-the-art of solar thermal power plants-A review. *Renew. Sustain. Energy Rev.* **27**, 258-273 (2013).

(183) Fletcher, E. A. Solarthermal processing: A review. *J. Sol. Energy Eng.* **123**, 63-74 (2001).

(184) Muhich, C. L., Ehrhart, B. D., Al-Shankiti, I., Ward, B. J., Musgrave, C. B., Weimer, A. W. A review and perspective of efficient hydrogen generation via solar thermal water splitting. *WIREs Energy Environ.* **5**, 261-287 (2016).

(185) Rao, C., Dey, S. Solar thermochemical splitting of water to generate hydrogen. *Proc. Natl. Acad. Sci. USA* **114**, 13385-13393 (2017).

(186) Kodama, T., Gokon, N. Thermochemical Cycles for High-Temperature Solar Hydrogen Production. *Chem. Rev.* **107**, 4048-4077 (2007).

(187) Xu, B., Bhawe, Y., Davis, M. E. Low-temperature, manganese oxide-based, thermochemical water splitting cycle. *Proc. Natl. Acad. Sci. USA* **109**, 9260-9264 (2012).

(188) Dey, S., Rajesh, S., Rao, C. N. R. Significant reduction in the operating temperature of the Mn(II)/Mn(III) oxide-based thermochemical water splitting cycle brought about by the use of nanoparticles. *J. Mater. Chem. A* **4**, 16830-16833 (2016).

(189) Steinfeld, A. Solar thermochemical production of hydrogen—a review. *Sol. Energy* **78**, 603-615 (2005).

(190) Perkins, C., Weimer, A. W. Likely near-term solar-thermal water splitting technologies. *Int. J. Hydrogen Energy* **29**, 1587-1599 (2004).

(191) Meredig, B., Wolverton, C. First-principles thermodynamic framework for the evaluation of thermochemical H_2O- or CO_2-splitting materials. *Phys. Rev. B* **80**, 245119 (2009).

(192) Schulz, H., Nie, Z. Q., Ousmanov, F. Construction of the Fischer-Tropsch regime with cobalt catalysts. *Catal. Today* **71**, 351-360 (2002).

(193) Riedel, T., Schaub, G. Low-temperature Fischer-Tropsch synthesis on cobalt catalysts - effects of CO2. *Top Catal.* **26**, 145-156 (2003).

(194) Scheffe, J. R., Steinfeld, A. Oxygen exchange materials for solar thermochemical splitting of H_2O and CO_2: a review. *Mater. Today* **17**, 341-348 (2014).

(195) Steinfeld, A. Solar hydrogen production via a two-step water-splitting thermochemical cycle based on Zn/ZnO redox reactions. *Int. J. Hydrogen Energy* **27**, 611-619 (2002).

(196) Perkins, C., Lichty, P. R., Weimer, A. W. Thermal ZnO dissociation in a rapid aerosol reactor as part of a solar hydrogen production cycle. *Int. J. Hydrogen Energy* **33**, 499-510 (2008).

(197) Loutzenhiser, P. G., Meier, A., Steinfeld, A. Review of the Two-Step H_2O/CO_2-Splitting Solar Thermochemical Cycle Based on Zn/ZnO Redox Reactions. *Materials* **3**, 4922-4938 (2010).

(198) Abanades, S., Charvin, P., Lemont, F., Flamant, G. Novel two-step SnO_2/SnO water-splitting cycle for solar thermochemical production of hydrogen. *Int. J. Hydrogen Energy* **33**, 6021-6030 (2008).

(199) Nakamura, T. Hydrogen production from water utilizing solar heat at high temperatures. *Sol. Energy* **19**, 467-475 (1977).

(200) Coker, E. N., Ambrosini, A., Rodriguez, M. A., Miller, J. E. Ferrite-YSZ composites for solar thermochemical production of synthetic fuels: in operando characterization of CO_2 reduction. *J. Mater. Chem.* **21**, 10767-10776 (2011).

(201) Charvin, P., Abanades, S., Flamant, G., Lemort, F. Two-step water splitting thermochemical cycle based on iron oxide redox pair for solar hydrogen production. *Energy* **32**, 1124-1133 (2007).

(202) Kodama, T., Nakamuro, Y., Mizuno, T. A Two-Step Thermochemical Water Splitting by Iron-Oxide on Stabilized Zirconia. *J. Sol. Energy Eng.* **128**, 3-7 (2004).

(203) Gokon, N., Murayama, H., Umeda, J., Hatamachi, T., Kodama, T. Monoclinic zirconia-supported Fe_3O_4 for the two-step water-splitting thermochemical cycle at high thermal reduction temperatures of 1400–1600°C. *Int. J. Hydrogen Energy* **34**, 1208-1217 (2009).

(204) Abanades, S., Villafan-Vidales, H. I. CO_2 and H_2O conversion to solar fuels via two-step solar thermochemical looping using iron oxide redox pair. *Chem. Eng. J.* **175**, 368-375 (2011).

(205) Kodama, T., Kondoh, Y., Yamamoto, R., Andou, H., Satou, N. Thermochemical hydrogen production by a redox system of ZrO_2-supported Co(II)-ferrite. *Solar Energy* **78**, 623-631 (2005).

(206) Scheffe, J. R., McDaniel, A. H., Allendorf, M. D., Weimer, A. W. Kinetics and mechanism of solar-thermochemical H_2 production by oxidation of a cobalt ferrite–zirconia composite. *Energy Environ. Sci.* **6**, 963-973 (2013).

(207) Allendorf, M. D., Diver, R. B., Siegel, N. P., Miller, J. E. Two-Step Water Splitting Using Mixed-Metal Ferrites: Thermodynamic Analysis and Characterization of Synthesized Materials. *Energy Fuels* **22**, 4115-4124 (2008).

(208) Scheffe, J. R., Li, J., Weimer, A. W. A spinel ferrite/hercynite water-splitting redox cycle. *Int. J. Hydrogen Energy* **35**, 3333-3340 (2010).

(209) Arifin, D., Aston, V. J., Liang, X., McDaniel, A. H., Weimer, A. W. $CoFe_2O_4$ on a porous Al_2O_3 nanostructure for solar thermochemical CO_2 splitting. *Energy Environ. Sci.* **5**, 9438-9443 (2012).

(210) Muhich, C. L., Evanko, B. W., Weston, K. C., Lichty, P., Liang, X., Martinek, J., Musgrave, C. B., Weimer, A. W. Efficient Generation of H_2 by Splitting Water with an Isothermal Redox Cycle. *Science* **341**, 540-542 (2013).

(211) Chueh, W. C., Falter, C., Abbott, M., Scipio, D., Furler, P., Haile, S. M., Steinfeld, A. High-Flux Solar-Driven Thermochemical Dissociation of CO_2 and H_2O Using Nonstoichiometric Ceria. *Science* **330**, 1797-1801 (2010).

(212) Chueh, W. C., Haile, S. M. A thermochemical study of ceria: exploiting an old material for new modes of energy conversion and CO_2 mitigation. *Philos. Trans. R. Soc. A* **368**, 3269-3294 (2010).

(213) Hao, Y., Yang, C.-K., Haile, S. M. High-temperature isothermal chemical cycling for solar-driven fuel production. *Phys. Chem. Chem. Phys.* **15**, 17084-17092 (2013).

(214) Furler, P., Scheffe, J. R., Steinfeld, A. Syngas production by simultaneous splitting of H_2O and CO_2 via ceria redox reactions in a high-temperature solar reactor. *Energy Environ. Sci.* **5**, 6098-6103 (2012).

(215) Furler, P., Scheffe, J., Gorbar, M., Moes, L., Vogt, U., Steinfeld, A. Solar Thermochemical CO_2 Splitting Utilizing a Reticulated Porous Ceria Redox System. *Energy Fuels* **26**, 7051-7059 (2012).

(216) Abanades, S., Legal, A., Cordier, A., Peraudeau, G., Flamant, G., Julbe, A. Investigation of reactive cerium-based oxides for H_2 production by thermochemical two-step water-splitting. *J. Mater. Sci.* **45**, 4163-4173 (2010).

(217) Le Gal, A., Abanades, S., Bion, N., Le Mercier, T., Harlé, V. Reactivity of Doped Ceria-Based Mixed Oxides for Solar Thermochemical Hydrogen Generation via Two-Step Water-Splitting Cycles. *Energy Fuels* **27**, 6068-6078 (2013).

(218) Meng, Q.-L., Lee, C.-i., Ishihara, T., Kaneko, H., Tamaura, Y. Reactivity of CeO_2-based ceramics for solar hydrogen production via a two-step water-splitting cycle with concentrated solar energy. *Int. J. Hydrogen Energy* **36**, 13435-13441 (2011).

(219) Scheffe, J. R., Weibel, D., Steinfeld, A. Lanthanum–Strontium–Manganese Perovskites as Redox Materials for Solar Thermochemical Splitting of H_2O and CO_2. *Energy Fuels* **27**, 4250-4257 (2013).

(220) McDaniel, A. H., Miller, E. C., Arifin, D., Ambrosini, A., Coker, E. N., O'Hayre, R., Chueh, W. C., Tong, J. Sr- and Mn-doped $LaAlO_{3-\delta}$ for solar thermochemical H_2 and CO production. *Energy Environ. Sci.* **6**, 2424-2428 (2013).

(221) Marxer, D., Furler, P., Scheffe, J., Geerlings, H., Falter, C., Batteiger, V., Sizmann, A., Steinfeld, A. Demonstration of the Entire Production Chain to Renewable Kerosene via Solar Thermochemical Splitting of H_2O and CO_2. *Energy Fuels* **29**, 3241-3250 (2015).

Solar thermal production of 700 liters of syngas with STH efficiency of 1.72%.
(222) Bhosale, R. R., Takalkar, G., Sutar, P., Kumar, A., AlMomani, F., Khraisheh, M. A decade of ceria based solar thermochemical H_2O/CO_2 splitting cycle. *Int. J. Hydrogen Energy* **44**, 34-60 (2019).

(223) Voitic, G., Hacker, V. Recent advancements in chemical looping water splitting for the production of hydrogen. *Rsc Adv.* **6**, 98267-98296 (2016).

(224) Luo, M., Yi, Y., Wang, S. Z., Wang, Z. L., Du, M., Pan, J. F., Wang, Q. Review of hydrogen production using chemical-looping technology. *Renewable Sustainable Energy Rev.* **81**, 3186-3214 (2018).

(225) Fujishima, A., Honda, K. Electrochemical Photolysis of Water at a Semiconductor Electrode. *Nature* **238**, 37-38 (1972).

(226) McKone, J. R., Lewis, N. S., Gray, H. B. Will Solar-Driven Water-Splitting Devices See the Light of Day? *Chem. Mater.* **26**, 407-414 (2014).

(227) Rocheleau, R. E., Miller, E. L., Misra, A. High-efficiency photoelectrochemical hydrogen production using multijunction amorphous silicon photoelectrodes. *Energy Fuels* **12**, 3-10 (1998).

(228) Reece, S. Y., Hamel, J. A., Sung, K., Jarvi, T. D., Esswein, A. J., Pijpers, J. J. H., Nocera, D. G. Wireless Solar Water Splitting Using Silicon-Based Semiconductors and Earth-Abundant Catalysts. *Science* **334**, 645-648 (2011).

(229) Okamoto, S., Deguchi, M., Yotsuhashi, S. Modulated III–V Triple-Junction Solar Cell Wireless Device for Efficient Water Splitting. *J. Phys. Chem. C* **121**, 1393-1398 (2017).

(230) Verlage, E., Hu, S., Liu, R., Jones, R. J. R., Sun, K., Xiang, C. X., Lewis, N. S., Atwater, H. A. A monolithically integrated, intrinsically safe, 10% efficient, solar-driven water-splitting system based on active, stable earth-abundant electrocatalysts in conjunction with tandem III-V light absorbers protected by amorphous TiO_2 films. *Energy Environ. Sci.* **8**, 3166-3172 (2015).

(231) Chen, Y. S., Manser, J. S., Kamat, P. V. All Solution-Processed Lead Halide Perovskite-$BiVO_4$ Tandem Assembly for Photolytic Solar Fuels Production. *J. Am. Chem. Soc.* **137**, 974-981 (2015).

(232) Gurudayal, Sabba, D., Kumar, M. H., Wong, L. H., Barber, J., Gratzel, M., Mathews, N. Perovskite-Hematite Tandem Cells for Efficient Overall Solar Driven Water Splitting. *Nano Lett.* **15**, 3833-3839 (2015).

(233) Kim, J. H., Jo, Y., Kim, J. H., Jang, J. W., Kang, H. J., Lee, Y. H., Kim, D. S., Jun, Y., Lee, J. S. Wireless Solar Water Splitting Device with Robust Cobalt-Catalyzed, Dual-Doped $BiVO_4$

Photoanode and Perovskite Solar Cell in Tandem: A Dual Absorber Artificial Leaf. *Acs Nano* **9**, 11820-11829 (2015).

(234) Young, J. L., Steiner, M. A., Doscher, H., France, R. M., Turner, J. A., Deutsch, T. G. Direct solar-to-hydrogen conversion via inverted metamorphic multi-junction semiconductor architectures. *Nat. Energy* **2**, 17028 (2017).

(235) Cheng, W. H., Richter, M. H., May, M. M., Ohlmann, J., Lackner, D., Dimroth, F., Hannappel, T., Atwater, H. A., Lewerenz, H. J. Monolithic Photoelectrochemical Device for Direct Water Splitting with 19% Efficiency. *ACS Energy Lett.* **3**, 1795-1800 (2018).

(236) Nocera, D. G. The Artificial Leaf. *Acc. Chem. Res.* **45**, 767-776 (2012).

(237) Joya, K. S., Joya, Y. F., Ocakoglu, K., van de Krol, R. Water-Splitting Catalysis and Solar Fuel Devices: Artificial Leaves on the Move. *Angew. Chem. Int. Ed.* **52**, 10426-10437 (2013).

(238) Khaselev, O., Turner, J. A. A monolithic photovoltaic-photoelectrochemical device for hydrogen production via water splitting. *Science* **280**, 425-427 (1998).

(239) Turan, B., Becker, J. P., Urbain, F., Finger, F., Rau, U., Haas, S. Upscaling of integrated photoelectrochemical water-splitting devices to large areas. *Nat. Commun.* **7**, (2016).

(240) Walter, M. G., Warren, E. L., McKone, J. R., Boettcher, S. W., Mi, Q. X., Santori, E. A., Lewis, N. S. Solar Water Splitting Cells. *Chem. Rev.* **110**, 6446-6473 (2010).

(241) Kornienko, N., Gibson, N. A., Zhang, H., Eaton, S. W., Yu, Y., Aloni, S., Leone, S. R., Yang, P. D. Growth and Photoelectrochemical Energy Conversion of Wurtzite Indium Phosphide Nanowire Arrays. *Acs Nano* **10**, 5525-5535 (2016).

(242) Kim, J. H., Kaneko, H., Minegishi, T., Kubota, J., Domen, K., Lee, J. S. Overall Photoelectrochemical Water Splitting using Tandem Cell under Simulated Sunlight. *Chemsuschem* **9**, 61-66 (2016).

(243) Yang, H. B., Miao, J. W., Hung, S. F., Huo, F. W., Chen, H. M., Liu, B. Stable Quantum Dot Photoelectrolysis Cell for Unassisted Visible Light Solar Water Splitting. *Acs Nano* **8**, 10403-10413 (2014).

(244) Jia, Q. X., Iwashina, K., Kudo, A. Facile fabrication of an efficient $BiVO_4$ thin film electrode for water splitting under visible light irradiation. *Proc. Natl. Acad. Sci. USA* **109**, 11564-11569 (2012).

(245) Pareek, A., Dom, R., Borse, P. H. Fabrication of large area nanorod like structured CdS photoanode for solar H_2 generation using spray pyrolysis technique. *Int. J. Hydrogen Energy* **38**, 36-44 (2013).

(246) Dilger, S., Trottmann, M., Pokrant, S. Scaling up electrodes for photoelectrochemical water splitting: fabrication process and performance of 40 cm^2 $LaTiO_2N$ photoanodes. *Chemsuschem*, (2019).

(247) Sivula, K., Le Formal, F., Gratzel, M. Solar Water Splitting: Progress Using Hematite (α-Fe_2O_3) Photoelectrodes. *Chemsuschem* **4**, 432-449 (2011).

(248) Dias, P., Vilanova, A., Lopes, T., Andrade, L., Mendes, A. Extremely stable bare hematite photoanode for solar water splitting. *Nano Energy* **23**, 70-79 (2016).

(249) Tamirat, A. G., Rick, J., Dubale, A. A., Su, W. N., Hwang, B. J. Using hematite for photoelectrochemical water splitting: a review of current progress and challenges. *Nanoscale Horiz.* **1**, 243-267 (2016).

(250) Jeon, T. H., Moon, G. H., Park, H., Choi, W. Ultra-efficient and durable photoelectrochemical water oxidation using elaborately designed hematite nanorod arrays. *Nano Energy* **39**, 211-218 (2017).

(251) Peerakiatkhajohn, P., Yun, J. H., Chen, H. J., Lyu, M. Q., Butburee, T., Wang, L. Z. Stable Hematite Nanosheet Photoanodes for Enhanced Photoelectrochemical Water Splitting. *Adv. Mater.* **28**, 6405-6410 (2016).

(252) Kim, J. Y., Magesh, G., Youn, D. H., Jang, J. W., Kubota, J., Domen, K., Lee, J. S. Single-crystalline, wormlike hematite photoanodes for efficient solar water splitting. *Sci. Rep.* **3**, (2013).

(253) Lopes, T., Dias, P., Andrade, L., Mendes, A. An innovative photoelectrochemical lab device for solar water splitting. *Sol. Energy Mater. Sol. Cells* **128**, 399-410 (2014).

(254) Hankin, A., Bedoya-Lora, F. E., Ong, C. K., Alexander, J. C., Petter, F., Kelsall, G. H. From millimetres to metres: the critical role of current density distributions in photo-electrochemical reactor design. *Energy Environ. Sci.* **10**, 346-360 (2017).

(255) Vilanova, A., Lopes, T., Mendes, A. Large-area photoelectrochemical water splitting using a multi-photoelectrode approach. *J. Power Sources* **398**, 224-232 (2018).

(256) Segev, G., Dotan, H., Malviya, K. D., Kay, A., Mayer, M. T., Grätzel, M., Rothschild, A. High Solar Flux Concentration Water Splitting with Hematite (α-Fe_2O_3) Photoanodes. *Adv. Energy Mater.* **6**, 1500817 (2016).

(257) Pihosh, Y., Turkevych, I., Mawatari, K., Uemura, J., Kazoe, Y., Kosar, S., Makita, K., Sugaya, T., Matsui, T., Fujita, D., et al. Photocatalytic generation of hydrogen by core-shell WO_3/$BiVO_4$ nanorods with ultimate water splitting efficiency. *Sci. Rep.* **5**, (2015).

(258) Shi, X. J., Choi, Y., Zhang, K., Kwon, J., Kim, D. Y., Lee, J. K., Oh, S. H., Kim, J. K., Park, J. H. Efficient photoelectrochemical hydrogen production from bismuth vanadate-decorated tungsten trioxide helix nanostructures. *Nat. Commun.* **5**, 4775 (2014).

(259) Lee, D. K., Choi, K. S. Enhancing long-term photostability of $BiVO_4$ photoanodes for solar water splitting by tuning electrolyte composition. *Nat. Energy* **3**, 53-60 (2018).

(260) Kuang, Y., Jia, Q., Ma, G., Hisatomi, T., Minegishi, T., Nishiyama, H., Nakabayashi, M., Shibata, N., Yamada, T., Kudo, A., et al. Ultrastable low-bias water splitting photoanodes via photocorrosion inhibition and in situ catalyst regeneration. *Nat. Energy* **2**, 16191 (2016).

(261) Yao, X., Wang, D. P., Zhao, X., Ma, S. S., Bassi, P. S., Yang, G., Chen, W., Chen, Z., Sritharan, T. Scale-Up of $BiVO_4$ Photoanode for Water Splitting in a Photoelectrochemical Cell: Issues and Challenges. *Energy Technol.* **6**, 100-109 (2018).

(262) Paracchino, A., Laporte, V., Sivula, K., Gratzel, M., Thimsen, E. Highly active oxide photocathode for photoelectrochemical water reduction. *Nat. Mater.* **10**, 456-461 (2011).

(263) Luo, J. S., Steier, L., Son, M. K., Schreier, M., Mayer, M. T., Gratzel, M. Cu_2O Nanowire Photocathodes for Efficient and Durable Solar Water Splitting. *Nano Lett.* **16**, 1848-1857 (2016).

(264) Pan, L. F., Kim, J. H., Mayer, M. T., Son, M. K., Ummadisingu, A., Lee, J. S., Hagfeldt, A., Luo, J. S., Gratzel, M. Boosting the performance of Cu_2O photocathodes for unassisted solar water splitting devices. *Nat. Catal.* **1**, 412-420 (2018).

(265) Wang, J., Yu, N. F., Zhang, Y., Zhu, Y. S., Fu, L. J., Zhang, P., Gao, L., Wu, Y. P. Synthesis and performance of Cu_2ZnSnS_4 semiconductor as photocathode for solar water splitting. *J. Alloys Compd.* **688**, 923-932 (2016).

(266) Chen, Y. B., Feng, X. Y., Liu, M. C., Su, J. Z., Shen, S. H. Towards eflcient solar-to-hydrogen conversion: Fundamentals and recent progress in copper-based chalcogenide photocathodes. *Nanophotonics-Berlin* **5**, 524-547 (2016).

(267) Mali, M. G., Yoon, H., Joshi, B. N., Park, H., Al-Deyab, S. S., Lim, D. C., Ahn, S., Nervi, C., Yoon, S. S. Enhanced Photoelectrochemical Solar Water Splitting Using a Platinum-Decorated CIGS/CdS/ZnO Photocathode. *ACS Appl. Mater. Interfaces* **7**, 21619-21625 (2015).

(268) Kumagai, H., Minegishi, T., Sato, N., Yamada, T., Kubota, J., Domen, K. Efficient solar hydrogen production from neutral electrolytes using surface-modified $Cu(In,Ga)Se_2$ photocathodes. *J. Mater. Chem. A* **3**, 8300-8307 (2015).

(269) Jiang, F., Gunawan, Harada, T., Kuang, Y. B., Minegishi, T., Domen, K., Ikeda, S. $Pt/In_2S_3/CdS/Cu_2ZnSnS_4$ Thin Film as an Efficient and Stable Photocathode for Water Reduction under Sunlight Radiation. *J. Am. Chem. Soc.* **137**, 13691-13697 (2015).

(270) Sim, Y., John, J., Surendran, S., Moon, B., Sim, U. Efficient Photoelectrochemical Water Splitting Reaction using Electrodeposited Co_3Se_4 Catalyst. *Appl. Sci.* **9**, 16-27 (2018).

(271) Sim, Y., John, J., Moon, J., Sim, U. Photo-Assisted Hydrogen Evolution with Reduced Graphene Oxide Catalyst on Silicon Nanowire Photocathode. *Appl. Sci.* **8**, 2046-2057 (2018).

(272) Boettcher, S. W., Warren, E. L., Putnam, M. C., Santori, E. A., Turner-Evans, D., Kelzenberg, M. D., Walter, M. G., McKone, J. R., Brunschwig, B. S., Atwater, H. A., et al. Photoelectrochemical Hydrogen Evolution Using Si Microwire Arrays. *J. Am. Chem. Soc.* **133**, 1216-1219 (2011).

(273) Warren, E. L., McKone, J. R., Atwater, H. A., Gray, H. B., Lewis, N. S. Hydrogen-evolution characteristics of Ni-Mo-coated, radial junction, n$^+$p-silicon microwire array photocathodes. *Energy Environ. Sci.* **5**, 9653-9661 (2012).

(274) Wan, Y. M., Karuturi, S. K., Samundsett, C., Bullock, J., Hettick, M., Yan, D., Peng, J., Narangari, P. R., Mokkapati, S., Tan, H. H., et al. Tantalum Oxide Electron-Selective Heterocontacts for Silicon Photovoltaics and Photoelectrochemical Water Reduction. *Acs Energy Lett.* **3**, 125-131 (2018).

(275) Jang, J. W., Du, C., Ye, Y. F., Lin, Y. J., Yao, X. H., Thorne, J., Liu, E., McMahon, G., Zhu, J. F., Javey, A., et al. Enabling unassisted solar water splitting by iron oxide and silicon. *Nat. Commun.* **6**, (2015).

(276) De Vos, A. Detailed Balance Limit of the Efficiency of Tandem Solar-Cells. *J. Phys. D: Appl. Phys.* **13**, 839-846 (1980).

(277) Jia, J. Y., Seitz, L. C., Benck, J. D., Huo, Y. J., Chen, Y. S., Ng, J. W. D., Bilir, T., Harris, J. S., Jaramillo, T. F. Solar water splitting by photovoltaic-electrolysis with a solar-to-hydrogen efficiency over 30%. *Nat. Commun.* **7**, (2016).

A concentrator PV-PEM device with highest STH efficiency of 30% so far.
(278) Esposito, D. V. Membraneless Electrolyzers for Low-Cost Hydrogen Production in a Renewable Energy Future. *Joule* **1**, 651-658 (2017).

(279) Nakamura, A., Ota, Y., Koike, K., Hidaka, Y., Nishioka, K., Sugiyama, M., Fujii, K. A 24.4% solar to hydrogen energy conversion efficiency by combining concentrator photovoltaic modules and electrochemical cells. *Appl. Phys. Express* **8**, 107101 (2015).

(280) Bonke, S. A., Wiechen, M., MacFarlane, D. R., Spiccia, L. Renewable fuels from concentrated solar power: towards practical artificial photosynthesis. *Energy Environ. Sci.* **8**, 2791-2796 (2015).

(281) Winkler, M. T., Cox, C. R., Nocera, D. G., Buonassisi, T. Modeling integrated photovoltaic-electrochemical devices using steady-state equivalent circuits. *Proc. Natl. Acad. Sci. USA* **110**, E1076-E1082 (2013).

(282) Cox, C. R., Lee, J. Z., Nocera, D. G., Buonassisi, T. Ten-percent solar-to-fuel conversion with nonprecious materials. *Proc. Natl. Acad. Sci. USA* **111**, 14057-14061 (2014).

(283) Song, H., Oh, S., Yoon, H., Kim, K. H., Ryu, S., Oh, J. Bifunctional NiFe inverse opal electrocatalysts with heterojunction Si solar cells for 9.54%-efficient unassisted solar water splitting. *Nano Energy* **42**, 1-7 (2017).

(284) Schuttauf, J. W., Modestino, M. A., Chinello, E., Lambelet, D., Delfino, A., Domine, D., Faes, A., Despeisse, M., Bailat, J., Psaltis, D., et al. Solar-to-Hydrogen Production at 14.2% Efficiency with Silicon Photovoltaics and Earth-Abundant Electrocatalysts. *J. Electrochem. Soc.* **163**, F1177-F1181 (2016).

(285) Becker, J. P., Turan, B., Smirnov, V., Welter, K., Urbain, F., Wolff, J., Haas, S., Finger, F. A modular device for large area integrated photoelectrochemical water-splitting as a versatile tool to evaluate photoabsorbers and catalysts. *J. Mater. Chem. A* **5**, 4818-4826 (2017).

(286) Fan, R., Cheng, S., Huang, G., Wang, Y., Zhang, Y., Vanka, S., Botton, G. A., Mi, Z., Shen, M. Unassisted solar water splitting with 9.8% efficiency and over 100 h stability based on Si solar cells and photoelectrodes catalyzed by bifunctional Ni–Mo/Ni. *J. Mater. Chem. A*, (2019).

(287) Zhang, W., Eperon, G. E., Snaith, H. J. Metal halide perovskites for energy applications. *Nat. Energy* **1**, 16048 (2016).

(288) National Renewable Energy Laboratory (NREL) Efficiency chart (2018). https://www.nrel.gov/pv/assets/pdfs/pv-efficiency-chart.20181214.pdf.

(289) Luo, J., Im, J.-H., Mayer, M. T., Schreier, M., Nazeeruddin, M. K., Park, N.-G., Tilley, S. D., Fan, H. J., Grätzel, M. Water photolysis at 12.3% efficiency via perovskite photovoltaics and Earth-abundant catalysts. *Science* **345**, 1593 (2014).

(290) Lee, J. W., Kim, D. H., Kim, H. S., Seo, S. W., Cho, S. M., Park, N. G. Formamidinium and Cesium Hybridization for Photo- and Moisture-Stable Perovskite Solar Cell. *Adv. Energy Mater.* **5**, 1501310 (2015).

(291) Saliba, M., Matsui, T., Seo, J. Y., Domanski, K., Correa-Baena, J. P., Nazeeruddin, M. K., Zakeeruddin, S. M., Tress, W., Abate, A., Hagfeldt, A., et al. Cesium-containing triple cation perovskite solar cells: improved stability, reproducibility and high efficiency. *Energy Environ. Sci.* **9**, 1989-1997 (2016).

(292) Bush, K. A., Palmstrom, A. F., Yu, Z. S. J., Boccard, M., Cheacharoen, R., Mailoa, J. P., McMeekin, D. P., Hoye, R. L. Z., Bailie, C. D., Leijtens, T., et al. 23.6%-efficient monolithic perovskite/silicon tandem solar cells with improved stability. *Nat. Energy* **2**, 17009 (2017).

(293) Andrei, V., Hoye, R. L. Z., Crespo-Quesada, M., Bajada, M., Ahmad, S., De Volder, M., Friend, R., Reisner, E. Scalable Triple Cation Mixed Halide Perovskite-BiVO$_4$ Tandems for Bias-Free Water Splitting. *Adv. Energy Mater.* **8**, (2018).

(294) Peharz, G., Dimroth, F., Wittstadt, U. Solar hydrogen production by water splitting with a conversion efficiency of 18%. *Int. J. Hydrogen Energy* **32**, 3248-3252 (2007).

(295) Fallisch, A., Schellhase, L., Fresko, J., Zedda, M., Ohlmann, J., Steiner, M., Bosch, A., Zielke, L., Thiele, S., Dimroth, F., et al. Hydrogen concentrator demonstrator module with 19.8% solar-to-hydrogen conversion efficiency according to the higher heating value. *Int. J. Hydrogen Energy* **42**, 26804-26815 (2017).

A concentrator PV-PEM device with maximum STH efficiency of 19.8% during two-month field test.

(296) Hashemi, S. M. H., Modestino, M. A., Psaltis, D. A membrane-less electrolyzer for hydrogen production across the pH scale. *Energy Environ. Sci.* **8**, 2003-2009 (2015).

(297) Gillespie, M. I., van der Merwe, F., Kriel, R. J. Performance evaluation of a membraneless divergent electrode-flow-through (DEFT) alkaline electrolyser based on optimisation of electrolytic flow and electrode gap. *J. Power Sources* **293**, 228-235 (2015).

(298) O'Neil, G. D., Christian, C. D., Brown, D. E., Esposito, D. V. Hydrogen Production with a Simple and Scalable Membraneless Electrolyzer. *J. Electrochem. Soc.* **163**, F3012-F3019 (2016).

(299) Chen, L., Dong, X. L., Wang, Y. G., Xia, Y. Y. Separating hydrogen and oxygen evolution in alkaline water electrolysis using nickel hydroxide. *Nat. Commun.* **7**, 11741 (2016).

(300) Landman, A., Dotan, H., Shter, G. E., Wullenkord, M., Houaijia, A., Maljusch, A., Grader, G. S., Rothschild, A. Photoelectrochemical water splitting in separate oxygen and hydrogen cells. *Nat. Mater.* **16**, 646-651 (2017).

(301) Woodhouse, M., Goodrich, A. A Manufacturing Cost Analysis Relevant to Single- and Dual-Junction Photovoltaic Cells Fabricated with III-Vs and III-Vs Grown on Czochralski Silicon. *NREL Technical Report PR-6A20-601267563*, (2013).

(302) Samsudin, M. F. R., Sufian, S., Mohamed, N. M., Bashiri, R., Wolfe, F., Ramli, R. M. Enhancement of hydrogen production over screen-printed $TiO_2/BiVO_4$ thin film in the photoelectrochemical cells. *Mater. Lett.* **211**, 13-16 (2018).

(303) Fekete, M., Hocking, R. K., Chang, S. L. Y., Italiano, C., Patti, A. F., Arena, F., Spiccia, L. Highly active screen-printed electrocatalysts for water oxidation based on β-manganese oxide. *Energy Environ. Sci.* **6**, 2222–2232 (2013).

(304) Guo, Y., Zhang, N., Wang, X., Qian, Q., Zhang, S., Li, Z., Zou, Z. A facile spray pyrolysis method to prepare Ti-doped $ZnFe_2O_4$ for boosting photoelectrochemical water splitting. *J. Mater. Chem. A* **5**, 7571-7577 (2017).

(305) Fekete, M., Riedel, W., Patti, A. F., Spiccia, L. Photoelectrochemical water oxidation by screen printed ZnO nanoparticle films: effect of pH on catalytic activity and stability. *Nanoscale* **6**, 7585-7593 (2014).

(306) Lee, W. J., Shinde, P. S., Go, G. H., Ramasamy, E. Ag grid induced photocurrent enhancement in WO_3 photoanodes and their scale-up performance toward photoelectrochemical H_2 generation. *Int. J. Hydrogen Energy* **36**, 5262-5270 (2011).

(307) Chen, H. J., Bo, R. H., Thanh, T. P., Liu, G. Y., Tricoli, A. One-Step Rapid and Scalable Flame Synthesis of Efficient WO_3 Photoanodes for Water Splitting. *Chempluschem* **83**, 569-576 (2018).

(308) Kho, Y. K., Teoh, W. Y., Iwase, A., Madler, L., Kudo, A., Amarl, R. Flame Preparation of Visible-Light-Responsive $BiVO_4$ Oxygen Evolution Photocatalysts with Subsequent Activation via Aqueous Route. *ACS Appl. Mater. Interfaces* **3**, 1997-2004 (2011).

(309) Liu, G., Karuturi, S. K., Chen, H., Spiccia, L., Tan, H. H., Jagadish, C., Wang, D., Simonov, A. N., Tricoli, A. Tuning the morphology and structure of disordered hematite photoanodes for improved water oxidation: A physical and chemical synergistic approach. *Nano Energy* **53**, 745-752 (2018).

(310) Liu, G., Karuturi, S. K., Simonov, A. N., Fekete, M., Chen, H., Nasiri, N., Le, N. H., Reddy Narangari, P., Lysevych, M., Gengenbach, T. R., et al. Robust Sub-Monolayers of Co_3O_4 Nano-Islands: A Highly Transparent Morphology for Efficient Water Oxidation Catalysis. *Adv. Energy Mater.* **6**, 1600697 (2016).

(311) Mueller, R., Madler, L., Pratsinis, S. E. Nanoparticle synthesis at high production rates by flame spray pyrolysis. *Chem. Eng. Sci.* **58**, 1969-1976 (2003).

(312) Liu, G. Y., Hall, J., Nasiri, N., Gengenbach, T., Spiccia, L., Cheah, M. H., Tricoli, A. Scalable Synthesis of Efficient Water Oxidation Catalysts: Insights into the Activity of Flame-Made Manganese Oxide Nanocrystals. *Chemsuschem* **8**, 4162-4171 (2015).

(313) Sheng, Y., Botero, M. L., Manuputty, M. Y., Kraft, M., Xu, R. Co_3O_4 and $Fe_xCo_{3-x}O_4$ Nanoparticles/Films Synthesized in a Vapor-Fed Flame Aerosol Reactor for Oxygen Evolution. *ACS Appl. Energy Mater.* **1**, 655-665 (2018).

(314) Tran-Phu, T., Chen, H., Bo, R., Di Bernardo, I., Fusco, Z., Simonov, A. N., Tricoli, A. High-Temperature One-Step Synthesis of Efficient Nanostructured Bismuth Vanadate Photoanodes for Water Oxidation. *Energy Technol.*, 1801052 (2019).

(315) Dumortier, M., Tembhurne, S., Haussener, S. Holistic design guidelines for solar hydrogen production by photo-electrochemical routes. *Energy Environ. Sci.* **8**, 3614-3628 (2015).

(316) Holmes-Gentle, I., Agarwal, H., Alhersh, F., Hellgardt, K. Assessing the scalability of low conductivity substrates for photo-electrodes via modelling of resistive losses. *Phys. Chem. Chem. Phys.* **20**, 12422-12429 (2018).

(317) Holmes-Gentle, I., Bedoya-Lora, F., Alhersh, F., Hellgardt, K. Optical Losses at Gas Evolving Photoelectrodes: Implications for Photoelectrochemical Water Splitting. *J. Phys. Chem. C* **123**, 17-28 (2018).

(318) Haussener, S., Hu, S., Xiang, C. X., Weber, A. Z., Lewis, N. S. Simulations of the irradiation and temperature dependence of the efficiency of tandem photoelectrochemical water-splitting systems. *Energy Environ. Sci.* **6**, 3605-3618 (2013).

(319) Xiang, C., Weber, A. Z., Ardo, S., Berger, A., Chen, Y., Coridan, R., Fountaine, K. T., Haussener, S., Hu, S., Liu, R., et al. Modeling, Simulation, and Implementation of Solar-Driven Water-Splitting Devices. *Angew. Chem. Int. Ed.* **55**, 12974-12988 (2016).

(320) Vilanova, A., Lopes, T., Spenke, C., Wullenkord, M., Mendes, A. Optimized photoelectrochemical tandem cell for solar water splitting. *Energy Storage Mater.* **13**, 175-188 (2018).

(321) Kirner, S., Stannowski, B., Jang, J., Abdi, F., Minkyu, S., Mayer, M., Lopes, T., Oswald, F. Public report on large-area PEC/PV components. *PEC DEMO-Project Deliverable Report-D3.3* (2016).

(322) Wullenkord, M., Spenke, C., Vilanova, A., Lopes, T., Mendes, A. Public report on performance of the large-area prototype array. *Project Deliverable Report - D6.4*, (2016).

(323) Artiphyction. http://www.artiphyction.org/.

(324) Tolod, K. R., Hernandez, S., Russo, N. Recent Advances in the BiVO$_4$ Photocatalyst for Sun-Driven Water Oxidation: Top-Performing Photoanodes and Scale-Up Challenges. *Catalysts* **7**, 13 (2017).

(325) Tembhurne, S., Nandjou, F., Haussener, S. A thermally synergistic photo-electrochemical hydrogen generator operating under concentrated solar irradiation. *Nat. Energy* **4**, 399-407 (2019).

A concentrator PV-PEM device with >0.88 A cm^{-2} current densities at >15% STH efficiencies via thermal management.

(326) Touili, S., Alami Merrouni, A., Azouzoute, A., El Hassouani, Y., Amrani, A.-i. A technical and economical assessment of hydrogen production potential from solar energy in Morocco. *Int. J. Hydrogen Energy* **43**, 22777-22796 (2018).

(327) James, B. D., Collela, W. G., Moton, J. M. Hydrogen Pathways Analysis for Polymer Electrolyte Membrane (PEM) Electrolysis *DOE Hydrogen and Fuel Cells Program* [Online], 2014. https://www.hydrogen.energy.gov/pdfs/progress14/ii_a_1_james_2014.pdf.

(328) Shaner, M. R., Atwater, H. A., Lewis, N. S., McFarland, E. W. A comparative technoeconomic analysis of renewable hydrogen production using solar energy. *Energy Environ. Sci.* **9**, 2354-2371 (2016).

(329) Yadav, D., Banerjee, R. Economic assessment of hydrogen production from solar driven high-temperature steam electrolysis process. *J. Cleaner Prod.* **183**, 1131-1155 (2018).

(330) Lin, M., Haussener, S. Techno-economic modeling and optimization of solar-driven high-temperature electrolysis systems. *Sol. Energy* **155**, 1389-1402 (2017).

(331) Koumi Ngoh, S., Ayina Ohandja, L. M., Kemajou, A., Monkam, L. Design and simulation of hybrid solar high-temperature hydrogen production system using both solar photovoltaic and thermal energy. *Sustain. Energy Technol. Assess.* **7**, 279-293 (2014).

(332) Manzhos, S. On the Choice of the Discount Rate and the Role of Financial Variables and Physical Parameters in Estimating the Levelized Cost of Energy. *Int. J. Financial Stud.* **1**, 54-61 (2013).

(333) James, B. D., Baum, G. N., Perez, J., Baum, K. N. Technoeconomic boundary analysis of biological pathways to hydrogen production. *DOE Report*, (2009).

(334) Ljunggren, M., Wallberg, O., Zacchi, G. Techno-economic comparison of a biological hydrogen process and a 2nd generation ethanol process using barley straw as feedstock. *Bioresour. Technol.* **102**, 9524-31 (2011).

(335) Ljunggren, M., Zacchi, G. Techno-economic evaluation of a two-step biological process for hydrogen production. *Biotechnol. Prog.* **26**, 496-504 (2010).

(336) Urbaniec, K., Grabarczyk, R. Hydrogen production from sugar beet molasses – a techno-economic study. *J. Cleaner Prod.* **65**, 324-329 (2014).

(337) Graf, D., Monnerie, N., Roeb, M., Schmitz, M., Sattler, C. Economic comparison of solar hydrogen generation by means of thermochemical cycles and electrolysis. *Int. J. Hydrogen Energy* **33**, 4511-4519 (2008).

(338) Moser, M., Pecchi, M., Fend, T. Techno-Economic Assessment of Solar Hydrogen Production by Means of Thermo-Chemical Cycles. *Energies* **12**, (2019).

(339) Bockris, J. O. M., Veziroglu, T. N. Estimates of the price of hydrogen as a medium for wind and solar sources. *Int. J. Hydrogen Energy* **32**, 1605-1610 (2007).

(340) Boudries, R. Techno-economic Assessment of Solar Hydrogen Production Using CPV-electrolysis Systems. *Energy Procedia* **93**, 96-101 (2016).

Guanyu Liu is a research fellow at the School of Chemical & Biomedical Engineering, Nanyang Technological University (NTU) and Cambridge Centre for Advanced Research and Education in Singapore (CARES). He received his Ph.D. degree at the Australian National University in 2017. His research is focused on the nanostructured catalysts for (photo)electrochemical water splitting and carbon dioxide reduction.
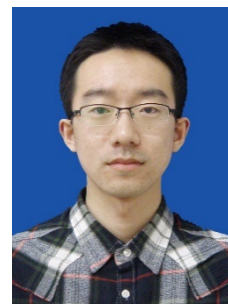
Yuan Sheng is a research fellow at the School of Chemical & Biomedical Engineering, Nanyang Technological University (NTU) and Cambridge Centre for Advanced Research and Education in Singapore (CARES). He obtained his Ph.D. degree at the National University of Singapore in 2016. His current research includes flame synthesis of nanomaterials, water splitting, and CO_2 utilization.

Joel W. Ager III is a Staff Scientist in the Materials Sciences Division of Lawrence Berkeley National Laboratory and an Adjunct Full Professor in the Materials Science and Engineering Department, University of California Berkeley. His research interests include the fundamental electronic and transport properties of semiconducting materials, discovery of new photoelectrochemical and electrochemical catalysts for solar to chemical energy conversion, and the development of new types of transparent conductors.

Prof. Markus Kraft is a Fellow of Churchill College Cambridge and Professor in the Department of Chemical Engineering and Biotechnology. He is the director of CARES Ltd, the Singapore Cambridge CREATE Research Centre. He completed his Doctor rerum naturalium at the University of Kaiserslautern in 1997. His research interests include the computational modelling and optimisation targeted towards developing carbon abatement and emission reduction technologies for the automotive, power and chemical industries. He has also contributed significantly towards the detailed modelling of combustion synthesis of organic/inorganic nanoparticles and worked on engine simulation, spray drying and the granulation of fine powders.

Rong Xu is a Professor at the School of Chemical & Biomedical Engineering, Nanyang Technological University (NTU), Singapore. She received her Ph.D. degree at the National University of Singapore in 2004. Her research group has been actively involved in areas related to energy and environmental applications including solar fuel generation and water treatment, using nanoengineered particulate semiconductor photocatalysts, molecular complexes, and hybrid systems.